KOCH, STEVEN EDWARD

MESOSCALE GRAVITY WAVES AS A POSSIBLE TRIGGER OF SEVERE CONVECTION ALONG A DRYLINE

The University of Oklahoma PH.D. 1979

THE UNIVERSITY OF OKLAHOMA

GRADUATE COLLEGE

MESOSCALE GRAVITY WAVES AS A POSSIBLE TRIGGER OF SEVERE CONVECTION ALONG A DRYLINE

A DISSERTATION

SUBMITTED TO THE GRADUATE FACULTY

in partial fulfillment of the requirements for the

degree of

DOCTOR OF PHILOSOPHY

By

STEVEN E. KOCH

Norman, Oklahoma

1979

MESOSCALE GRAVITY WAVES AS A POSSIBLE TRIGGER

OF SEVERE CONVECTION ALONG A DRYLINE

APPROVED BY

DISSERTATION COMMITTEE

ACKNOWLEDGEMENTS

I wish to express my sincere gratitude to Professor John McCarthy, the chairman of my doctoral committee, for his guidance and unrelenting encouragement throughout this research effort. To my doctoral committee members, Drs. Barnes, Blick, Davies-Jones, Duchon, and Sasaki, special thanks are given for their helpful suggestions and instructive assistance.

I also wish to express my appreciation for the broad support of the National Severe Storms Laboratory, directed by Dr. Edwin Kessler. In particular, assistance in data quality assessment by Mr. Stephan Nelson is acknowledged. The Computer Data Processing group cooperated in making data available for this study, permitting use of the NSSL computer system, and providing essential software for data analysis and display. The final form of this dissertation is due in large part to the patience and ability of Ms. Terry Snodgrass, typist, and Ms. Joan Kimpel, draftsperson.

This work was sponsored by the Atmospheric Sciences Section, National Science Foundation, NSF Grant ATM-78-12401, and was done as part of a graduate study program at the University of Oklahoma.

ABSTRACT

Perturbations in the surface moisture convergence field in the mesoscale environment of the 8 June 1974 Oklahoma dryline are shown to be manifestations of a wavelike mechanism responsible for triggering each of 11 severe storms on that day. Objective analysis of the available mesonetwork data shows the following wave characteristics: horizontal phase speed $C_p = 22$ m/s, median wavelength of 22 km, and mean periodicity of 17 min. Repeated succession of the waves along the dryline sustains the subsynoptic-scale moisture convergence region there, and is also primarily responsible for the eastward progression of the dryline.

Several hypotheses from classical hydrodynamic instability theory are considered as plausible explanations for the mesoscale disturbance. The observations are most in agreement with the test implications and predications of the gravity wave hypothesis. A cross spectral analysis of the data confirms the mesoanalytical estimates of the wave characteristics, and shows the waves to be confined to a region within 20 km of the dryline. Poor spatial coherence is consistent with the fact that gravity waves would be untrapped within the adiabatic boundary layer west of and along the

dryline. A low-level inversion to the east may have caused destructive interference of reflected waves there. Temporally coherent, consistent spectral signals are found in 50% of those mesonet wind records that display linear wind oscillations predicated by gravity wave theory.

Predicted and observed phase velocities C_p are in good agreement. By combining the predicted C_p with the spectral characteristics of the wind fluctuations, the general nature of the observed wind field is reconstructed. The spectral phase relationship of the wind fluctuations differs by only 15° from theoretical predictions. An apparent source of gravity waves is in dynamic instability at an altitude of 2.9-3.2 km AGL; this being the case, then 73% of the maximum wave amplitude aloft could be expected to reach ground level. By employing a predicted wave displacement profile from evanescent gravity wave theory upon a model sounding representative of the observed mesoscale dryline environment, the ability of the assumed gravity waves to periodically trigger the development of the storms is demonstrated.

TABLE OF CONTENTS

LIST OF ILLUSTRATIONS

LIST OF TABLES

LIST OF SYMBOLS

(exclusive of appendices)

A	Aspect ratio
b_1	Spectral bandwidth of Tukey window
$\underset{\sim}{C}$	Advection vector in time-to-space conversion technique
c_p	Specific heat of dry air at constant pressure
$\underset{\sim}{C}_p$	Horizontal phase velocity of wave relative to ground coordinate system
$\underset{\sim}{C}_w$	Intrinsic horizontal phase velocity of wave relative to background flow $\overline{U}$
CI	Spectral confidence interval
$C_{11}(f)$, $C_{22}(f)$	Autospectra of first and second time series
DLW	Subsynoptic dryline "wave"
f	Linear frequency, also Coriolis parameter
f_{NY}	Nyquist frequency ($= \frac{1}{2}\Delta t$)
F_E	Gravity wave energy flux
F_M	Gravity wave momentum flux
g	Acceleration of gravity
h	Height of top of duct layer
H	Estimated source height of gravity wave

i	$\sqrt{-1}$
k	Horizontal wavenumber in x-direction
$\overline{K}_{12}(f)$	Transformed display of smoothed coherence, function of frequency
ℓ	Horizontal wavenumber in y-direction
$L_{12}(f)$	Cospectrum (in-phase), function of frequency
m	$(k^2 + \ell^2)^{\frac{1}{2}}$
M	Maximum lag used in autocovariance calculation
MDLW	Mesoscale dryline "wave"
n	Vertical wavenumber
N	Number of data points in spectral analysis, also Vaisala-Brunt frequency
p	Static pressure
P_o	Transformed pressure at ground level
P_H	Transformed pressure at height H
P_{dyn}	Dynamic pressure due to Bernoulli-effects
$Q_{12}(f)$	Quadrature (out-of-phase) spectrum, function of frequency
$\underset{\sim}{r}_i$	Vectoral distance between station and grid point
r_{uv}	Cross-correlation coefficient characterizing u and v time series
Ra	Rayleigh number
Ri	Richardson number
$R(\lambda)$	Filter response function, function of wavelength
S	Horizontal distance between any two stations along the direction of $\underset{\sim}{C}_p$

t	Time
T, $\overline{T}$	Period (1/f), mean period obtained from histogram plot of spectral results
u,v,w,x,y,z	Wind components in coordinate system of intrinsic wave motion, specified by x
U,V,W,P	Transformed wind components in coordinate system of intrinsic wave motion, and transformed static pressure
u^*, v^*	Estimates of U, V from observations
$\underset{\sim}{\overline{U}}$, $\overline{U}_1$, $\overline{U}_2$	Ambient mean flow vector, in lower layer, and upper layer
$\overline{U}''$, $\overline{U}_{IP}$	Curvature of $\overline{U}$, and $\overline{U}$ value at height of inflection point
$\underset{\sim}{V}$	Horizontal wind velocity
w_i	Objective analysis weight function for station i
z_1, z_2, z_3	Consecutive heights of instrumentation on WKY tower
z_c	Height of critical level
α, α^*	Lag of cross correlation function, and the closest positive 95% significant maximum in cross correlogram to lag $\alpha = 0$
β, β^*	Wave propagation direction, and $270° - \beta$
γ	Numerical convergence parameter in time-to-space conversion technique, also -ni
γ_1	Value of $\gamma = -ni$ in lower atmospheric layer
Δt	Time increment
Δn, Δx, Δz	Average station spacing, objective analysis grid length, and vertical increment

Δf_o	Frequency band centered upon frequency of coherent, consistent spectral signal
$\lvert\Delta\varphi\rvert$	Phase consistency criterion = $\lvert\varphi_{BP} - \varphi_S\rvert$
ζ, ζ_H	Transformed wave vertical displacement, and maximum at height H
η	Wave vertical displacement
θ	Potential temperature, also observed wind direction
θ_e, θ_v, θ_w, θ_o, $\overline{\theta}$	Equivalent potential temperature, virtual potential temperature, wet-bulb potential temperature, mean value of θ in Ri formula, and mean value of θ in a given layer representative of background conditions.
θ_p, θ_p^*	Predicted wave propagation direction, and $270° - \theta_p$
θ_ω, θ_ω^*	Estimate of intrinsic wave propagation direction, and $270° - \theta_\omega$
$\overline{\kappa}_{12}(f)$	Smoothed coherence as function of frequency
κ^*	Spatial weight parameter in time-to-space conversion technique
$\lambda = \lambda_x$, λ_z	Horizontal and vertical wavelengths
ν^*	Temporal weight parameter in time-to-space conversion technique, also spectral degrees of freedom
ρ_o, ρ_s	Height-dependent background air density, and density at the ground reference level
σ, σ_r	Complex frequency, and standard deviation of theoretical population with zero correlation
τ, τ^*	Time delay of propagating disturbance between any two stations, as obtained from the mesoanalyses, and as calculated from phase spectra

$\varphi_{12}(f) = \varphi_S$	Value of phase obtained from phase spectrum
φ_{BP}	Value of phase estimated from bandpass cross correlogram
ω	Intrinsic wave frequency
∇_H	Horizontal del operator

MESOSCALE GRAVITY WAVES AS A POSSIBLE TRIGGER OF SEVERE CONVECTION ALONG A DRYLINE

CHAPTER I

INTRODUCTION

Recent studies have indicated that the formation of convective storm systems is governed by complex interactions between dynamical processes occurring on a wide spectrum of scales. The systems are recognizable as amalgamations of individual storms with distinctive modes of new cell development and orientation. They seem to form in a manner which indicates mesoscale or subsynoptic scale organization, and thus will be referred to as "meso-convective systems".

For the specific purposes of this thesis, scales of motion are defined here by wavelength of disturbance as synoptic (1000-5000 km), subsynoptic (250-1000 km), and mesoscale (10-250 km). Interactions among these scales have been known to occur. In the case of the intersection of various mesoscale boundary-layer convergence lines (squall lines, arc clouds, drylines, fronts, and sea breeze boundaries), frequently the low-level inversion typically found

outside of the mesoscale updraft regions is rapidly eliminated, and new convection triggered. Both the evolution of these systems and the convergence lines have been monitored lately by high-resolution satellite (Purdom, 1976).

Such synoptic scale processes as those discussed by Fawbush, et al. (1951), Miller (1972), Danielsen (1974), and many others are important for establishing dynamical and thermodynamical environments conducive to the formation of meso-convective systems. However, the actual formation has been shown to be better correlated with the intensity, position, and movement of boundary-layer moisture convergence fields (Hudson, 1971; Doswell, 1977; Ulanski and Garstang, 1978). A host of phenomena has been suggested to have a strong relation to these convergence fields, among them the dryline (Sasaki, 1973; Schaefer, 1973, 1975), gravity waves (Matsumoto and Akiyama, 1970; Uccellini, 1975), and the low-level jet stream (Pitchford and London, 1962; Bonner, 1966). However, our understanding of the quantitative relation between the circulations associated with these phenomena and the nature of the convergence field, and theoretical models of these mesoscale mechanisms, still remains very inadequate (Lilly, 1975).

This work attempts to examine the precise role that mesoscale dryline convergence plays in the initiation of discrete convection cells, and the mechanisms likely responsible for the highly fluctuating nature of this convergence

field. Using observations from a single well-documented case, the wavelike nature of these mesoscale convergence patterns is revealed. The dynamics of the disturbance patterns are explained with the help of classical hydrodynamic instability theory, and thus allows a quantitative estimate to be made of their ability to initiate deep convection.

I.a. Properties of the Dryline

The dryline is a low-level discontinuity between warm, moist air to the east originating from the Gulf of Mexico and hot, dry air to the west originating from the desert southwest. Moist air density has a biconstituent nature due to its dependence on both temperature and water vapor content. Hence at the dryline there is no corresponding density discontinuity characteristic of a classical front, as has been shown observationally by McGuire (1962) and theoretically by Schaefer (1975). Consequently, the virtual isentropes near a dryline are nearly vertical throughout the boundary layer (typically below 1-2 km altitude), although they slope above this level to the east to demarcate the low-level inversion over the moist air.

Aircraft traverses through drylines depict the dryline to be an extremely narrow zone of moisture contrast (McGuire, 1962). A close association between the position of the dryline and storm development immediately to its east

was first recognized by Fawbush, et al. (1951), and later quantified by Rhea (1966) who found that 78% of dryline storms develop within 20 km of the wind confluence zone associated with the surface dryline. Recently, objective analysis of surface data has revealed subsynoptic areas of moisture convergence near the dryline (Hudson, 1971; Sasaki, 1973; Doswell, 1977).

Various hypotheses have been formulated to explain such observations as Rhea's. In some cases, passage of a mid-tropospheric "short wave" disturbance over the dryline apparently may initiate convection as the field of upward motion progressing eastwards first encounters the potential instability at the dryline. Rhea found such a disturbance in 71% of the convectively active cases studied.

Another mechanism that can operate in the absence of synoptic-scale vertical motion was postulated by Schaefer (1975). According to this theory, the initial density homogeneity dictated by the distributions of heat (potential temperature) and moisture (mixing ratio) theoretically cannot persist; rather, a density minimum (or virtual potential temperature maximum) should develop as the consequence of independent diffusion of heat and moisture at a rate proportional to the product of the constituent gradients. Thereafter, the reduced density at the dryline could initiate a secondary circulation of several cm/sec

magnitude at the dryline. This mechanism is termed non-linear biconstituent diffusion.

A third mechanism which might explain the formation of dryline moisture convergence is the convergence of momentum flux in the boundary layer. With the aid of daytime heating of the high terrain west of the dryline, a dry adiabatic boundary layer can rapidly grow to depths of several kilometers. Zonal momentum in the mid-tropospheric jet stream can then be entrained into the top of this layer and rapidly transported downwards to the surface by means of turbulent mixing. As this zonal momentum encounters the meridional momentum field to the east, dryline convergence would be enhanced. Observations of strongly ageostrophic flow and negative Richardson numbers west of the dryline by Sasaki (1973) give support to the idea of such a downward turbulent transport of momentum. McGinley (1973) vertically integrated the momentum equation from synoptic data and found that the eddy residuals (implicitly assumed to represent vertical turbulent transports) were maximized immediately southwest (upwind) of eastward bulges in the dryline, suggesting sinks of momentum. These observations are consistent with the dryline "wave" (DLW) model of Tegtmeier (1974), displayed in Fig. 1. In this model, surface winds back in response to the isallobaric pressure gradient force induced by falling pressures northeast of

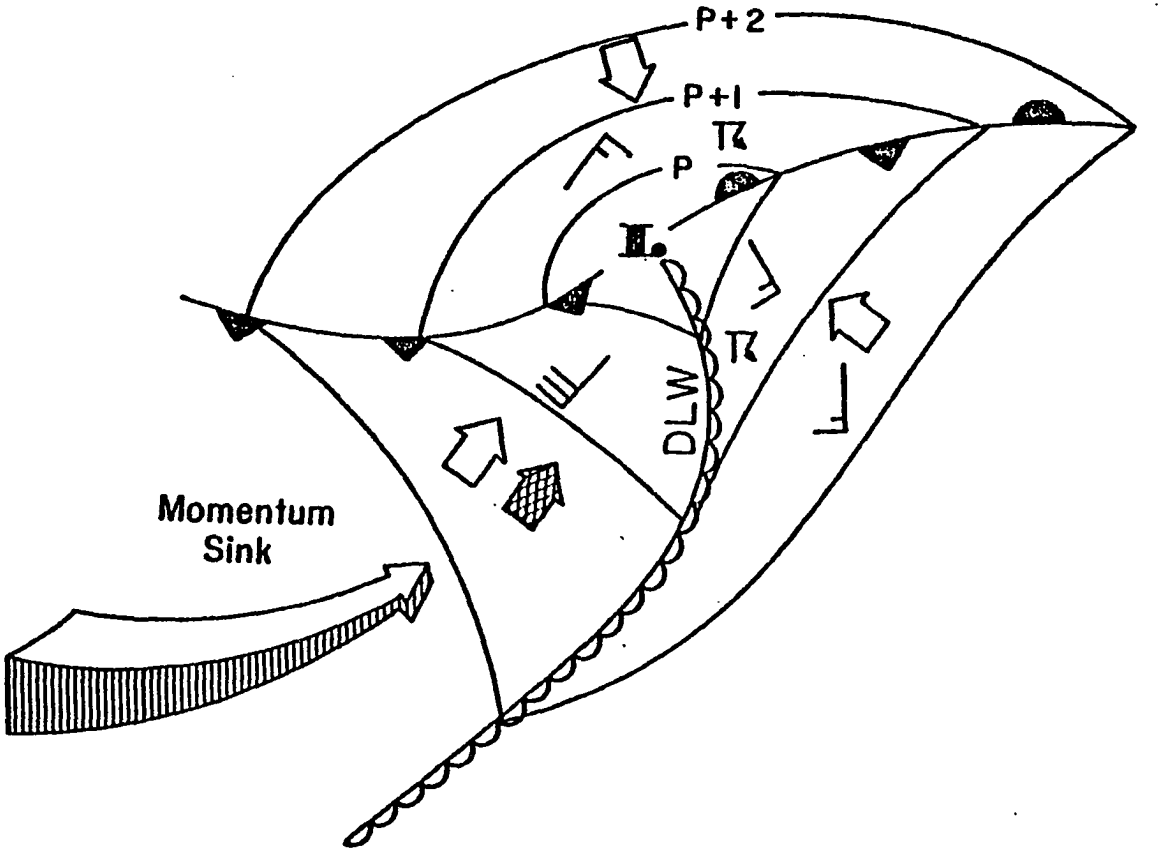

Fig. 1. Schematic model of the relationship between low pressure system, dryline "wave" (DLW), momentum flux, and deep convective development, after McGinley (1973) and Tegtmeier (1974).

both the low pressure center and the DLW.

All of these mechanisms are intended to explain subsynoptic areas of moisture convergence and resulting development of meso-convective systems. It is unknown whether any of these hypotheses are directly relevant to the formation of discrete convective cells. The mid-tropospheric disturbance concept undoubtedly applies to a much larger scale than the one of interest. Nonlinear biconstituent diffusion has not been sufficiently tested against actual observations, and was apparently not the primary cause of convection in at least one case (Ogura and Chen, 1977). The momentum flux convergence mechanism would operate quite efficiently during the passage of a jet streak over the deep boundary layer, and thus in such cases it may operate concurrently with the "short wave" disturbance mechanism.

What kind of dynamic adjustment might occur on the mesoscale as a consequence of the rapid transfer of westerly momentum to the mixed layer west of the dryline? One possible response might be a horizontal shearing instability within the wind confluence zone near the dryline. Vertical vortex tubes would result, and as these are advected with the mean winds, it is conceivable that convection might be generated if the atmosphere is statically unstable (Kuo, 1949; Barcilon and Drazin, 1972).

Another possible mesoscale response might be gravity

waves resulting from a state of geostrophic imbalance (Blumen, 1972); the strongly ageostrophic flow observed by Sasaki (1973) and indicated behind the dryline in Fig. 1 are evidence in support of such a state. On the other hand, Danielsen (1974) has questioned whether dynamic instability might sometimes result from the strong vertical wind shear existing in the statically stable atmosphere above the mixed layer west of the dryline. Although this instability could act as a source for gravity waves (Miles, 1961; Gossard and Hooke, 1975), such an hypothesis is questionable since downward propagation of wave energy through the mixed layer would be greatly attenuated before the waves reached the ground.

To date there exists very few observations of mesoscale dryline structure and the storm-triggering mechanisms, and virtually no understanding of the governing dynamics. In only case (NSSP, 1963) have mesoscale dryline waves been detected; specifically, longitudinal wavelike patterns in the moisture and temperature fields were observed just to the east of a dryline.

I.b. Objectives of Case Study

Previous research on the mechanisms responsible for creating and sustaining boundary-layer moisture convergence near the dryline has focused on the subsynoptic scale. There remains a large gap in our knowledge of mesoscale

precursor conditions to severe convective development, and a great need to understand the dynamics of the actual storm-triggering mechanisms through a definitive comparison with classical hydrodynamic instability theory. This thesis attempts to relieve this condition by exploring answers to the following questions using observations from one case study: (1) Can a mesoscale "trigger mechanism" be isolated and its characteristics investigated? (2) What is the relationship of the mechanism to the evolving mesoscale structure? (3) Is it possible to quantitatively demonstrate the ability of the mechanism to initiate deep convection?

The particular case of 8 June 1974 is studied because various sensing systems observed both the general mesoscale environment and the storm-triggering disturbances prior to radar detection of storm precipitation. In Chapter 2 we discuss the objective technique employed in the analysis of the subsynoptic and mesonetwork data. A preliminary report of the mesoscale structure (Koch and McCarthy, 1977) is currently being prepared for publication, and results of this study relevant to the disturbance analysis appear in Chapter 3. Also appearing in this chapter are the results of an objective analysis of surface mesonetwork data, which reveal the presence of wavelike disturbances apparently responsible for storm initiation. Classical theory is reviewed in the next chapter to assist in

the formulation of a cross spectral and bandpass filter analysis of pertinent parameters useful in testing the applicability of the various hypotheses. This is not intended to be an exhaustive treatment of hydrodynamic stability theory, but rather an aid in understanding which avenue of research would be most fruitful in the study of the disturbance dynamics. The statistical methodology and results appear in Chapters V and VI, respectively. Of the various hypotheses which appear plausible, the gravity wave idea offers the most test implications, hence the entire Chapter VII is devoted to a rigorous testing of this hypothesis. Results from the objective mesoanalysis and cross spectral study are synthesized in Chapter VIII with observations from subsynoptic rawinsondes and an instrumented tower. From this synthesis and the results of the previous section, a model of the structure of the local dryline environment is constructed, which allows for an estimate of the ability of the disturbance to release the potential instability of the atmosphere at the dryline. A summary of the results is presented in Chapter IX.

CHAPTER II

OBJECTIVE SURFACE ANALYSIS TECHNIQUE

For this case study, data from 26 National Severe Storms Laboratory (NSSL) surface mesonetwork stations were processed. Analog chart data collected at each station were digitized at one minute intervals onto magnetic tape. Several data gaps of a few minutes duration were filled by applying interpolating Lagrange cubic polynomials; other random digitization errors were detected by calculating first-order time derivatives, then subsequently removed by reference to the chart data.

To represent accurately the dryline's moisture gradient, a bias correction had to be applied to most hygrometer data. Comparative measurements made by field technicians during the Spring of 1974 indicated a need to apply small corrections to recorded relative humidity values to account for instrumental calibration and hysteresis problems. A plot of 510 calibration data from 26 mesonetwork stations showed a clear dependence of bias error on the value of RH, namely positive errors at low RH (at most 6% too high for RH $< 43\%$), and negative errors at moderately high RH (at most

2% too low). No corrections were actually applied for RH> 43% because the errors did not exceed the hygrothermograph resolution (see Appendix B).

Remaining systematic errors could be attributed to spatial bias caused both by inhomogeneity of the surrounding countryside and instrument inaccuracies. A spatial singularity technique was utilized to reduce these errors in relative humidity, temperature, pressure, and wind speed/direction. This technique involves (1) construction of a highly smoothed map analysis of data averaged over the analysis period 1100-1900, (2) consideration of the general mesometeorological conditions over that period, e.g. dryline isochronology, and (3) removal of bias error assumed to exist for any single station whose time-averaged value clearly differed from that at neighboring stations. In effect, the greatest magnitude of bias corrections applied were: temperature, 1.2°F; relative humidity, 6%; pressure, 1.020 in Hg (digitization error); wind speed, 3 knots; wind direction, 15°.

A low-pass filter was applied to all data to (a) alleviate instrumental response and resolution problems (discussed in section V.a.), and to (b) reduce concern over possible aliasing at frequencies $f > \frac{1}{2} f_{NY}$ (where f_{NY} is the Nyquist frequency) introduced as a consequence of the digitization process. The selected pre-filter was designed by

Stephens (1966); it strongly suppresses response to any signal whose period is shorter than 5.0 min (see Fig. 2).

Subsynoptic and mesoscale surface data are objectively analyzed using the time-to-space conversion technique of Barnes (1973). This time-to-space conversion technique is similar to the earlier non-automated technique of Fujita (1963) in one important respect, namely that the properties of the system of interest are assumed to be advected horizontally along the translational velocity $\underset{\sim}{C}$ of the system. As with other objective analysis methods, this scheme weights observations to obtain interpolated values at grid points of a square mesh, yet is unique in that the weights are functions of the age of the observations relative to the map time, in addition to their distance from the grid points.

The weight at a grid point given to a station i is

$$w_i = \exp\ (-\underset{\sim}{r}_i^2/\kappa^* \gamma - t^2/\nu^*), \qquad (1)$$

where $\underset{\sim}{r}_i = \underset{\sim}{C}t$ is the vectoral distance between station and grid point, t is the temporal displacement, and κ^* and ν^* are, respectively, spatial and temporal weight parameters whose values are chosen on the basis of the scale size of the phenomenon of interest, the data density, and the degree to which the phenomenon may be assumed to be in steady-state. A numerical convergence parameter γ is used to reduce

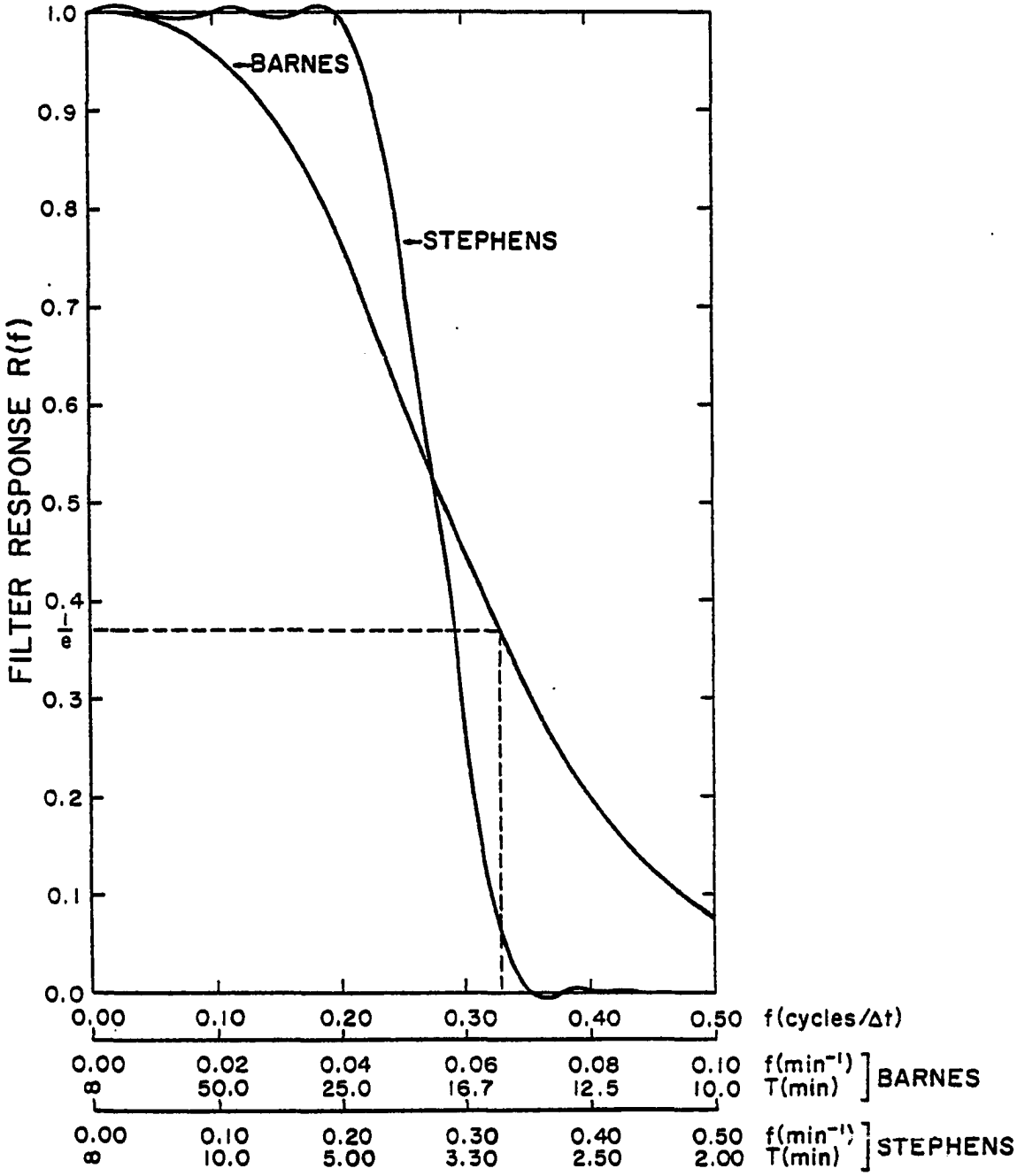

Fig. 2. Low-pass filter response curves: 25-weight data prefilter (Stephens), and inherent filter to mesoscale objective analysis (Barnes). Sampling interval $\Delta t = 1$ min for Stephens filter, $\Delta t = 5$ min for Barnes filter. Note 1/e response of Barnes filter occurs at 15 min period (16.7 km wavelength).

computer time necessary to fit interpolated values to observations; only one iteration including γ upon an initial interpolation without γ is sufficient to achieve the desired fit.

For the mesoanalyses in this thesis, the following parameter values are used: $\kappa^* = 81\ km^2$, $\nu^* = 225\ min^2$, and $\gamma = 0.4$. The analyses are made at 10-min intervals utilizing the filtered data from 26 stations spaced $\Delta n = 13.5$ km apart on the average, and interpolated to a square mesh of grid spacing $\Delta x = 4.8$ km. For the chosen value of $\underset{\sim}{C} = 218°$, 66.6 km/hr applied in all analyses between 1100 and 1730, and the parameter values above, the resulting response is 0.76 for $\lambda = 2\Delta n = 27$ km and 0.04 for $\lambda = 2\Delta x = 9.6$ km. Notice that this technique implicitly contains a low-pass filter, resulting in at least 92% reduction in the amplitude of all waves with periods shorter than 10 minutes (see Fig. 2).

If the mesoanalysis display of small wavelike disturbances is to have any real meaning, it will be necessary that the objective analysis technique be capable of resolving the $2\Delta n$ wave. Classical sampling theory (Petersen and Middleton, 1963) dictates that this wave cannot be resolved through a conventional synoptic analysis, however it is shown in Appendix A that the Barnes technique has the unique ability to resolve the $2\Delta n$ wave. For additional information on the methods by which the values for κ^* and ν^*

were chosen and the results of sensitivity tests on the variability of the $\underset{\sim}{C}$ value, the reader is directed to this appendix.

CHAPTER III

METEOROLOGICAL CONDITIONS IN 8 JUNE 1974 CASE STUDY

III.a. Synoptic and Subsynoptic Conditions

The synoptic environment on 8 June 1974 showed strong potential for a major tornado outbreak in the Southern Plains. A major short wave trough at 500 mb was approaching eastern New Mexico at 00Z 9 June with an 80 kt jet core over the Texas Panhandle and pronounced diffluence in the exit region of the jet over all of Oklahoma. At 700 mb, pronounced drying and cooling had occurred by this time throughout Kansas and northern Oklahoma. An 850 mb dryline appeared in central Oklahoma at the juncture of (a) an extremely moist air mass in eastern Oklahoma (19°C dew point at OKC) being advected northward by a 50 kt southerly jet, and (b) an extremely dry air mass to the west being advected northeastwards by a 40 kt jet. Vertical juxtaposition of all of these phenomena results in considerable conditional and potential instability, and strong vertical wind shear (5×10^{-3} sec^{-1} in the 1-6 km layer of the 12Z 8 June 1974 Norman sounding) in central and northeastern Oklahoma.

Rapid surface cyclogenesis occurred throughout the day in southwestern Kansas. Objective analysis of subsynoptic surface data (see Fig. 3a) by Tidwell (1975) reveals the presence of a marked dryline bulge and an associated maximum of moisture convergence in central Oklahoma. Deep convection repeatedly formed generally within the subsynoptic moisture convergence area in central Oklahoma, and more specifically within the NSSL mesonetwork outlined there. The two regions of strongest pressure fall, in Kansas east of the low pressure center and in northern Oklahoma east-northeast of the DLW, correlate well with the moisture convergence field, in accordance with the Tegtmeier (1974) model.

The vertical structure of the subsynoptic environment of the dryline can be seen in the west-east isentropic cross section in Fig. 3b. A remarkable adiabatic boundary layer is evident west of the dryline, whose origin is in the strong surface heating there, as discussed earlier. Above this layer, strong vertical wind shear exists in association with the 500 mb southwesterly jet stream and strong static stability above 4.4 km AGL. Within the adiabatic layer is a weak manifestation of the dry, southwesterly jet whose core is at 750 mb in the region southwest of CDS (see Fig. 3a). East of the dryline and within the low-level inversion is the familiar moist, southerly jet. Between these converging low-level jet streams is the dryline,

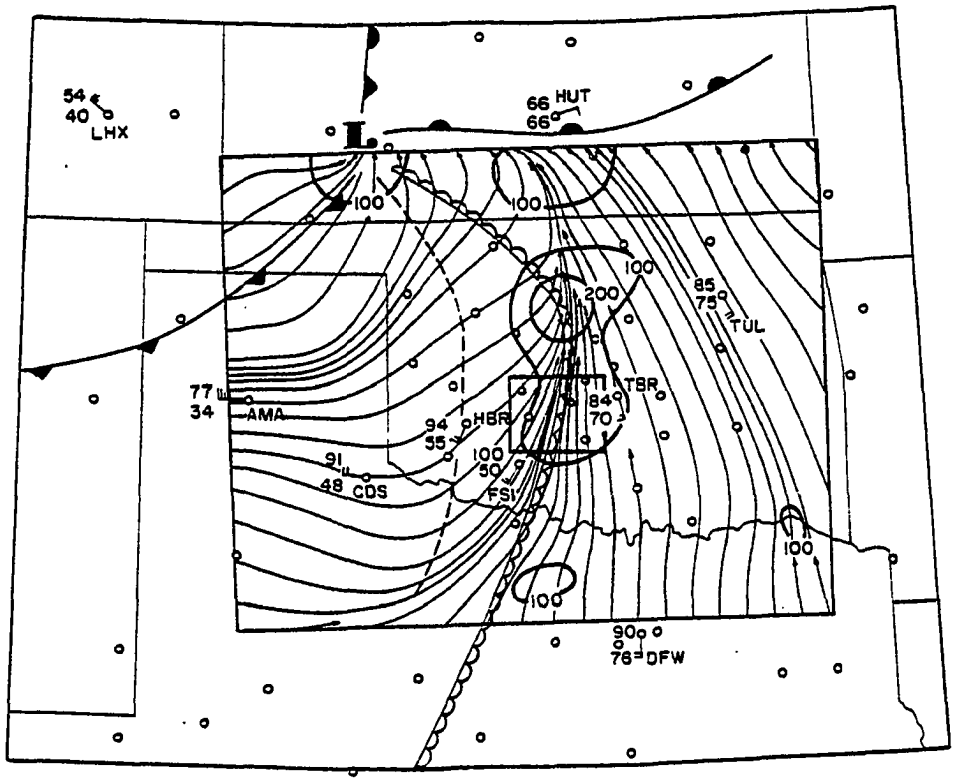

Fig. 3a. Subsynoptic objective analysis at 1400 CST of streamlines and moisture convergence (intervals of 100×10^{-5} g kg^{-1} s^{-1}) at earth's surface, and subjective analysis of frontal systems including the "weak frontal system" (dashed line), and the dryline (scalloped line). Notice the location of small rectangular NSSL mesonetwork and locations of all stations used in subsynoptic objective analysis.

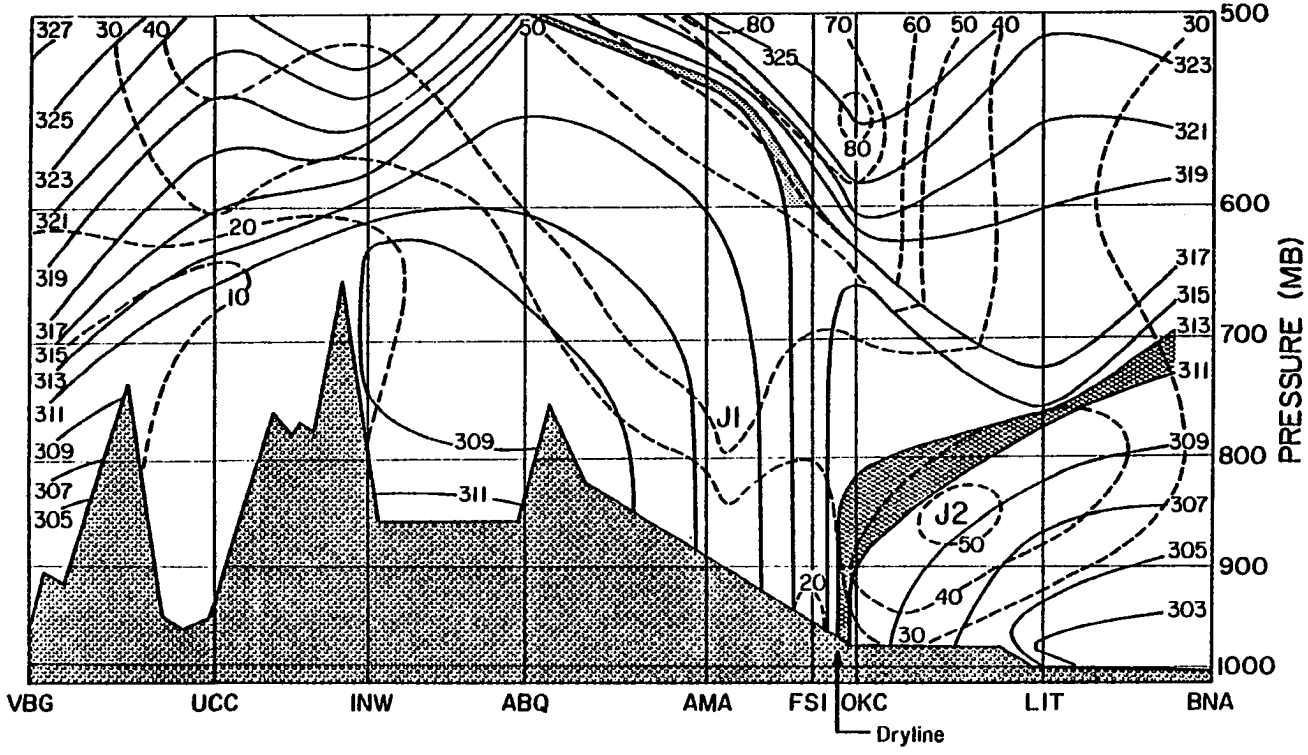

Fig. 3b. West-east cross sectional analysis of virtual potential temperature (isentropes are solid lines, in K) and total windspeed (isotachs are dashed lines, in kt) at 00Z 9 June 1974. Observations at: Vandenburg AFB CA, Winnemucca NV, Winslow AZ, Albuquerque NM, Amarillo TX, Oklahoma City OK, Little Rock AR, and Nashville TN. Note the dry, southwesterly jet J1, the moist, southerly jet J2, the base of the mid-tropospheric inversion (shaded), and the top of the low-level inversion (cross-hatched).

which necessarily appears as a vertical interface in the region of highest virtual potential temperature. This configuration is in accordance with Schaefer (1975).

Satellite and surface observations indicated the development of a duststorm, and strong gusty winds, over the Texas Panhandle and southwestern Oklahoma. Correlation between the appearance of dust streaks and the formation of meso-convective systems has been observed in other dryline situations by Anthony (1978). This relationship can be explained in terms of the DLW-momentum flux model (Fig.1) if the momentum existing above the deep boundary layer west of the dryline were transported downwards through this layer to the ground, where a "sandblasting" effect could result in upward flux of arid soil particles. Such a mechanism is not unrealistic since this layer is obviously well-mixed, in terms of both potential temperature (a conservative parameter) and momentum (the surface wind direction of 220° is exactly that of the mass-weighted mean wind in this layer above FSI). Thus the duststorm may be evidence for such a process. Now this process naturally would result in an increase in the southwesterly momentum at the surface just downwind of the duststorm. Since the DLW is located downwind of the duststorm, then it is conceivable that both the DLW and associated moisture convergence may be the direct consequence of the downward transport of momentum through the mixed layer west of the dryline.

Although this hypothesis is appealing, it was not the purpose of this research to verify it with the existing data. This idea is only presented as one tenable explanation for the observed sequence of events on the subsynoptic scale, and is intended to serve as a background for the mesoscale discussion.

Despite the hypothesized momentum entrainment, a sharp vertical gradient of momentum was maintained just beneath the mid-tropospheric inversion during the 1246-1640 CST[1] interval at Ft. Sill (Fig. 4a). In fact, the height of the inversion base lifted from 3.0 km to 4.1 km AGL and sharpened throughout this period, just as would be anticipated if the eddy vertical heat flux $\overline{w'\theta'}$ were negative as implied by the mixing-momentum entrainment process just discussed. This inversion will be of considerable interest later in the discussion of gravity waves. Notice that the sounding made at Norman (Fig. 4b), which was at the time only 25 km east of the dryline, displays a lower inversion base but similar strong vertical wind shear there.

Unfortunately, the Norman rawinsonde probably passed through several small convective clouds on its way upwards, as evidenced by the superadiabatic layer around 790 mb and the rapid drying above. Moreover, the data above 500 mb should not be considered at all representative of ambient

---

[1]Hereafter, all unindexed times are Central Standard Time (CST).

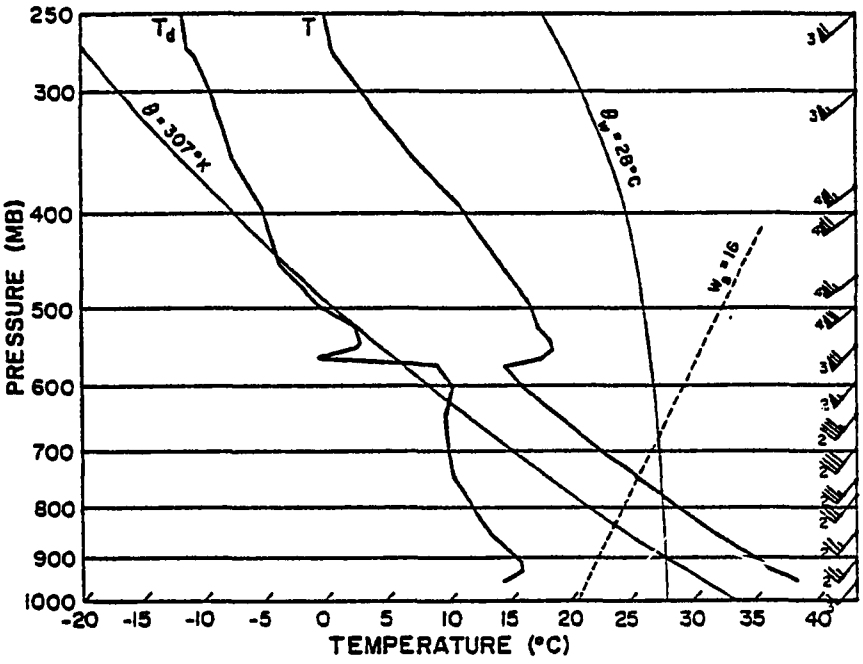

Fig. 4a. Ft. Sill, OK sounding (FSI in Figs. 3a and 22) at 1640 CST on 8 June 1974, plotted in Skew T-lnp coordinates (winds in knots).

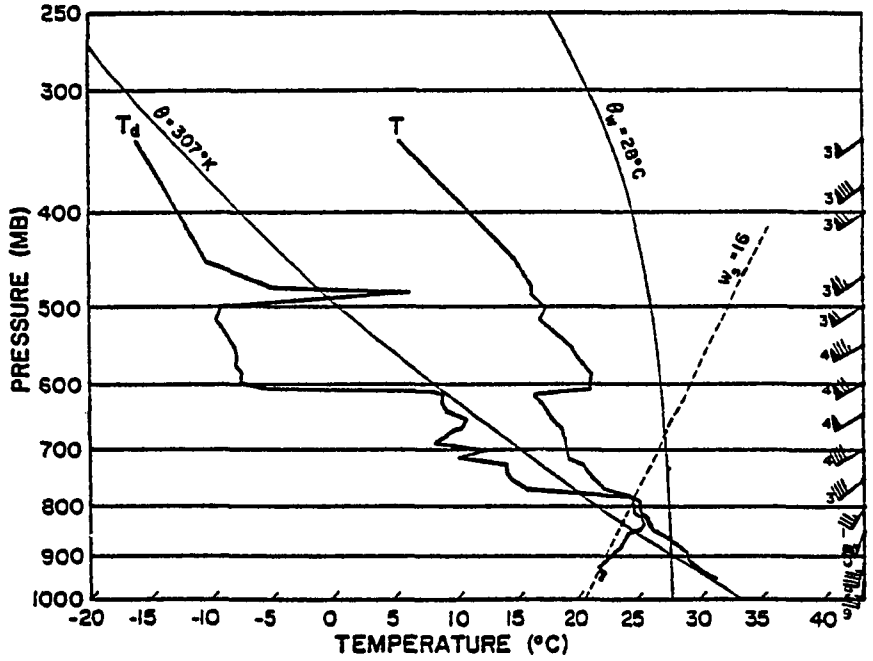

Fig. 4b. Norman, OK sounding (OUN in Fig. 22) at 1710 CST on 8 June 1974, same format as in Fig. 4a.

conditions because of the balloon's proximity to strong convection. Despite these drawbacks, this sounding is believed the most useful of the Norman serial releases on this day, because of its spatial proximity to the dryline and its temporal proximity to both the Ft. Sill sounding and observed mesoscale disturbances.

The atmosphere both west of (FSI) and east of (OUN) the dryline is potentially unstable. Although both soundings indicate surface superadiabatic layers, even those air parcels which ascend from the ground at Norman cannot reach their level of free convection (780 mb) without being mechanically forced to rise through the slightly stable layer beneath. Thus, a triggering mechanism is necessary, either in the form of layer lifting or additional low-level destabilization, to permit the spontaneous development of deep convection.

III.b. Radar Observation of Storm Echoes

Storm echoes within an 80 km radius of the WSR-57 surveillance radar at NSSL are displayed in Fig. 5 at 30 minute intervals, beginning with the first organized system of echoes as it developed into a line at 1230 just ahead of the dryline. The radar displays inside the 40 km range are the result of combining computer-plotted digital reflectivity values (Wilk and Brown, 1975) with microfilmed video PPI configurations; elsewhere the digital data alone is

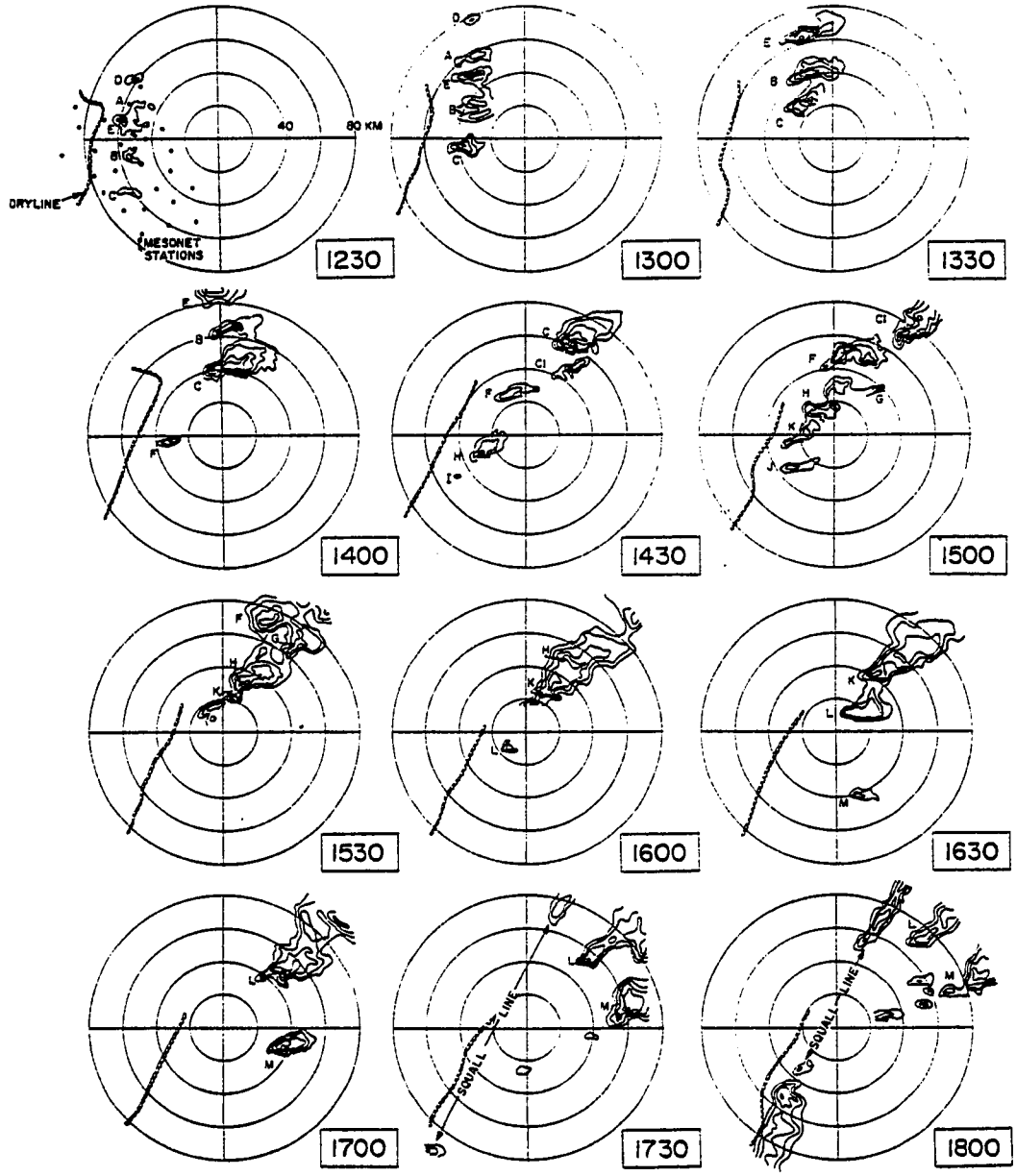

Fig. 5. Plan Position Indicator (PPI) display of radar reflectivity within 80 km radius of NSSL. Isoecho contours at intervals of 27, 36, 41, 46, and 51 dbZ. All displays are at either 0, 1, or 2 deg elevation angle at intervals of 30 min. Storms are labelled alphabetically, objectively analyzed dryline location given by scalloped line.

utilized. Altogether three meso-convective systems can be discerned from these displays, as summarized in Table 1.

All but one of the 22 documented tornadoes which developed over central and northeastern Oklahoma were produced by storms C, M, and the storms of system II (there were 8 other tornadoes in Kansas and Missouri). One reason for the preponderance of system II is that the geometrical configuration and spacing between the storm cells of that system are most favorable for severe storm formation because there is less competition for the available low-level moisture being transported northward.

It is not the purpose of this thesis to examine those dynamical processes which may have contributed to the development of these three systems, although this has been done and will be reported elsewhere. Instead, the problem that is being addressed here is: What mechanisms could have caused the formation of each of the storm cells over the mesonetwork? The storms of meso-convective system II will hereafter be the focus of attention, because their repeated development over a very restricted mesoscale area is a most fascinating and unusual event that deserves explanation.

The position of the dryline in Fig. 5 is obtained from the objective mesoanalyses explained below. Except for storm M, which was an isolated storm first detected by

satellite in extreme southern Oklahoma, every new storm formed within 20 km of the dryline. Thus clearly a very close relationship exists between the surface position of the dryline and the development of meso-convective systems despite earlier occurrence of storms in the same area; this is in excellent agreement with Rhea (1966).

Table 1. Meso-convective Storm Systems During Afternoon of 8 June 1974

System	Times over Mesonet (CST)	Storm Members	Characteristics
I	1210-1320	A,B,C,D,E	Broken line of storms. N-S orientation. Simultaneous mode of development. Developed 20 km east of dryline.
II	1350-1600	F,H,I,J,K,L	Broken line of storms. NE-SW orientation. Consecutive mode of rear flank development. Developed 15-20 km east of dryline.
III	1730-1900	Not indexed	Solid squall line of storms. NNE-SSW orientation. Quasi-simultaneous mode of development. Developed along dryline.

III.c. Evolution of the Mesoscale Dryline Environment

The mesoanalyses depicted the dryline as a very narrow zone of moisture gradient separating the air mass of great moist static instability ($\theta_e > 365$ K) from a more stable air mass (325 K $< \theta_e <$ 340 K) to the west, with virtually all of this differential occurring within a 10 km zone. The fact that mesoscale observations are sufficient to resolve such a fine scale that had previously only been detected by aircraft (McGuire, 1962) is evidence of the validity of the time-to-space conversion technique.

In this study the dryline is delineated by the 355 K isopleth of θ_e, typically located at the easternmost edge of the sharp θ_e gradient. No significant difference results when another moisture variable is used instead; however, θ_e is preferred because it is a conservative parameter which describes the thermodynamic nature of an air mass. Isochrones of the surface dryline position are depicted in Fig. 6. Notice that the mesoscale dryline decelerated after 1400 and came to a virtual halt during the period 1600-1800. One possible cause for this is that the efficiency with which dry air can mix with moist air was significantly reduced as the dry air encountered an increasingly deep moist layer in its eastward progression across the gentle downslope in western Oklahoma. This topographic mechanism was advanced by Schaefer (1973) as a likely reason for why Oklahoma drylines rarely progress beyond the center of the state

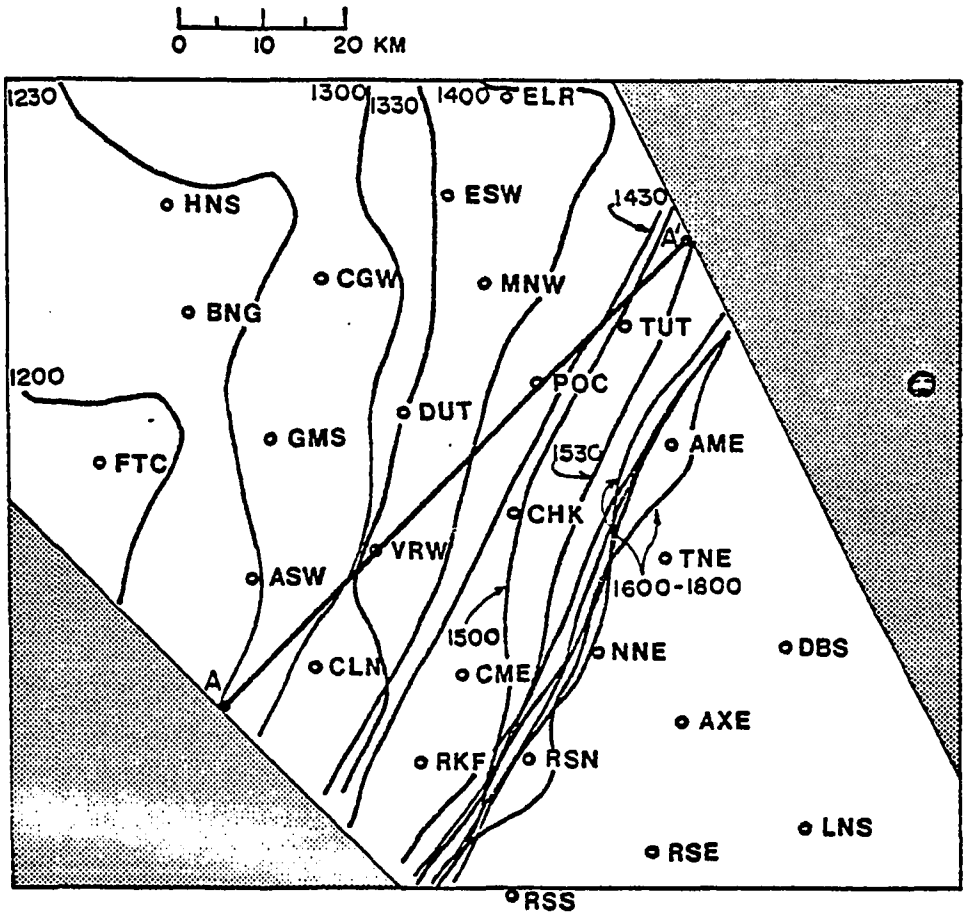

Fig. 6. Isochrones of surface dryline location determined from objective analysis of θ_e field. Note line A-A' depicting the plane of space-time cross section analysis shown in Fig. 11, and the scale at top of figure for future mesonet figures.

under synoptically quiescent conditions.

The conditions on 8 June 1974 were definitely not quiescent, and so the topographic mechanism is of minor importance here. In fact, the mesoanalyses reveal the presence of a different mechanism that most contributes to the dryline's general eastward progression. This mechanism is manifested as wavelike perturbations that propagate along the dryline.[2] The evolution of the θ_e field during the passage of one such mesoscale dryline "wave" (MDLW) η is shown in Fig. 7. This particular feature possessed good continuity of wave form and phase velocity until dissipation about 1520, but only after causing the dryline to advance past stations RKF, CME and CHK (a new MDLW labelled $\varkappa$ appears at 1520).

A comparison is made at 1520 of the positioning of the dryline (355 K isopleth) and existing MDLW by the mesoscale objective analysis and the Doppler radar reflectivity display (a refractive index gradient naturally occurs at the dryline's moisture gradient). Special attention should be paid to the western edge of the radar dryline, and allowance should be made for the small time difference between displays, when searching for the radar MDLW η and $\varkappa$ (notice that upon extrapolating MDLW η to 1520 with the same phase

[2]Such a perturbation will be referred to as mesoscale dryline "wave" (MDLW), although the wave characteristics of repetition and periodic behaviour are evident only in the associated perturbations in the wind fields discussed in Section III.d.

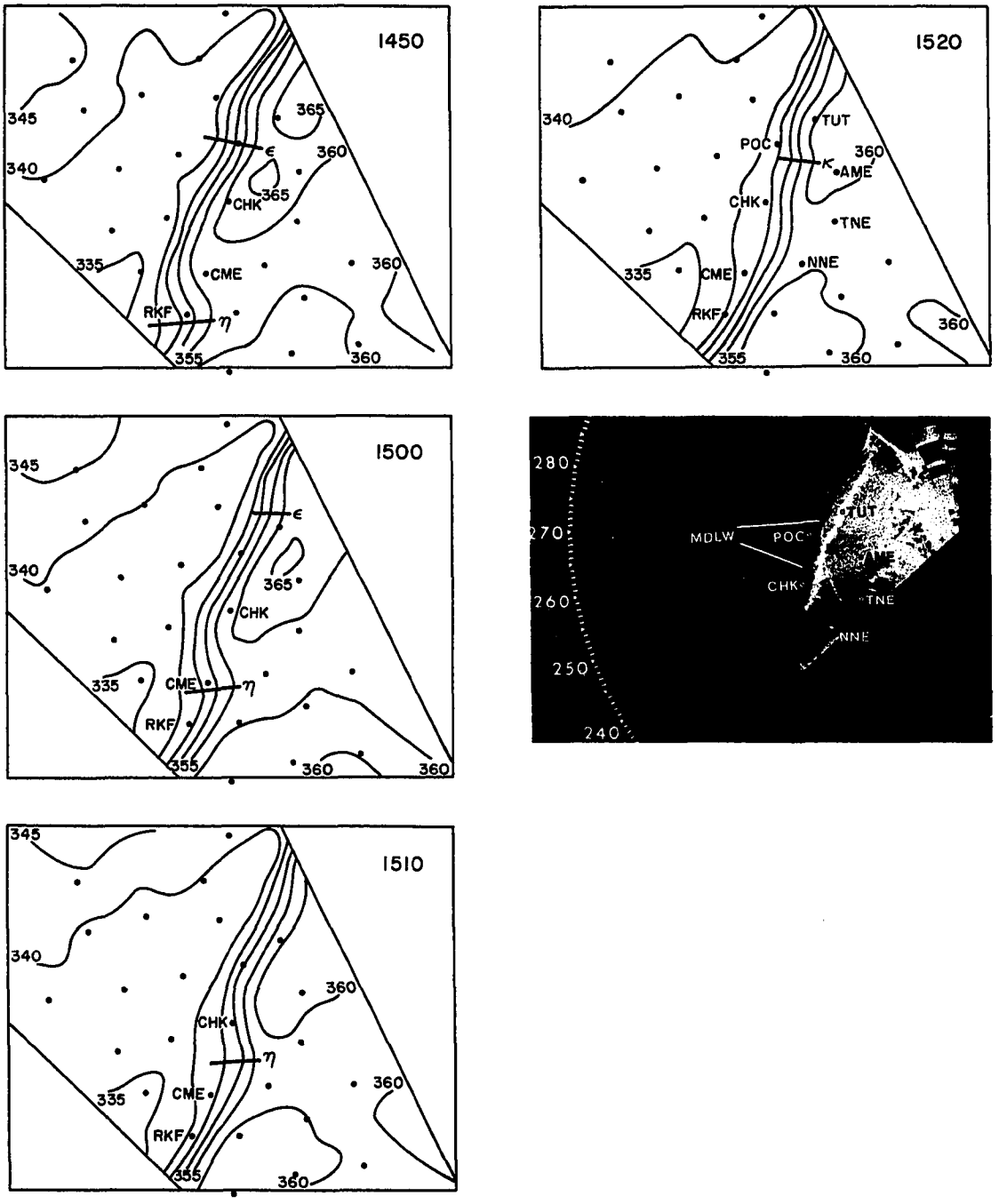

Fig. 7. Mesoscale Dryline Waves (MDLW) seen in objectively analyzed θ_e field and Doppler radar reflectivity display (152124 CST).

velocity as that existing before 1520, excellent agreement between displays would result). An independent check on the validity of the MDLW confirmed that there is good agreement between the times at which θ_e depressions are found in the original time series data and the appearance of an MDLW at the station in question.

This observation adds a new dimension to our understanding of dryline behaviour: travelling mesoscale disturbances may be more important than topographically-related variations in mixing efficiency in pushing some drylines eastward. Several of the MDLW were very dramatic, as can be seen in Fig. 6 during the 1200-1300 interval. During this time the subsynoptic DLW passed through the western portion of the mesonet and was resolvable on the mesoscale as two pronounced MDLW. The hypothesized cause-and-effect relationship between MDLW activity and dryline advancement is further substantiated by the observation that no MDLW activity is detectable after 1600, when the dryline had come to a stop. Incidentally, the MDLW were never simply advected north-northeastwards by the surface flow, because maximum wind speeds were only ~50% of MDLW speed, as estimated from the movement of the MDLW axes (Fig. 7).

It is of interest to examine the evolution of the mesoscale density field, inversely related to virtual

potential temperature[3] θ_v. Although the results of the objective analysis are shown at 90 minute intervals, the general density field can still be examined without significant loss in continuity (Fig. 8). Obviously a θ_v maximum occurs west of the dryline throughout the 1200-1500 period. This particular feature is centered on the westernmost station FTC (see Fig. 6), and suggests station bias there was inadequately accounted for. Because this station was located near the western border, it consistently displayed the lowest RH values, and thus it is quite possible that the bias removal technique was ineffective there.

This bias problem is of no large concern, since the feature of interest is the development of a θ_v maximum within the dryline zone ($\pm$ 10 km of the dryline) by 1300. This maximum is the consequence of oppositely directed gradients of potential temperature and mixing ratio. Although this behaviour is consistent with the predictions of Schaefer's (1975) theory of nonlinear biconstituent diffusion, it by no means confirms that theory. Still these observations are important for two reasons: (1) the θ_v field after 1300 implies the presence of a narrow zone of reduced density and enhanced parcel buoyancy along the dryline, and (2) this

---

[3]The virtual temperature field is less informative than the θ_v field because no correction has been applied for pressure differences related to topography. It can be easily shown that local changes in density are singularly related to local changes in inverse θ_v.

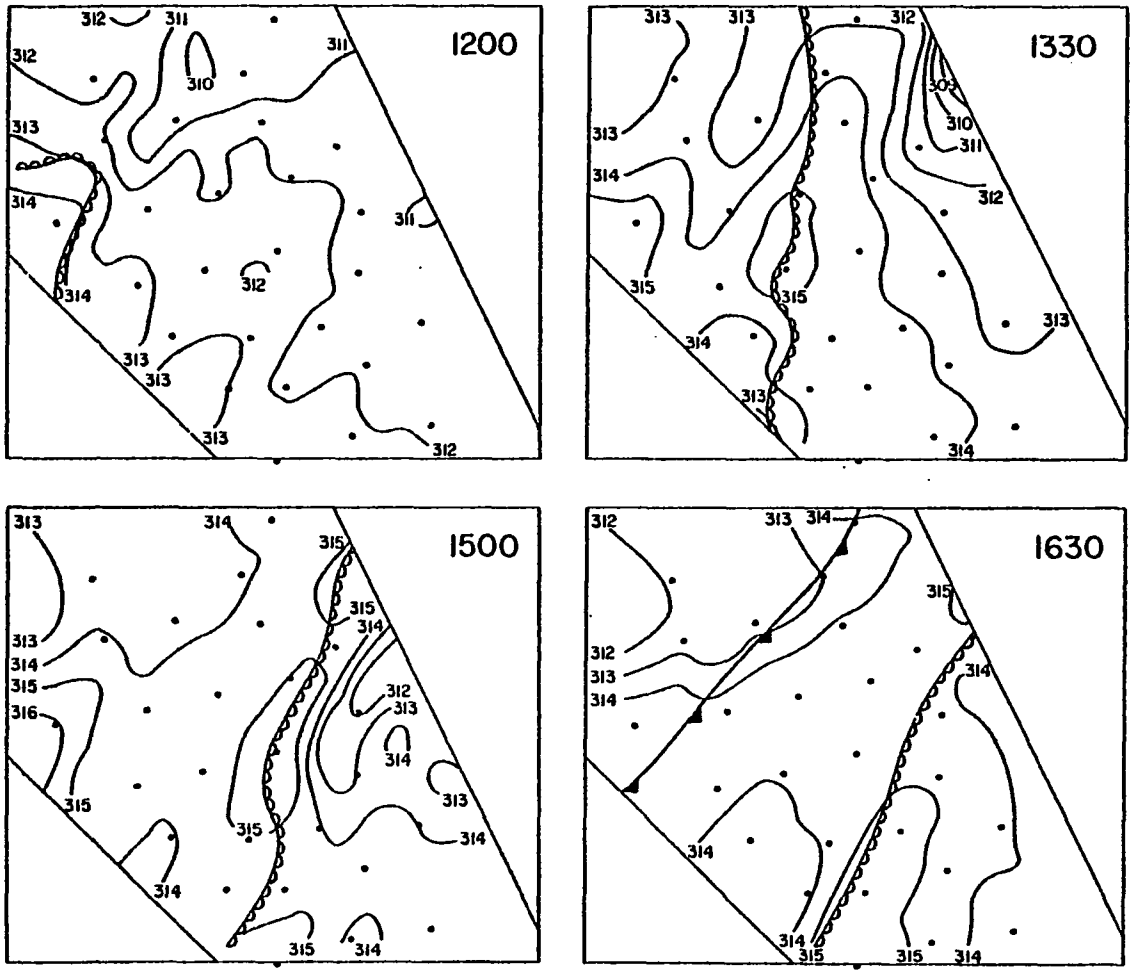

Fig. 8. Mesoscale objective analysis of θ_v(K) field at 90 min intervals, dryline, and weak frontal system.

density configuration dictates a nearly vertical dryline, which agrees with results of isentropic cross-sectional analysis of rawinsonde data (Fig. 3b).

The last feature of interest in Fig. 8 is the presence of a very weak frontal system at 1630 that eventually arrives at the stalled dryline by 1730. This system was also identifiable in the pressure and wind divergence analyses. All of the above observations will be considered in the construction of a representative mesoscale structure model later in Chapter VIII. However, they do little in explaining the formation of individual storm cells, to which attention is now directed.

III.d. The Waves Revealed by Mesoanalysis

Earlier it was mentioned that the storms of mesoconvective system II formed repeatedly over a small area inside the mesonetwork. In fact, each storm first echo appeared within a 15 km radius of a point located 8 km northeast of station NNE. In order to see whether the responsible trigger mechanism is reflected in the mesoscale surface fields, "static energy flux convergence" $[-C_p \underset{\sim}{\nabla}_H \cdot (\underset{\sim}{V} \frac{\partial \theta e}{\partial z})]$ was computed in the mesoanalyses. This parameter has been shown by Koch (1975) to be a good predictor of storm cell intensity, as it measures both the degree of potential instability ($\partial\theta_e/\partial z$) and the amount of low-level lifting ($\underset{\sim}{\nabla}_H \cdot V$) present. It can also be shown that this parameter measures the

convergence of total energy ($C_p \partial\theta_e/\partial z$) available to a convective system through condensational heating and evaporational cooling.

As an excellent approximation to the "static energy flux convergence", the quantity $[C_p \nabla_H \cdot (\theta_e \underset{\sim}{V})]$, called "energy convergence" for brevity, is computed in this work. All quantities are now evaluated from mesoscale surface data alone, assuming that the mesoscale variation of θ_e at the level of minimum θ_e (the mid-troposphere) is negligible. This assumption is justified since the minimum θ_e on the Norman and Ft. Sill soundings differs by only 0.6 K. Incidentally, objectively analyzed fields of this quantity exhibited very similar patterns to the more conventional fields of moisture convergence (Hudson, 1971).

Radar observations indicated that just as one storm cell of meso-convective system II grew to maturity, a new one would develop to its rear, this sequence being repeated periodically at about a 20 minute interval. It will now be shown that wavelike disturbances (positive anomalies) in the energy convergence field could be isolated as surface reflections of the apparent storm-triggering mechanism. However, because the dryline zone is a zone of energy convergence in the time-averaged sense, these disturbances are not as easily visualized in this field as in the relative vorticity and streamline fields. All of these fields are shown during one 60-min time sequence in Fig. 9.

It is acknowledged that these fields appear rather noisy upon first glance, yet in obtaining the position of each disturbance axis (depicted by a line segment), two constraints were imposed. It was of utmost importance first of all to have the disturbance phase velocity be nearly invariable during the course of tracking the individual vorticity anomalies; this continuity should be verified by the concerned reader in the case under discussion in Fig. 9. Secondarily of importance was the desirability of obtaining a fairly consistent locational relationship between the wavelike disturbances in the streamline, vorticity, and energy convergence fields. In practice, the disturbances were first detected as enhanced cyclonic curvature in the streamlines in the general confluence zone along the dryline, and then more exactly defined with the help of the vorticity analyses.

The problem in interpretation admittedly rests in the fact that, whereas these disturbances appear transverse in nature (wave crests oriented normal to both the dryline orientation and the mean boundary layer wind direction), yet the crests are not uniform or coherent in appearance, instead consisting of one or more discrete positive vorticity anomalies. This <u>apparent</u> lack of coherence should not be regarded as evidence for pure noise since virtually all of the anomalies displayed excellent spatial and temporal continuity, and it has already been shown in Appendix A that the

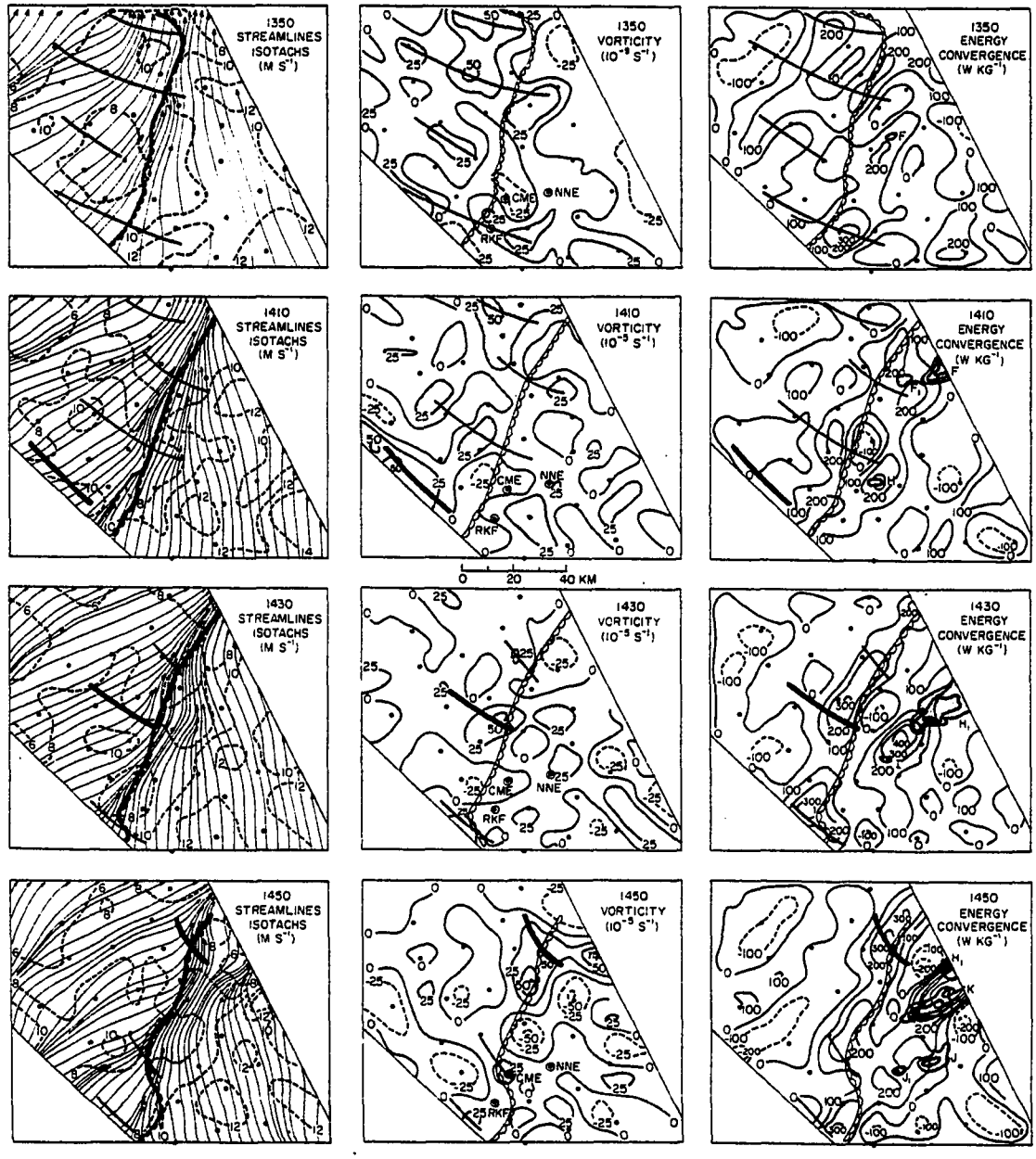

Fig. 9. Relationships between radar echo patterns, dryline, and wavelike disturbances in the streamline, relative vorticity, and energy convergence fields. Positive vorticity regions are shaded to aid in disturbance identification, particularly the one depicted by a very heavy line segment. Storm echoes are labelled as in Fig. 5.

time-to-space conversion technique can resolve these disturbances, whose apparent wavelength is roughly that of the $2\Delta n$ wave. The surface detection of the storm-triggering disturbances amounts to extracting a rather weak signal from a moderately high background noise level, but still within the limits of the analysis resolution capability. Because of this signal-to-noise ratio problem and the associated subjectivity involved at this point in determining the length of the wave crests in a NW-SE direction, a more objective statistical analysis of the station-to-station signal coherence must be made (see Chapters V and VI).

Despite these cautionary statements concerning the interpretation of the mesoanalyses, the apparent storm-triggering mechanism can be isolated in every case as a positive enhancement in the energy convergence field in association with a vorticity disturbance. In the case under consideration in Fig. 9, as the vorticity disturbance approaches the dryline from the southwest, energy convergence is enhanced locally within the dryline energy convergence zone, located 5-10 km behind the dryline, to values in excess of 200 W kg^{-1}. Storm cells I and K appear to form in response to the passage of the disturbance depicted with a heavy line segment. Notice that both the energy convergence zone along the dryline and the discrete maximum of

energy convergence immediately to the southwest of storm H_1 intensify as the disturbance passes by. If only the latter had intensified, it could easily be argued that this enhanced convergence was related to the strengthening circulation of storm H_1; however, because two separate areas of convergence were simultaneously enhanced, it is more plausible that some independent phenomenon has been detected. This was the case even when no radar echoes existed.

Such wavelike disturbances in the energy convergence field were found within 10 km distance to the southwest of the location of storm first echo in every case of new cell development, sometimes as early as 50 minutes prior to echo appearance. A typical lead time of 35 minutes was found, or roughly the time expected for a rapidly growing cumulus cloud to produce radar-detectable hydrometeors. Because these disturbances could be isolated at such an early time prior to radar first echo appearance, it is unlikely that they were merely reflections of the convection cells.

Although every MDLW is associated with a wave in vorticity, the converse is not true (it is not apparent from this data why this is so, since some of the strongest waves are not associated with MDLW). The frequency rose shown in Fig. 10 summarizes the intimate locational relationship between the MDLW and disturbances in the streamline (vorticity) field: the MDLW were almost always at or within 15 km

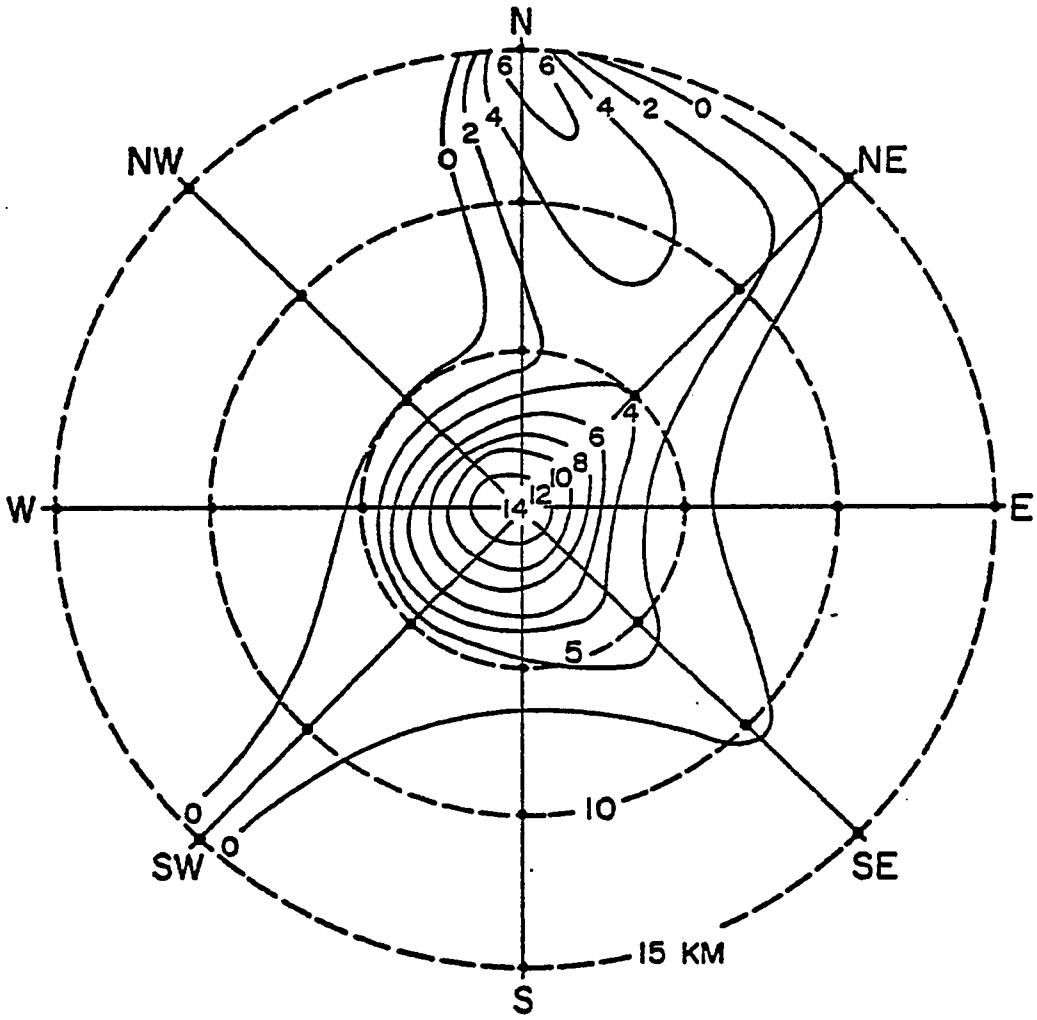

Fig. 10. Frequency rose depicting locational relationship between the axes of the MDLW (at center) and axes of the disturbances in the streamline (vorticity) field. Values indicate the number of occurrences of each "event", plotted at the indicated dots in polar coordinates (see Panofsky and Brier, 1968). An "event" occurs whenever an MDLW and an associated streamline disturbance coexist (these frequencies do not indicate the number of such disturbance pairs found, since each pair was followed for several map times).

upstream of the streamline disturbances.

The wave characteristics of the disturbances in the fields of energy convergence, vorticity, the streamlines, and moist static energy (MDLW) were determined by (1) measuring the wavelengths between successive disturbances at those times when multiple disturbances concurrently existed on the mesoanalyses, (2) calculating the average phase velocity $\overline{\underset{\sim}{c}}_p$ of each disturbance during its appearance over the mesonet, (3) determining the median wavelengths λ_{MED} from histograms of wavelength, and (4) calculating the mean periodicity from the relationship

$$\overline{T} = \frac{\lambda_{MED}}{|\overline{\underset{\sim}{c}}_p|} . \qquad (2)$$

The histograms were always unimodal and positively skewed. The results, summarized in Table 2, show very little variance between the fields, and so for comparisons later with the spectral wave characteristics, the streamline values are used.

The true wavelike nature of these mesoscale disturbances is easiest to visualize from a space-time cross section along a plane parallel to the mean trace direction of the disturbances. Such a composite is constructed from the vorticity analyses along line A-A' (see Fig. 6) for the 1100-1500 period, when the dryline was nearby, as shown in Fig. 11. The average "trace speed", i.e. horizontal phase

Table 2. Mean Wave Characteristics of Mesoscale Disturbances Obtained from Mesoanalyses

Field	Horizontal Phase Speed ($m\ s^{-1}$)	Propagation Direction (deg)	Median Wavelength (km)	Mean Periodicity (min)
Energy Convergence	19.6 (N=9)	219 (N=9)	20 (N=77)	17 (N=9)
Relative Vorticity	21.3 (N=9)	217 (N=9)	21 (N=76)	17 (N=9)
Streamlines	21.7 (N=9)	219 (N=9)	22 (N=76)	16 (N=9)
Moist Static Energy(MDLW)	18.3 (N=6)	205 (N=6)	*	*

* Too infrequent to be calculable

speed in the direction of wave travel, calculated from this diagram is $|\bar{\underset{\sim}{C}}_p| = 22.1$ m/s, in excellent agreement with the estimates above. Clearly waves can be found to the southwest of the dryline. Also important is that the waves are detectable up to 50 minutes prior to storm first echo.

Thus the mesoanalyses readily detect the apparent wavelike storm trigger mechanisms at least 35 minutes prior to radar-detectable precipitation, as well as revealing their characteristics. These results cannot be interpreted as numerical noise introduced as the result of the interpolation scheme, because of the unique ability of the time-to-space conversion technique to resolve the observed $2\Delta n$ waves, as clearly demonstrated in Appendix A. These analyses also indicate the source of the disturbances to be to

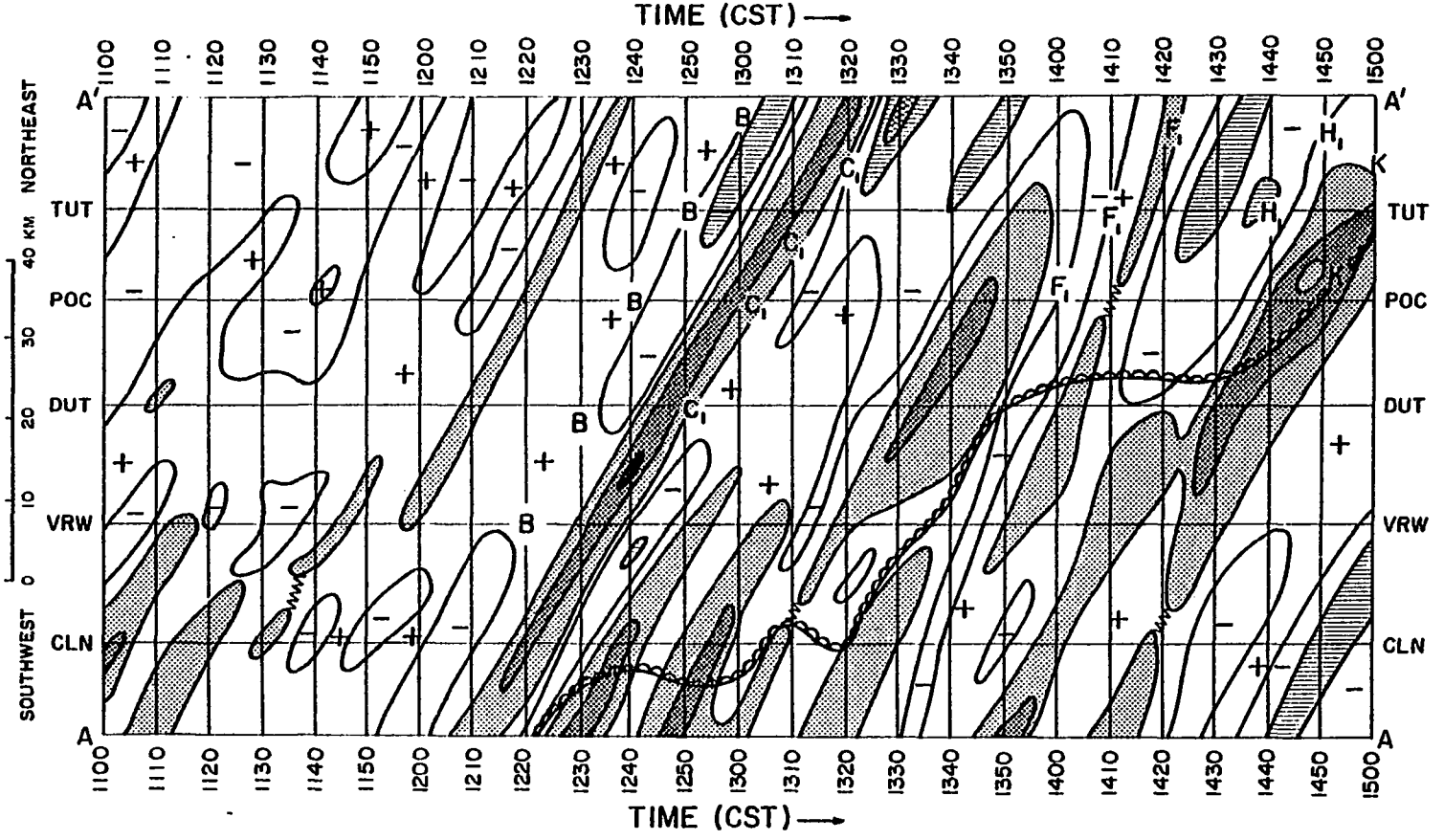

Fig. 11. Space-time cross section of vorticity along line A-A' of Fig. 6 during 1100-1500 interval. Positive vorticity values are stippled, negative are hatched at intervals of $25 \times 10^{-5} s^{-1}$. Trace speed determined by slope of the propagation path of each disturbance in this space-time framework. Short breaks in wave continuity are filled with zig-zag lines. Dryline and storm cell positions are indicated by scalloped line and alphabetic letters, respectively.

the southwest of the dryline. As the disturbances visible in the streamline/vorticity fields propagate towards the dryline, several events occur: (1) in some instances the dryline advances eastwards as a response to these disturbances, resulting in the appearance of an MDLW; (2) in all cases the energy convergence along the dryline is locally enhanced; finally, (3) each new storm cell apparently develops as the consequence of the passage of one of the mesoscale disturbances, but only when part of the energy convergence anomaly is able to break away from the dryline.

The isolation of the wavelike disturbance and its characteristics was a difficult matter because of its low signal-to-noise ratio. There is a real need to quantitatively verify these same features through an objective statistical analysis of the mesonet station data, and to determine how far to the east and west of the dryline that a coherent signal can be found. It will be useful at this point to review the theory of hydrodynamic instability to assist in the selection of pertinent parameters useful in this statistical study of the mesoscale disturbance dynamics.

CHAPTER IV

CONSIDERATIONS FROM CLASSICAL HYDRODYNAMIC INSTABILITY THEORY

IV.a. Hypothesis Testing and the General Theory of Hydrodynamic Stability

The general premise of this thesis is that the storm cells of meso-convective system II developed as the result of some hydrodynamic instability process that was manifested in the form of wavelike disturbances in the surface velocity field. Auxiliary to this premise is the belief that these observations are not characteristic of simple random turbulence, because the disturbances do not display high levels of diffusion, dissipation, or rapidly fluctuating vorticity (see Tennekes and Lumley, 1972). On the other hand, these phenomena do not represent simple, idealized wave motions involving dispersion rather than diffusion, but rather seem to possess an intermediate degree of structure characteristic of boundary-free turbulent shear flows.

Some general philosophical notions on hypothesis testing will be useful in determining which hydrodynamic instability theories are both testable and relevant for study.

If a particular method of analyzing and interpreting data is to lead to an explanation of the phenomena of interest, then the method must be based on tentative hypotheses about how those phenomena are interrelated (Hempel, 1966). Such hypotheses determine what facts are relevant to the investigation, and thus provide it with some direction. An acceptable hypothesis is one which fits the available relevant empirical findings, although no hypothesis can ever be inductively confirmed, but only lent some degree of support. For a given hypothesis to be of practical value in explaining the phenomena, it must currently have a number of "test implications" (theoretical predictions of observable events) by which observations can be analyzed to test the hypothesis. Although a currently untestable hypothesis may at some later time provide test implications, it would still be considered speculation for the present.

Such motions as those governed by quasi-geostrophic theory are thus irrelevant because the simplifying assumptions do not allow the creation of workable hypotheses which might explain mesoscale phenomena. Ekman layer and baroclinic-symmetric instability theories are also irrelevant because they predict longitudinal roll vortices that are clearly not in agreement with the mesoanalytical observations. It will be shown later how the vortex tube stretching mechanism of Barcilon and Drazin (1972), although perhaps relevant, is untestable.

Those tentative hypotheses that are both relevant and testable are to be formulated within the general theory of hydrodynamic stability as discussed in Lin (1955). The method of small disturbances (linearity) is, in its simplest form, applied to a two-dimensional mean flow ($\partial\bar{U}/\partial x << \partial\bar{U}/\partial z$), upon which wave disturbances are allowed to propagate. Disturbance streamlines are represented by

$$\psi(x,y,t) = \hat{\psi}(z)\ e^{i(kx + \ell y - \sigma t)}\ , \qquad (3)$$

where $k = 2\pi/\lambda_x$ and $\ell = 2\pi/\lambda_y$ are horizontal wavenumbers, $\sigma = \sigma_r + i\sigma_i$ is the complex frequency, σ_r is the circular frequency of the wave oscillation, and σ_i is the disturbance growth rate which, if positive, means the disturbance will amplify and the flow is thus hydrodynamically unstable to an infinitesimal perturbation. Wave phase velocity is given by $c_p = \sigma_r/k$. Veering of the ambient wind with height can be accounted for by considering the flow characteristics of the vector $\underset{\sim}{\bar{U}} = \underset{\sim}{i}u + \underset{\sim}{j}v$, and projecting this vector onto the relevant plane for stability analysis. For example, such considerations are made when analyzing the dynamic stability characteristics of the real atmosphere. Several tentative hypotheses within the framework of this general theory are now considered.

IV.b. Convective Instability

One hypothesis to be tested is that the mesoscale wavelike disturbances are not really waves at all, but

instead organized convective plumes resulting from a difference in density between the disturbance and its ambient environment. Conditional and potential instabilities are necessary but insufficient prerequisites for plume formation, as the intensity of convection is governed by the amount of buoyant energy available to it. Certainly the local storm environment in this case study meets these necessary conditions. Note that the type of organized convection under discussion here is not the deep convection obviously existing at the time of first radar echo; rather, the dynamical nature of the precursor "trigger mechanism" is to be understood.

If too strong a vertical wind shear or static stability is present in the atmosphere, only random forced convection is possible. Thus, other necessary conditions for organized convective plumes to occur involve critical values of both the Richardson number (a ratio of thermal to mechanical energies), defined as

$$Ri = \frac{\frac{g}{\bar{\theta}_o}\frac{d\theta}{dz}}{\left(\frac{d\bar{U}}{dz}\right)^2} \quad , \tag{4}$$

and the Rayleigh number Ra (a ratio of buoyancy to dissipative energies). In an analytical investigation of the hydrodynamic stability properties of a variable vertical shear flow in an unstably stratified fluid, Asai (1970) found that

for $-Ri > 10^{-1}$ and $Ra \geq 10^{3}$, a thermal convection mode slightly modified by the shear flow would develop. At lower -Ri, a transverse inertial instability slightly modified by buoyancy would preferentially develop; at lower Ra, only flat convective cells could occur. Vertical shear tends to suppress two-dimensional convection, whose central axes of ascending motion tilt with height in the direction of the mean shear.

The theoretical prediction that a longitudinal, fully three-dimensional convection is the preferred mode for values of $-Ri > 10^{-1}$ is apparently not in accordance with the mesoanalytical results which indicate a transverse mode (Figs. 9 and 11). However, an earlier discussion showed that this interpretation of these figures was still open to some question. Besides, the exact value of Ri is very uncertain when the static stability is so low.

The theory of convective instability presents several test implications by which this hypothesis may be evaluated. The first of these is that a quarter-wavelength phase lag should appear between fluctuations in pressure and horizontal wind when no vertical wind shear is present, since in this case the centers of low pressure and horizontal wind convergence are coincident. In the presence of vertical shear, the axis of the warm core aloft tilts downshear more than the updraft axis (Asai, 1970), in which case hydrostatic pressure falls at ground level should lead the horizontal

wind convergence. A second test implication is that fluctuations can only be detected by ground sensors when the circulations associated with the convective plumes are sufficiently deep and intense. A third test implication is a dynamical consequence of the second, namely that the plume dynamics are typically not hydrostatic in nature given that the aspect ratio A (A = disturbance width/disturbance height = λ_x/λ_z) is typically near 1 (Kunkel, et al., 1977). These three test implications need to be evaluated from the relevant available data to assess the merit of this hypothesis, and then considered in the light of the apparent discrepancy between theoretical and observed modes of activity. Specifically, the first two test implications suggest that a cross spectral analysis would be a very useful tool in these respects.

IV.c. Rayleigh Instabilities

This kind of hydrodynamic instability can occur in an inviscid, homogeneous fluid only if the velocity profile contains a point of inflection, and in particular when the condition that

$$\overline{U}'' \ (\overline{U} - \overline{U}_{IP}) \leq 0 \qquad (5)$$

holds everywhere within the flow, where $\overline{U}'' = \partial^2\overline{U}/\partial z^2$ or $\partial^2\overline{U}/\partial x^2$, depending upon the case under study, and $\overline{U}_{IP}$ is the mean flow speed at the inflection point (Gossard and Hooke, 1975). In the case of horizontally sheared flow, this

instability will occur when the absolute vorticity of the flow displays a maximum, as shown by Kuo (1949), whereupon this "vortex sheet" will rapidly spin up into tight vortices. Orlanski (1968) has shown that the amplifying disturbances have rather vertical orientations at Rossby numbers characteristic of mesoscale flows. However, they are also transient phemomena when $0 < Ri < 2$, thus when static stratification effects are included.

A more interesting situation arises when an unstable stratification ($Ri < 0$) is introduced, since the vertical vortex tubes resulting from horizontal wind shear may now couple with convective updrafts and intensify as angular momentum is conserved during the vortex stretching process. Barcilon and Drazin (1972) have advanced this hypothesis as a plausible explanation for microscale dust devil formation.

The theory has not been extended to date to include mesoscale flows of much lower Rossby number. Serious questions can be raised about the relevance of this hypothesis when vertical wind shear is appreciable. The vertical vortex tubes generated from horizontal wind shear would be tilted as a consequence of vertical shear of the horizontal winds. This process amounts to a transport of the turbulent vorticity by the mean flow, which becomes more significant at smaller length scales and lower Reynolds numbers (Tennekes and Lumley, 1972). It is difficult to say whether such a disrupting effect on organized vertical spin would be

significant at scales characterizing either the dust devil or the mesoscale disturbance. The theory also suffers from being analytically intractable because of the three-dimensional nature of the problem. Therefore, because the vortex stretching hypothesis is questionably relevant to the mesoscale and has not included the effects of vertical wind shear, this theory does not offer firm test implications specifically applicable to the problem under study.

Despite these problems, the earlier work of Kuo (1949) may be helpful in examining the tenability of the general Rayleigh instability theory for the 8 June 1974 situation. In his study of barotropic (inflection point) instability of a jet stream, a horizontal, nondivergent flow representative of synoptic scale motions was assumed, and effects of static stability or vortex stretching were not dealt with. Because of these approximations, the model expressions contain functions of the beta parameter ($\partial f/\partial y$), and thus predictions of both the shortest unstable wavelength and the tilt of wave axes are inapplicable to the present case. However, the basic physics of the conditions for wave amplification are the same, namely that where the curvature of the wind profile changes sign, vortex elements gain an acceleration in the direction away from their original positions if the initial displacement is large enough. Thus the model test implication that the wave phase velocity $|c_p|$ has a value between the minimum velocity in the jet

profile $\overline{U}_{MIN}$ and the value $\overline{U}_{IP}$ is relevant here as a test implication.

It will now be shown that this hypothesis is of some interest because the observations are in rough agreement with this one test implication. Returning to Fig. 11, it is apparent that the dryline zone serves as a local region of enhanced positive vorticity if one neglects those centers of vorticity directly associated with storm cells. The reasons for this are because there exists a general cyclonic curvature to the streamlines in this zone, and because there is also lateral cyclonic speed shear present due to the wind speed minimum there (see Fig. 9). In fact, a profile of the wind component along the basic flow made in a plane normal to the dryline reveals a jet doublet, one on either side of the dryline. Although this provides inflection points approximately halfway between the locations of the dryline and jet cores, the relative vorticity is maximized at the dryline because of the substantial effect of the curvature term in natural coordinates. Thus Rayleigh instability would most likely develop at the dryline instead of at the inflection points (notice that (5) is satisfied there since $\overline{U}'' > 0$ and $\overline{U} < \overline{U}_{IP}$). The wave characteristics summarized in Table 2 reveal phase speeds about twice as large as that predicted by the Kuo model, and thus are in fair agreement with theory. However, it seems that no existing variation on the basic Rayleigh instability theory can offer a

testable hypothesis that can be applied specifically to the mesoscale disturbance phenomena.

IV.d. Gravity Waves and the Theory of Dynamic Instability

It will be shown in this section that gravity wave theory offers a relevant hypothesis with many test implications by which the merit of the hypothesis may be evaluated from the observations. The classical analysis of dynamic instability, only one of several possible wave sources (see IV.d.(4)), dates back to Helmholtz (see Lamb, 1932), who studied wave motions along a surface of discontinuity in wind and density (potential temperature) along the vertical. This two layer model predicts that the interface is unstable to sufficiently short wavelengths, usually $\lambda_x < 10$ km for typical values of $\Delta\overline{U}$ and $\Delta\overline{\theta}$.

Recent investigations have found what appear to be long-wavelength gravity waves in the atmosphere. Herron and Tolstoy (1969) found 20-300 km wavelengths from correlations of surface pressure oscillations with upper tropospheric jet-stream winds. Radar observations of 15-30 km waves in an upper level frontal zone by Reed and Hardy (1972) were found to agree well with the wave characteristics deduced from ground microbarograph data by Hooke and Hardy (1975). Many other studies of this sort indicate that the origin of these waves is seemingly caused by dynamic instability in the jet stream, an hypothesis which has recently been given support from the continuous profile model of Mastrantonio,

et al. (1976).

It should be understood that Kelvin-Helmholtz waves differ from gravity waves in the following respects: (1) the horizontal scale of K-H waves is related to the vertical depth of a very small-scale anomaly in the ambient wind shear and/or density profiles that results locally in $Ri < 0.25$, (2) these waves approach the classical idealization of disturbances at the interface of a two layer fluid discussed above (Lamb, 1932), and (3) characteristically, they are isolated vertically to a rather small depth of the troposphere, which is not the case for gravity waves associated with the upper-level jet stream; hence K-H waves usually cannot be detected with ground-based microbarograph arrays. Gossard and Hooke (1975) show that nonlinearities develop in strongly amplifying gravity waves on the verge of "breaking", and that the wave-induced shears can become so great that Kelvin-Helmholtz instability sets in as well.

Gravity waves, K-H waves, and turbulence commonly exist also in the surface-based inversion most commonly observed at night. Microbarograph arrays and acoustic sounders have detected the characteristics of this wave activity as a combination of continual background "noise" with intermittent bursts of stronger oscillatory behaviour (Merrill, 1977). However, such low inversions can only support waves with horizontal wavelengths of at most a few kilometers. These waves can propagate for great horizontal distances, but very little

energy escapes upwards out of the duct often formed by the inversion. Most often a critical level can be found somewhere within the duct, although this does not always happen. Jones (1972) discusses how a duct serves as a wave guide so that only trapped gravity waves will be observed at large horizontal distances from the region of generation, and that only one or at most a few dominant long wavelengths out of the spectrum of dispersive waves will appear there if the wind shear is stable ($Ri > 0.25$). In the intrinsic framework (relative to the background flow), the ducted modes are confined to propagate perpendicular to the shear vector.

IV.d.(1) Phasing of Velocity-Pressure Fluctuations

These subsections describe various test implications derivable from the theory of gravity waves. From the linearized equations of motion, continuity, and energy conservation for adiabatic processes, Gossard and Hooke (1975) show that linear, homogeneous, partial differential equations can be formulated to describe the phasing of gravity wave variables. If η, u, v, w, ρ_o, and p denote small wave perturbations in a constant level surface, in the x,y,z components of wind, and in density and pressure, then the following set of Eulerian equations describe the state of a non-ionized, laminar, inviscid atmosphere:

$$\frac{Du}{Dt} + \frac{1}{\rho_o}\frac{\partial p}{\partial x} - fv = 0 \qquad \text{(u-momentum)}$$

$$\frac{Dv}{Dt}+\frac{1}{\rho_o}\frac{\partial p}{\partial y} + fu = 0 \qquad \text{(v-momentum)}$$

$$\frac{Dp}{Dt} - \rho_o g w + c_s^2 \rho_o \underset{\sim}{\nabla} \cdot \underset{\sim}{\overline{U}} = 0 \quad \text{(mass conservation)}$$

$$\left(\frac{D^2}{Dt^2}+N^2\right) w + \frac{1}{\rho_o}\frac{D}{Dt}\left(\frac{\partial}{\partial z}+\frac{g}{c_s^2}\right)p = 0, \quad \text{(energy conservation)}$$

where $D/Dt = \partial/\partial t + \underset{\sim}{\overline{U}}\cdot\underset{\sim}{\nabla}$ is related to the wave intrinsic frequency ω (see (13)) through (3) by

$$\frac{D}{Dt} = i(-\sigma + \overline{u}k + \overline{v}\ell) = -i\omega,$$

and f, c_s, and N are the Coriolis parameter, the speed of sound, and the Väisälä-Brunt frequency (see (12)), respectively.

If we neglect the earth's rotation (f = 0) and consider gravity waves with phase speeds much less than the speed of sound, then ρ_o can be eliminated between the equations of continuity and energy conservation by adopting the transformation

$$\zeta,\ U,\ V,\ W,\ P^{-1} = \left(\frac{\rho_o}{\rho_s}\right)^{\frac{1}{2}} [\eta,\ u,\ v,\ w, p^{-1}], \qquad (6)$$

where $\rho_o(z)$ is the variation of background density with height, and ρ_s is the density at the ground reference level. Then solutions of the form (3) require the following phasings:

$$P = P(z)\ \cos\ (ly)\ \sin\ (kx-\sigma t), \qquad (7)$$

$$U = U(z) \cos (ly) \sin (kx-\sigma t), \qquad (8)$$

$$V = V(z) \sin (ly) \cos (kx-\sigma t), \qquad (9)$$

$$W = W(z) \cos (ly) \cos (kx-\sigma t). \qquad (10)$$

Thus the theory predicts the test implications that both P and U, and V and W, are precisely in phase, whereas U and V, U and W, and P and W are 90° out of phase, in the intrinsic direction x. The presence of vertical shear in the basic flow ($\partial\underset{\sim}{\overline{U}}/\partial z$) projected onto the direction of intrinsic wave propagation distorts these precise relationships somewhat, although for reasonable values of $[\partial\underset{\sim}{\overline{U}}/\partial z)/k]$, the effect is quite small. Elimination of P(z), U(z) and V(z) leads to the familiar Taylor-Goldstein wave equation:

$$\frac{d^2W(z)}{dz^2} + \left[\frac{(Nm/k)^2}{[\overline{U}(z)-c_p]^2} - m^2 - \frac{\overline{U}''k}{[\overline{U}(z)-c_p]} \right] W(z) = 0, \qquad (11)$$

where $m^2 = k^2 + \ell^2$, $\overline{U}'' \equiv d^2\overline{U}/dz^2$, $c_p = \sigma/k$ is the phase velocity in the x direction, and

$$N = \left(\frac{g}{\theta_o} \frac{d\theta}{dz} \right)^{\frac{1}{2}} \qquad (12)$$

is the Väisälä-Brunt frequency. We have implicitly made the Boussinesq approximation, which requires that the scale depth of the atmosphere be large compared with the scale depth of the disturbance.

The intrinsic frequency is the wave frequency that an observer drifting with the background flow would see, and

is defined as

$$\omega = \sigma - k\underset{\sim}{\bar{U}} = k[\underset{\sim}{c}_p - \underset{\sim}{\bar{U}}(z)] = k\,\underset{\sim}{c}_\omega . \tag{13}$$

At the "critical level" where $|\underset{\sim}{c}_p| = |\underset{\sim}{\bar{U}}|$, the intrinsic frequency vanishes.

If no vertical shear is present, a polarization relation can be found between U and V, namely

$$\frac{U}{V} = \frac{k}{\ell} , \tag{14}$$

which provides that for waves propagating essentially in the x direction ($k/\ell > 1$), the amplitude of the U perturbations should be significantly larger than that of the V perturbations. This fact will have very important implications for the cross spectral study.

IV.d.(2) Prediction of Wave Phase Velocity

A second test of the gravity wave hypothesis is a direct comparison between observed and predicted values of the wave phase velocity. Gossard and Munk (1954) show that under the same assumed conditions as above, joint use of pressure and wind data can be exploited in determining the intrinsic wave phase velocity from the impedance relation

$$|\underset{\sim}{c}_\omega| = \frac{\omega}{k} = \frac{1}{\rho_s}\,\frac{P}{U} , \tag{15}$$

where U represents half the vector difference between extremes in the position of the total wind vector as it oscillates between crest and trough during wave passage, as shown

schematically in Fig. 12. A measure of wave signal-to-noise ratio is the degree of sign-independent correlation between U and P, consequently the sign on U must be treated consistently in determining the sense of the direction of wave propagation. The results of this calculation then allows an estimate to be made of the phase velocity from

$$\underset{\sim}{C}_p = \underset{\sim}{C}_w + \underset{\sim}{\bar{U}}\,(z). \tag{16}$$

An independent estimate of $\underset{\sim}{C}_p$ can be obtained as a consequence of the Wegener hypothesis prediction, which states that the direction of $\underset{\sim}{C}_p$ (namely θ_p) should be along the shear vector between the two atmospheric layers, and that its speed $|\underset{\sim}{C}_p|$ should be equal to the mean of the projection of the air speeds below and above the interface onto the direction of $\underset{\sim}{C}_p$. Although this prediction disregards details of the motion very near to the critical level, according to Gossard and Hooke (p.138), there exists "a fairly imposing body of observational data which supports the predictions of the theory." The predictive equations are, if subscripts 1 and 2 refer respectively to the lower and upper layers and u_o and v_o are the conventional wind components in the Cartesian coordinate system:

$$|\underset{\sim}{C}_p| = \tfrac{1}{2}[(u_{o1}\cos\beta^* + v_{o1}\sin\beta^*) + (u_{o2}\cos\beta^* + v_{o2}\sin\beta^*)], \tag{17}$$

$$\theta_p = \tan^{-1}\left(\frac{v_{o1}-v_{o2}}{u_{o1}-u_{o2}}\right). \tag{18}$$

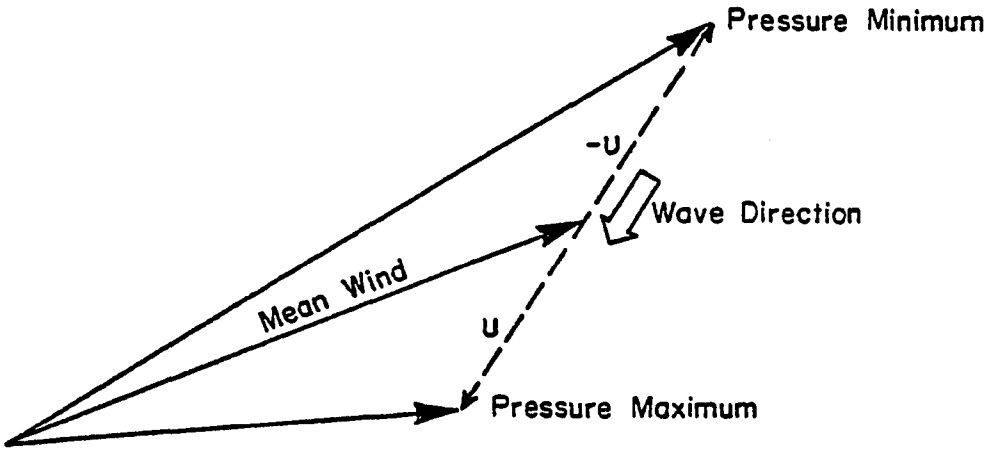

Fig. 12. Vector diagram illustrating how intrinsic wave phase velocity can be obtained from measured perturbations in the surface wind and pressure fields. The maxima in pressure occur under the wave crests and the sense of U at that time determines wave direction, so that P and U are in phase for waves propagating from the 180° sector to the left of the mean wind (after Gossard and Munk, 1954).

These equations require an a posteriori estimate of the wave propagation direction ($\beta^* = 270^\circ - \beta$), say from the mesoanalyses. The predictions maximize the projected speed difference, which means the orientation of the largest, fastest unstable wave predicted by the two layer model is specified by the Wegener hypothesis.

IV.d.(3) Wave Behaviour and the Conditions for Ducting

If the bracketed quantity in (11) is constant ($\equiv n^2$), vertical wind shear is neglected ($\overline{U}'' = 0$), and $\ell = 0$, then this equation yields simple plane-wave solutions of the type

$$W(z) = A\, e^{i(kx + nz - \sigma t)}. \tag{19}$$

Notice that if n^2 is negative, then n is of the imaginary form ($n = i\gamma$), and the waves are evanescent (trapped), dying off exponentially with height above or below the wave source height. However, if n^2 is positive ($n = \gamma$), then the waves will be untrapped, oscillating indefinitely with height.

The relationship between intrinsic frequency ω, horizontal wavenumber k, and vertical wavenumber n is derived by first noting that the bracketed quantity becomes

$$n^2 = \frac{N^2}{[\overline{U}(z) - c_p]^2} - k^2$$

which upon substitution from (13) becomes

$$n^2 = k^2 \left[\left(\frac{N}{\omega} \right)^2 - 1 \right], \tag{20a}$$

or

$$\gamma = k \left[1 - \left(\frac{N}{\omega} \right)^2 \right] . \tag{20b}$$

Thus an equivalent condition for evanescent wave behaviour is that $N/\omega < 1$.

An expression for the theoretical amplitude of the pressure perturbation at the ground (P_o) can be found in the linear, Boussinesq case from the expression relating P and vertical displacement ζ, namely

$$P = \rho_s |\underset{\sim}{C}_\omega|^2 \frac{\partial \zeta}{\partial z} . \tag{21}$$

Considering only the evanescent case, the profile of ζ will have the form

$$\zeta = \zeta_H \frac{\sinh \gamma z}{\sinh \gamma H} , \tag{22}$$

where H is the height of the gravity wave source. Upon differentiation and substitution of (22) back into (21) under the condition that $Z = 0$, it follows that

$$P_o = \frac{\rho_s |C_\omega|^2 \zeta_H}{H} \left(\frac{\gamma_1 H}{\sinh \gamma_1 H} \right) . \tag{23}$$

The set of equations (20a-23) will be used later to calculate a perturbation displacement profile needed to estimate the ability of evanescent gravity waves to initiate deep convection. This serves as yet another test implication of the hypothesis.

For the present, it is instructive to understand how the atmosphere acts as a "hydrodynamic filter" to allow detectable surface pressure perturbations only for sufficiently large ratios of λ_x/H. The strongest evanescent effect will occur when $N = 0$, thus when $\gamma = k$ $(=2\pi/\lambda_x)$. The filtering effect enters through the term $(\gamma H/\sinh \gamma H)$ in (23), and since $\gamma H = 2\pi H/\lambda_x$, then

$$\lim_{\gamma H \to o} \left(\frac{\gamma H}{\sinh \gamma H} \right) = 1,$$

or therefore P_o is maximized for $\lambda_x/H \to \infty$.

In many cases, this ratio is simply not large enough to permit ground sensing of the waves unless a low-level duct is present, as discussed earlier. Lindzen and Tung (1976) present four necessary conditions for a statically stable ducting layer to be able to partially reflect wave energy downward:

(1) Naturally, the duct layer must display static stability;

(2) Nowhere within the duct layer can there exist a critical level if everywhere $Ri > 0.25$, because otherwise wave momentum would rapidly be lost to the mean flow (Miles, 1961);

(3) The duct layer must lie beneath a partially reflective layer wherein the lapse rate is conditionally unstable,

there is a critical level, and Ri drops below 0.25 at some point;

(4) The duct must be sufficiently thick to be able to accommodate at least one quarter of the vertical wavelength λ_z corresponding to the observed value of $|\underset{\sim}{c}_p|$. This is calculated from

$$\lambda_z = \frac{2\pi}{n} = 2\pi \frac{|\underset{\sim}{c}_\omega|}{N}, \tag{24}$$

which follows from (20a) when $(N|\omega)^2 >> 1$. This criterion is necessary to guarantee that the lowest order wavemode with the longest wavelength is not badly attenuated by dissipative processes.

IV.d.(4) Determination of Wave Source Height

Before discussing methods by which the source height for gravity waves can be estimated, a clear understanding of possible wave source mechanisms is needed. Gossard and Hooke (1975) review many such sources: penetrative convection, Wave-CISK, density impulses, geostrophic imbalance, topographical forcing, and dynamic instability. It will now be shown that only the latter three mechanisms offer tentative hypotheses in light of the existing observations, and that only dynamic instability can be evaluated

with the available data.

Penetrative convection can act as a source for gravity waves when cumulonimbus towers penetrate the region of strong static stability at and above the tropopause. Acting essentially as a point source, the storm may generate concentric rings of internal gravity waves in a framework moving with the velocity of the storm. An observer on the ground should witness faster wave propagation downwind of the storm than upwind of it. However, no such systematic alteration of the phase velocity of the 8 June mesoscale disturbance was observed. Moreover, these phenomena appeared in a way strongly suggesting an origin far upstream of existing storms, since the disturbances were first detected along the southwestern border of the mesonetwork tens of kilometers upstream of the storms.

The theory of Wave-CISK (Conditional Instability of the Second Kind) has been successfully developed by Raymond (1975) to predict the continuous propagation of convective storms by modelling them as convectively forced internal gravity waves. The concept here is that the convection forces the gravity waves, which in turn organize the convection into coherent, amplifying patterns, but only when the wave and storm phase velocities are identical. The theory predicts that vertical motions are damped along the direction of the shear vector due to destructive wave interferences there. Although the observed mesoscale disturbances do have

a phase velocity (219°, 21.7 m/sec) almost exactly equal to the average storm propagation velocity (218°, 22.6 m/sec), they also travel essentially in the direction of the wind shear (220°). The same discussion as above concerning the apparent wave source region far upstream of existing convection applies here as a negative consideration for Wave-CISK.

Density impulses, such as accelerating cold fronts and thunderstorm outflow boundaries, both of which involve cold air masses of greater density than the air ahead, can generate trains of gravity waves downstream under some circumstances. The only air mass boundary in the apparent source region of the disturbance is obviously the dryline, yet the air density is essentially the same on either side of this boundary. No other thunderstorms exist upstream of the storms in Fig. 5 throughout the subsynoptic region.

Geostrophic adjustment is the process whereby an imbalanced system resulting from an impulsive addition of momentum to an initially flat, parallel, rotating current of finite width will return to a steady geostrophically-balanced state. In the excellent review of theoretical work by Blumen (1972), it is shown that inertia-gravity waves are generated as the means by which this process takes place. Although linearized models have shown the propagation of waves at right angles to the basic current when the mementum impulse is generated in the direction of the current, other geometries could conceivably result in other wave propagations.

Another complication rests in the highly dispersive nature of the waves, which comprise an entire spectrum of wavelengths limited by the Rossby deformation radius (typically of several thousand kilometers scale in the atmosphere). Insufficient subsynoptic-to-mesoscale rawinsonde data is available for 8 June 1974 to resolve such a momentum impulse (e.g. a propagating jet streak). Thus, depsite the likelihood of this hypothesis as being relevant for further consideration, it is untestable with the existing data.

An unsteady momentum field may also generate progressive lee waves, or gravity waves, upon encountering a mountain barrier. According to Gossard and Hooke (1975, p.359), "very little is currently known about the effectiveness of this mechanism as a source of progressive waves" because lee wave theory to date has only dealt with a steady-state ambient wind field, although the transient development of lee waves to a steady state has been considered. Consequently, the generation of waves not fixed to the topography remains a speculative, and thus untestable, hypothesis.

Despite this problem, it is of some interest to observe that should such waves be created, they would quite likely be trapped within the mid-tropospheric inversion layer (Fig. 3b), and therefore would propagate for a long distance downstream of the forcing topography. Such forcing is very doubtful over Oklahoma since the terrain consists of only gently rolling hills no higher than 2000 ft above the

local surroundings, so the Rocky Mountains are the most likely candidate. The ducting capability of this inversion to the lee of the Rockies can be appreciated with the classical lee wave equation

$$\frac{d^2W}{dz^2} + \left(k_s^2 - k^2\right) W = 0 \ ,$$

where

$$k_s = \left[\left(\frac{N}{C_\omega}\right)^2 + \frac{\bar{U}''}{C_\omega}\right]^{\frac{1}{2}}$$

is the "Scorer parameter" and k is the wavenumber of the mountain topography. Clearly an atmospheric structure characterized by an elevated layer of maximum k_s^2 is needed in order to support a ducted internal gravity wave. Notice that k_s^2 is large for conditions of either strong static stability (N) or strong curvature in the ambient wind profile ($\bar{U}''$). Since both of these conditions exist within this inversion layer, and k_s^2 is so small in the mixed layer beneath where $N \doteq 0$, then a ducting phenomenon seems plausible. Numerical studies confirm the idea that wave amplitudes are stronger when the lower (mixed) layer displays such weak static stratification.

In summarizing, none of the possible gravity wave sources thus far considered pass both tests of hypothesis testing (relevance and testability) and can, in addition, be evaluated with the available data. It is very unfortunate

that the plausible geostrophic imbalance and topographical forcing mechanisms cannot be evaluated with the available data, and thus the source of the hypothesized gravity waves cannot be assuredly determined in this case study. However, the dynamic stability characteristics of the mesoscale environment about the dryline can be examined for relevance, and is very testable. Thus the means whereby the height of the possible dynamic instability may be estimated is now discussed.

Assuming linear, homogeneous, and frictionless flow, then restrictions are imposed on the generation of gravity waves resulting from dynamic instability. The growth of the waves depends upon the relative importance of destabilization by the wind shear compared to stabilization by the static stratification, as measured by Ri (see (4)): if $Ri > 0.25$ everywhere within the flow, then insufficient kinetic energy is extracted from the shearing wind to overcome the negative buoyancy. Theoretical work (Miles, 1961) indicates that it is a necessary, although perhaps not sufficient, condition for Ri to fall below 0.25 at, or very near to, the height of a "critical level" (that altitude where the horizontal phase speed of the wave equals the ambient wind speed in the plane of wave propagation) for unstable modes to be possible. These conditions can be evaluated from the subsynoptic rawinsonde data.

In addition to determining the dynamic stability

characteristics of the atmosphere in this case study, other calculations will help provide insight into the probable height of the assumed wave source. An analysis of time-height data obtained from an instrumented tower nearby the mesonetwork should reveal whether there is any possibility of a wave duct in the lower atmosphere. Wave momentum and energy fluxes can also be calculated from the tower data, existing thoughout the lowest 444 m of the atmosphere, which can provide an answer to the question of whether the source is above the tower.

The vertical profile of wave momentum flux defined as

$$F_M = \rho_o(z)\ \overline{UW}^{\lambda}, \tag{25}$$

can provide considerable insight into the likely source of the wave momentum (the overbar here represents an average taken of the UW eddy correlation over at least two horizontal wavelengths). The reason for this is that the background flow loses momentum to the waves at the point where there is a vertical divergence of wave momentum flux:

$$\frac{\partial \overline{U}}{\partial t} \cong -\frac{\partial}{\partial z}(\rho_o \overline{UW}^{\lambda}). \tag{26}$$

When ducted modes exist, the constructive resonance of the waves results in a zero mementum flux. Gossard and Hooke (1975) point out that several different interpretations of the direction of wave momentum flux are possible for any

given result. For example, $F_M > 0$ can be interpreted as (a) an upward flux of wave U-momentum if $C_\omega > 0$, (b) a horizontal flux of wave W-momentum if $C_\omega > 0$, or (c) a downward flux of wave-U-momentum if $C_\omega < 0$.

It can be shown when no vertical wind shear is present (Gossard and Hooke, 1975) that

$$W = -\frac{\omega n}{\rho_s (N^2 - \omega^2)} P. \tag{27}$$

For an evanescent wave ($n = i\gamma$), W and P are 90° out of phase; therefore the energy flux, defined as

$$F_E = \overline{PW}^{\lambda}, \tag{28}$$

is zero; thus wave energy is lost very rapidly outside of a very confined region surrounding the point of wave generation. An observation at a given level that $F_E < 0$ implies that wave generation occurs above this level.

An independent estimate of F_E is both useful and advisable as a check on the quality of the estimate using (28). This second estimate is based upon the impedance relation (15):

$$P = \rho_s |\underset{\sim}{C}_p - \underset{\sim}{\overline{U}}(z)| \, U,$$

and thus upon insertion into (28) we have

$$F_E = |\underset{\sim}{C}_p - \underset{\sim}{\overline{U}}(z)| \, \rho_s \overline{UW}^{\lambda} = |\underset{\sim}{C}_\omega| F_M. \tag{29}$$

The estimates (28) and (29) should be in close agreement, and in fact the vertical energy and momentum fluxes must have the same sign when $|\underset{\sim}{c}_p| > |\bar{U}|$.

IV.d.(5) Summary

Of all the various hypotheses considered that have foundations in the general theory of hydrodynamic stability, only two are found to be both relevant and testable: thermal plume theory and gravity wave theory. The two hypotheses predict different phasings between U and P, different aspect ratios, and different stability characteritistics of the background medium as related to Ri. These different test implications then amount to three crucial tests of the two hypotheses.

The gravity wave hypothesis offers the most test implications, in addition to those above, by which its merit can be evaluated from the available data. Thus the research methodology will be designed in such a manner as to examine these test implications. This methodology amounts to (a) an estimation of the expected wave amplitude at the ground using (23), subject to the complications that might arise if the conditions for wave ducting (Lindzen and Tung, 1976) are met; (b) a comparison of observed mesoanalysis and predicted values (using (15), (17), and (18)) for wave phase velocity; and (c) a statistical determination of the U and V phase relationship, to be compared with the prediction from

(8) and (9). A source for the gravity waves will be sought by estimating the dynamic stability characteristics of the dryline environment. Should instability conditions be found, this experiment can be deemed successful at finding necessary conditions for the occurrence of gravity waves, although other sources cannot be ruled out (like geostrophic imbalance and topographical forcing); if the conditions are not found, then the results will be inconclusive. The vertical profiles of calculated wave momentum and energy fluxes will be useful as an independent guide in determining wave source altitude. Finally, a wave amplitude profile using (22) will be calculated to determine the ability of the gravity wave to actually initiate deep convection.

Combinations of various instabilities have not been considered here. One example of such a sophisticated theory is stratification-modified Rayleigh instability, treated numerically in a three-layer model by Gossard and Moninger (1975). The existence of an inflection point (see (5)) results in a transverse wave mode within a statically neutral boundary layer, but below a strong inversion such as the one in Fig. 4a. Depending upon the ambient conditions, a host of modes with differing k/ℓ ratios are predicted to evolve, although instability analysis shows one to be dominant for any given set of conditions. The mesonetwork is too small to allow a longitudinal mode ($k/\ell < 1$) to be detected. For the purposes of this research, it seems best to attempt to

explain the observations using the simplest hypotheses, if at all possible. More complicated explanations will not be considered unless simpler explanations fail.

The U and P, and U and V phase relationship tests indicate that a cross spectral and bandpass filter analysis of the mesonetwork data would be in order. These topics are discussed in the next chapter, along with limitations imposed by the measurement systems.

CHAPTER V

TECHNIQUES FOR ISOLATING THE WAVE CHARACTERISTICS

In this chapter, a discussion of the resolution and response characteristics of the sensors employed both in the mesonetwork and on the instrumented tower is given to assess the practical problems in using the mesonet pressure data and in obtaining the wave energy flux profile. Then, following a description of the cross spectral analysis techniques and the effects that assumptions inherent to the techniques has upon physical interpretations, two stages of spectral investigation are discussed. The determination of which parameters and record lengths to choose for these analyses is shown to be a direct consequence of the constraints imposed by the instrumentation and spectral techniques. The chapter closes with a discussion on the methods by which the various phase relationships and phase velocity of the wavelike mesoscale disturbance can be most accurately estimated.

V.a. Instrumentation Limitations

Performance characteristics of all sensors employed both in the mesonetwork (NSSL, 1971) and on the instrumented tall tower (Carter, 1970; Mazzarella, 1972) are given in

Appendix B. "Resolutions" quoted there probably refer to a combination of bias, absolute accuracy, hysteresis, and repeatability errors (definitions appear in Gill and Hexter, 1972). It may seem that a major problem exists in the 22.5° resolution of the wind vane system resulting from the discrete sampling nature of its recording mechanism. However, the Stephens pre-filter (Fig. 2) greatly reduces the undesirable variance in this data.

A very unfortunate resolution problem exists in the mesonet microbarograph system. Because a recording range of 2.5 in Hg was used, the read-off error is $\pm$ 0.01 in Hg ($\pm$ 0.3 mb), or about twice the width of the recording pen curve. Except for pressure anomalies of magnitude 0.4 mb or larger (usually associated with storm activity), in practice it was very difficult to ascertain the physical meaning of pressure fluctuations appearing in the digital data. It was often impossible to distinguish meteorological events from fluctuations apparently caused by Bernoulli-effects or an unsteady pen device in the original analog trace charts. For comparative purposes, a more ideal system for gravity wave studies is that used by Gossard (1960), namely a highly amplified microphone with chamber leaks on either side of the diaphragm to filter out both very long and short wavelengths.

As a result of this microbarograph problem, very little should be expected to result from cross spectral analysis of the mesonet pressure data. Any calculations directly

involving observed pressure oscillations, such as the impedance relation (15) or the amplitude equation (23), would likely be meaningless. Consequently, one of the crucial tests involving P and U phasings cannot be reliably performed. Instead the spectral test of the gravity wave hypothesis will have to rest upon the U and V phasings. Because $V/U < 1$ as implied earlier by (14), a rather large amount of scatter in the results might be anticipated. It is crucially important to realize that because of microbarograph problems, this thesis cannot employ the customary methods of testing the gravity hypothesis, i.e. utilizing the impedance relation and testing the degree of P-U correlation (Gossard and Sweezy, 1974; Uccellini, 1975; Merrill, 1977).

Problems also exist in estimating the energy flux profile using (28). Despite the superior performance specifications of the WKY-TV tower sensors compared to the corresponding mesonetwork sensors, the vertical resolution is hardly adequate for profile construction. Horizontal wind speed and direction, vertical wind speed, and dry and wet bulb temperatures were recorded at three instrumented levels in 1974 ($z_1 = 89$m, $z_2 = 266$m, $z_3 = 444$m), pressure was recorded only at the z_1 and z_3 levels, and both incident radiation and rainfall at only z_1 (Goff and Zittel, 1974). Thus it is impossible to construct a profile using (28) unless assumptions are made regarding the vertical variation of pressure (Chapter VII).

All of the tower data are linearly interpolated and extrapolated to 10 evenly spaced grid points in the vertical at 10 second time intervals, subjected to 60 passes of a two-dimensional (time-height) Shuman filter (Haltiner, 1971, p. 270) to smooth out undesirable high frequency fluctuations, and then contoured for display using the computer program of Goff (1975). The filter is designed to have a -3 dB point (71% response) at $f = 0.033\ f_{NY}$ (10 minute period), and no more than a 13% amplitude response for periods shorter than 4 minutes.

Calculated responses of the mesometeorological sensors to atmospheric waves of various periods (Appendix B) reveal that no significant problems should exist with the wind-measuring sensors. For waves of 15-20 min period observed from the mesoanalyses, small amplitude reductions and phase shifts can be expected for the other sensors. Major problems should occur in the interpretation of higher frequency phenomena. In any case, negligible energy exists in that part of the spectrum following application of the Stephens pre-filter (Fig. 2).

V.b. Cross Spectral Analysis Techniques

A cross spectral analysis of the mesonet data should be useful in the study of the wavelike characteristics of the mesoscale disturbance: its spatial coherence downstream, the frequency or period of the fluctuations, the phase

relationships and coherences between variables measured at any given station, and the horizontal extent of disturbance activity over which the phase relationships remain consistent. It is assumed that the reader is familiar with the basic principles of autospectrum analysis and has access to the formal mathematical definitions of the spectral statistics. The discussion can then be centered upon the various assumptions inherent to cross spectral analysis techniques and the constraints placed upon physical interpretations.

To explain the meaning of the cross spectrum in terms of a physical example, let us assume for illustrative purposes a steadily-propagating wave detected by a network of stations strung out equidistantly along the propagation vector $\underset{\sim}{C}_p$. If the time series for some parameter at station X_1 is taken as the "base series" to be crossed with the corresponding series at stations downstream along $\underset{\sim}{C}_p$, then for a perfectly sinusoidal wave of wavelength λ_x, the series at the station a distance of $(X_1 + \lambda_x/4)$ will be 90° out of phase with that at station X_1, the series at a distance of $(X_1 + \lambda_x/2)$ will be 180° out of phase, and so forth downstream until a full cycle is completed at a distance of $(X_1 + \lambda_x)$. These fluctuations in phase φ appear as maxima in the quadrature spectrum $Q_{12}(f)$ when $\varphi = 90^\circ$ and maxima in the cospectrum $L_{12}(f)$ when $\varphi = 0^\circ$.

In reality the detected waves will not be regular for a number of reasons. If the wave cycles are irregular,

or some stations lie on the fringes of the wave path, or the wave signal is immersed in a great amount of "noise" contamination from other phenomena, the degree of relatedness between the two series in question will be reduced. In moving farther and farther away from station X_1, the time series will appear less and less like those at X_1 (even with proper time lagging to line them up as well as possible) until eventually there is absolutely no correlation between them. The quantitative correlation between any two time series is expressed in terms of the normalized absolute value of the cross spectrum, called the coherence

$$\varkappa_{12}(f) = \left[\frac{L_{12}^2(f) + Q_{12}^2(f)}{C_{11}(f)C_{22}(f)} \right]^{\frac{1}{2}} , \qquad (30)$$

where the subscripts refer to the two series, and the quantities in the denominator are the individual autospectra. Thus, in moving farther downstream from X_1, the value of $\varkappa_{12}(f)$ decreases from 1.0 to essentially 0.0.

The relative phase angle between oscillations of frequency f determined from the spectra is

$$\varphi_s = \tan^{-1} \left[\frac{-Q_{12}(f)}{L_{12}(f)} \right] . \qquad (31)$$

Because the confidence in the phase estimate increases with the squared coherence (Jenkins and Watts, 1968, p. 379), the phase relationship for large station separation, when $\varkappa_{12}$

fluctuates about zero (see (36a) below), has no meaning.

The squared coherence is completely analogous to the square of the familiar correlation coefficient, except that it applies to the frequency regime. Although it is usually assumed that the presence of an isolated peak in the coherence spectrum presupposes the existence of at least one wave type whose frequency is near to that of the peak, this is not always the case. Leakage of variance from frequency bands of high variance density to other regions is a problem for both autospectrum and coherence spectrum interpretations. Because of the convolution of a lag window with the autocorrelation function, "side lobes" of variance will appear around isolated peaks in the autospectrum, and in a much more complicated way in the coherence spectrum due to the nature of (30). Another type of problem unique to the coherence analysis is the introduction of bias to the coherence estimate as the result of leakage of variance from low frequencies to higher frequencies in highly autocorrelated "red noise" data (Duchon and Goerss, 1977). Thus it is conceivable that even quite irregular (nonoscillatory) data could produce a number of coherence peaks that appear to have significance.

In order to prevent these serious leakage problems, the time series must be subjected to high-pass filtering prior to spectrum analysis. The time series analyzed in

this study are those of:

(1) u - the east-west wind fluctuations

(2) u^* - the wind fluctuations in the direction of estimated intrinsic wave propagation

(3) v^* - those wind fluctuations normal to u^*

(4) p - static pressure fluctuations

(5) θ_e - moist static energy fluctuations

A second-order least squares polynomial was fit to each of the above kinds of series to remove data trends, and hence the undesirable "red noise" variance contribution to leakage. Even after application of the detrender, most of the coherence spectra involving θ_e or p, and a few of the velocity spectra, still showed strong evidence of leakage problems resulting from extreme levels of "red noise". To further alleviate the leakage problem, a high-pass difference filter that produces a new time series y(t) from the original x(t) series as

$$y(t) = x(t) - x(t-1) \tag{32}$$

was applied. Jenkins and Watts (1968) show that this filter has the properties that (1) its response slowly decreases from unity at the Nyquist frequency ($f_{NY} = \frac{1}{2}\Delta t$) to zero at zero frequency, (2) no phase changes result when the filter is applied to both of the time series under analysis, and (3) meaningful peaks at very low frequencies will not be lost.

This filter was only applied in cases of autocorrelation exceeding 0.95 or strong coherence peaks at $f < 0.03$ cycle/min (the peaks of interest are in the $0.03 < f < 0.11$ range).

The cross spectrum results from taking the Fourier transform of the windowed cross-covariance function (a Tukey window was used in this study). This function usually has an asymmetric character about lag zero. It is highly desirable to align the two time series such that the maximum cross-covariance occurs at lag zero prior to taking the transform (Jenkins and Watts, p. 399). If this is not done, significant bias will be introduced into the coherence spectral estimate as the result of the convolution of the symmetric Tukey window with the asymmetric function. This operation was performed, but only in clear-cut cases involving a strong peak in the cross correlogram.

It is necessary that the confidence intervals be acceptably small before fine detail in the various spectra can be considered significant. For the Tukey window used here, the relationships between the 80% confidence interval (CI), the spectral bandwidth of the window (b_1), and the degrees of freedom (ν^*) are

$$CI = \pm\ 1.30\ \nu^{*-\frac{1}{2}}, \tag{33}$$

$$b_1 = 1.33/(M-1), \tag{34}$$

$$\nu^* = 2.667\ \frac{N}{M}, \tag{35}$$

where M is the maximum lag used in the autocovariance calculation and N is the record length. Notice that as M is increased, both b_1 and ν^* decrease, while CI increases. Ideally, b_1 should be chosen such that it is always smaller than the width of the finest detail of interest in the coherence spectrum; however, in practice this usually produces an unacceptable variance in the spectral estimate, and thus spurious peaks will appear that mask the true spectral peaks. The familiar problem of tradeoff between low bias (high fidelity) and small variance (high stability) is a consequence of using the lagged-product method of computing spectra, and necessitates examining several cases of various M/N values (a process called "window closing"). Almost all of the spectra in this study use M/N ratios of 0.2-0.3, or 9-13 degrees of freedom.

Jenkins and Watts (1968) show that the smoothed phase and coherence spectra are subject to <u>variance</u> caused by small values of ν^* and $\bar{\kappa}_{12}^2$ (low coherence implies a large noise level):

$$\text{Var}\ (\bar{\varphi}_{12}(f)) = \frac{1}{\nu^*}\left[\frac{1}{\bar{\kappa}_{12}^2(f)} - 1\right] , \qquad (36a)$$

$$\text{Var}\ [|\bar{\kappa}_{12}(f)|] = \frac{1}{\nu^*}\left[1-\bar{\kappa}_{12}^2(f)\right]^2 . \qquad (36b)$$

The estimates of the smoothed phase and coherence spectra are also subject to <u>bias</u> as determined by the particular choice of ν^* and spectral window. For the coherency, this bias is

given by

$$B[|\bar{\kappa}_{12}(f)|] = \left[\frac{2}{\nu^*} + \frac{|\bar{\Gamma}_{12}(f)|^2 - |\Gamma_{12}(f)|^2}{\Gamma_{11}(f)\Gamma_{22}(f)}\right]^{\frac{1}{2}}, \quad (37)$$

where $\Gamma_{11}(f)$ and $\Gamma_{22}(f)$ are the theoretical autospectra, and $\bar{\Gamma}_{12}(f)$ and $\Gamma_{12}(f)$ are the smoothed (windowed) and raw theoretical cross spectra. This equation predicts that the mean smoothed coherency can be large even if the theoretical cross spectrum is zero. Since $\Gamma_{12}(f) = \bar{\Gamma}_{12}(f) = 0$ for two independent white noise processes, the offset bias value must be taken into account in the employment of confidence intervals. Incidentally, this is not the case in autospectral analysis because the autospectral estimator is an unbiased estimator of white noise. To reject the null hypothesis that a given peak in the coherence spectrum is not significantly different from the white noise expectation at the 80% level of confidence, the peak's coherence must exceed the sum of the bias offset plus positive confidence limit values as calculated from (33), (35), and (37).

Jenkins and Watts (p.379) remark that the coherency should be plotted on a transformed scale

$$\bar{K}_{12}(f) = \tanh^{-1}|\bar{\kappa}_{12}(f)|$$

in order for the confidence intervals (33) to be represented by a frequency-independent constant interval. This is a consequence of the fact that the variance of the coherency

estimate (36a) is identical to the variance of a linear correlation coefficient if the effect of smoothing is disregarded.

An example of one of the computed coherence spectra plotted on such a scale with the appropriate bias value and confidence limits is presented in Fig. 13. In this case a difference filter and $\nu^* = 9$ degrees of freedom were used. This particular spectrum displays two of the most significant peaks found in any of the spectra without problems relating to "window closing". The peaks at $f = 0.096$, 0.163, and 0.250 min^{-1} all pass the 80% confidence limits, and are separated from adjacent peaks by a frequency interval larger than the spectral window bandwidth. Although quite pronounced peaks also appear at $f > 0.3$, such peaks were always disregarded, because they were evidently the result of leakage (notice the intervals of $\Delta f \cong b_1$) and application of the Stephens filter. The latter effect can be anticipated because the normalization involved in calculating coherence spectra from cross amplitude spectra depends on the values of $C_{11}(f)$ and $C_{22}(f)$, which are extremely low upon applying the filter, so that very weak spectral peaks could be amplified in the process.

In the results to be described in the next chapter, spectral statistics are shown for those peaks which meet the following criteria: (1) they are statistically significant at the 80% level or higher, (2) they are separated from adjacent significant peaks by a frequency gap exceeding b_1, and

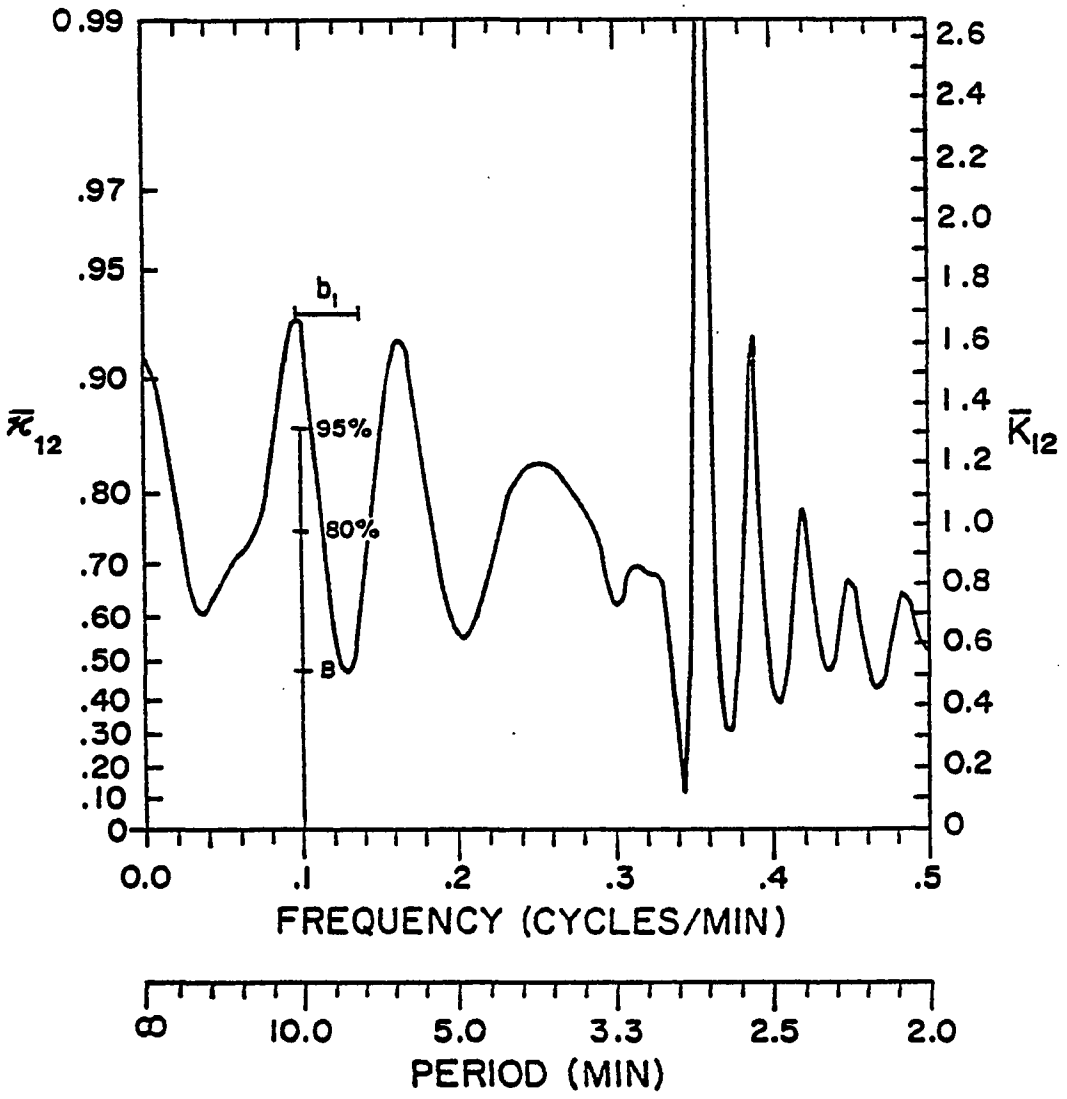

Fig. 13. Example coherence spectrum of u^* vs v^* time series from station POC. Notice bandwidth b_1 and a priori confidence intervals plotted above estimated bias B of white noise process against $\bar{K}_{12}$ scale.

(3) they are not evidently the result of side lobe leakage or variance problems produced at large M/N ratios. The general philosophical approach concerning the physical meaningfulness of the coherence peaks is the same as that used by Wallace (1971): for a group of spectra to be considered as separate realizations of the same stochastic physical process, they must exhibit similar phase relationships in that (those) frequency band(s) wherein significant coherences are mutually found. The idea here is thus to calculate a large number of coherence/phase spectra and examine the variance in the results in the hope of finding some general frequency band in which consistent phase relationships exist.

The term "stochastic physical process" should not be misunderstood to mean a purely random process. As shown by Jenkins and Watts (1968), a stochastic process provides a probabilistic description of changing physical phenomena. Any given time series is, in statistical analysis, regarded as being only one of an infinite ensemble of functions which might have been observed had the sampling conditions been slightly different. It is because the atmosphere is not totally deterministic, and data records are necessarily finite in length, that spectral methods must be used, rather than Fourier harmonic analyses, to study the stochastic nature of the atmosphere.

A few words should be said regarding the problem of aliasing before the description of how the cross spectral

techniques are to be specifically applied to the mesonet data. Aliasing of high frequency energy existing in the data at $f > f_{NY}$ back into the spectrum at lower frequencies may be a problem if Δt is chosen so large that the variance density is not effectively zero at $f > f_{NY}$. Application of the Stephans pre-filter to all data prior to spectral analysis effectively avoids the problem of aliasing because this filter has a -3 dB point at $f = 0.5 f_{NY}$. Some aliasing of energy to moderately high frequencies in the range $0.33 < f < 0.50$ min^{-1} would have resulted from increasing Δt by data decimation (a sometimes desirable enterprise to expand the lower frequency spectral domain and thus permit easier detection of spectral peaks there), but this would have required doubling the record length. Considerations of statistical stationarity and physical interpretations, discussed below, could not permit any reduction in record length.

V.c. Applications to Mesonet Data

The cross spectrum analysis is divided into two phases of investigation: "preliminary" and "primary". The purposes of the "preliminary study" are (1) to see whether coherent signals in the u time series can be followed along predetermined propagation tracks between stations; (2) to determine whether a frequency band can be distinguished for the purpose of constructing a bandpass filter; and (3) to obtain an independent check on the mesoanalytical estimate

of $|\underset{\sim}{C}_p|$. There is no attempt made at this stage to determine the consistency of the phase estimates in the given frequency band, should such a band be found. Ideally, a search for coherent signals should be made in the pressure time series rather than the u time series, however this is impossible because of the microbarograph problems.

It will be shown in the next chapter how the bandpass filter analysis of the u^* time series data is very helpful in the determination of which stations and record segments to subject to cross spectral analysis in the "primary stage". However, it is necessary to have some idea of which frequency band Δf_o this filter should be centered upon. For this reason, the u time series are used as a preliminary guess with the expectation that Δf_o will be nearly identical whether u or u^* is used. This guess is shown to be an excellent one in the next chapter.

Cross spectra of the u time series between stations are computed along each of 5 predetermined tracks, using data from the southwesternmost station as the "base series" (except when no significant coherence is found, then the next station downstream is used as the base). Those zones wherein frequent mesoscale disturbance activity was seen essentially determines the location of these tracks. Since the tracks of fluctuations in relative vorticity, energy convergence, moist static energy, and presumably pressure as well, were nearly always along the 219° azimuth, the orientation of the

tracks is chosen in this direction. An additional study of the tracks of all positive anomalies in relative vorticity and energy convergence showed that there were several other such active zones. Remember that substantial activity consistently appeared along the dryline zone. During the period 1100-1350, active tracks could be found running from FTC to ELR and from ASW to MNW. During the 1350-1730 period (includes meso-convective system II), active tracks could be found running from RKF to TUT and from RSE to DBS.

These first guesses at which tracks and periods to use are modified to account for possible undesirable effects of statistical nonstationarity upon the spectral results. As shown by Wallace (1971), this would lead to a reduction in coherence caused by fluctuations in the two time series having appreciably different amplitudes and phase relationships during different segments of the data record. In order to optimize the information existing in any given segment of the data, it is desirable to omit from consideration any period during which storm influence was obviously being felt at any station; after all, it is the purpose of this thesis to examine only the precursor storm-triggering mechanisms. Since any changes in the mean or variance in the data will affect the stationarity, any data recorded after the passage of the weak frontal system (see Fig. 8) is also disregarded, the static stability and hence turbulence characteristics of the atmosphere there being

somewhat different. The 5 tracks shown in Fig. 14 are along the 219° azimuth, being primarily determined by the anomaly track study, but modified for the effects of stationarity.

The purposes of the "primary stage" of study are (1) to determine the phase relationships between u^* and v^*, and perhaps also u^* and p, and u^* and θ_e; and (2) to determine the degree and nature of spatial coherence of the wavelike disturbance. The u^* time series data are first subjected to bandpass filter analysis, with maximum filter response in the Δf_o band, to aid in the determination of which records to spectrally analyze so as to optimize the information existing in this data. An estimate of the intrinsic wave propagation direction is prerequisite to this study, as discussed in Chapter VI. It will be shown that the Δf_o band found in both the "preliminary" and "primary" stages of spectral inquiry are identical, and that the best estimate of $|\underset{\sim}{c}_p|$ is obtainable from the "preliminary" study because of the greater number of stations located a greater distance apart.

The manner by which the mesonet stations are classified according to their location with respect to the dryline is as follows: if at least 75% of the record length under spectral investigation took place within the "dryline zone" ($\pm$ 10 km of dryline location), then that record is considered to be taken "along the dryline" (otherwise it is either "east" or "west" of the dryline).

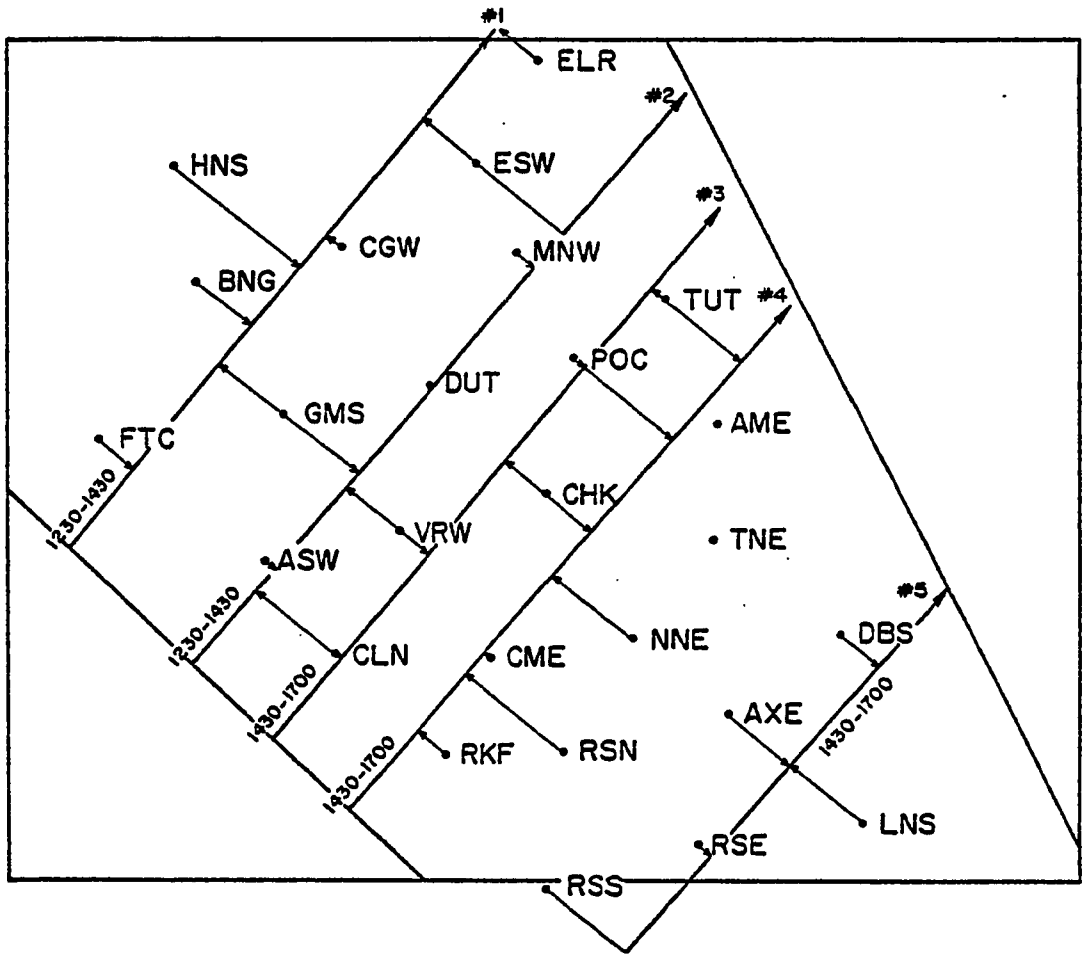

Fig. 14. The five tracks considered for cross spectrum study of the u time series between stations in the "preliminary stage" of investigation. Arrows at the ends of the light lines denote which stations are involved in each track of study.

V.d. Estimation of Phase Angles and Phase Velocity

In general, the coherence values of significant peaks were not as high as those in Fig. 13, and so a significant variance in the phase estimates is anticipated from (36a). In the "primary stage" of investigation, the first guideline in choosing the record is the appearance of the mesoscale disturbances over a given station. This record length is then modified to include only the presence of moderate amplitude, regular oscillations in the bandpass u^* time series. The final record length takes into account those meteorological conditions (dryline, weak frontal system, storm locations) that could have affected the statistical stationarity of the data. Despite these refinements in N, some variance in $\bar{\varphi}_{12}(f)$ must still remain because of the necessity to extend the record length somewhat beyond the limits imposed above so that a sufficiently large N could be obtained (say $N > 100$).

Because of these problems it is highly desirable to impose some additional constraint on the phase estimation to reduce the scatter in the spectral estimates of phase angle φ_S (the same as $\bar{\varphi}_{12}$). It is possible to obtain another estimate of the phase angle from analysis of the bandpass cross correlograms, say φ_{BP}. It is shown in Appendix C that the chosen bandpass filter possesses high fidelity and does not significantly alter the phases of any Fourier harmonics within the time series. Unquestionably both φ_S and φ_{BP} are

subject to errors caused by irregularity in the waveform and limitations imposed by the measurement systems (like poor pressure data or small V/U amplitudes). However, φ_{BP} is subject neither to bias nor uncertainty caused by high variance, and is thus the preferable estimate, if $|\Delta\varphi| = |\varphi_{BP} - \varphi_S|$ is within certain set limits. The method by which φ_{BP} is obtained is as follows: if α^* represents the closest positive 95% significant maximum in the cross correlation function to lag $\alpha = 0$, then for a wave of period T the phase angle is

$$\varphi_{BP} = -2\pi \left(\frac{\alpha^*}{T} - 1 \right) . \tag{38}$$

The determination of the wave phase velocity $\underset{\sim}{C}_p$ calculated from the spectral analyses depends upon the phase relationship of the u time series between any two stations under study. This calculation is performed to satisfy one of the purposes of the "preliminary stage" of spectral analysis. It can be accomplished by comparing the time delay of the disturbance between the stations obtained from the meso-analyses (τ) with that time delay calculated from the phase spectra (τ^*). If S represents the distance between stations along the direction of $\underset{\sim}{C}_p$, then

$$\tau = S/|\underset{\sim}{C}_p|, \tag{39}$$

and from the phase spectra

$$\tau^* = T + \frac{\varphi_S}{2\pi f} . \tag{40}$$

Notice that the constraint $T \geq \tau^*$ must be imposed to guarantee that no more than one wavelength exists between the stations, which would otherwise admit ambiguity in the interpretation. The comparison between the mesoanalytical estimate of $\underset{\sim}{C}_p$ and the spectral estimate is then made by computing the fractional difference

$$[(\tau - \tau^*)/T] \times 100.$$

CHAPTER VI

RESULTS OF STATISTICAL ANALYSES OF THE MESONET DATA

VI.a. Preliminary Cross Spectrum Results

The statistically significant results of the cross spectral analysis of the u time series between stations appears in Fig. 15 in histogram form. These results, from all of the spectra irregardless of the station locations relative to the dryline, indicate that coherent signals can be followed along the direction of $\underset{\sim}{C}_p$ ($219^\circ \pm 8^\circ$) between many stations.

The histogram is bimodal, suggesting two physical modes of activity, namely a high frequency mode centered near 5-6 minutes and a low frequency mode of 9-25 minute period centered near 15 minutes. The average period of the low frequency mode ($\overline{T} = 15$ minutes) is in excellent agreement with the results of the mesoanalyses presented earlier in Table 2. These results indicate that the bandpass filter should be constructed so as to have a fairly high response within a 10-30 minute band.

The last purpose of the "preliminary stage" of spectral investigation was to check the mesoanalytical estimate

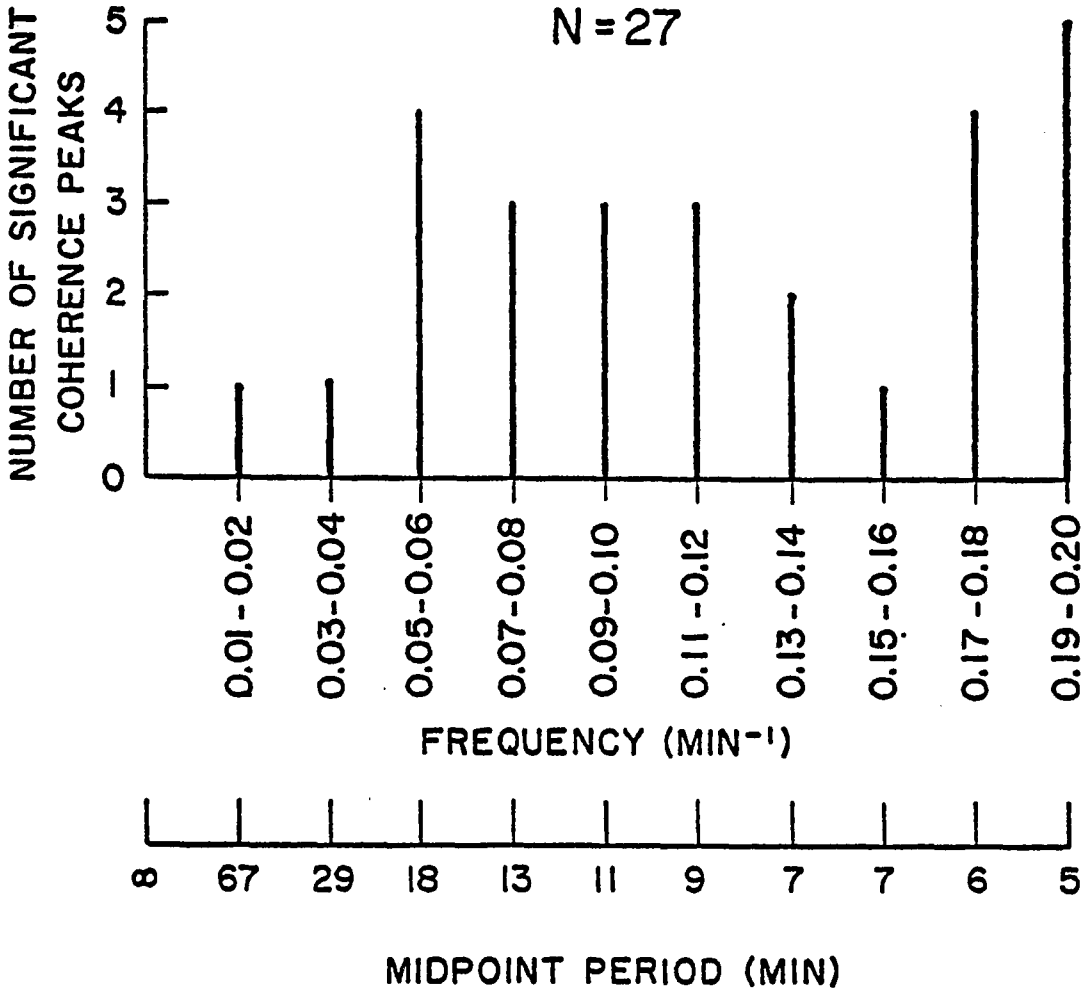

Fig. 15. Histogram plot of 80% statistically significant results from "preliminary stage" of coherence spectral study involving u time series between stations. Altogether 22 pairs of stations displayed 27 significant spectral peaks.

of $|\underset{\sim}{c}_p|$. Evaluation of (40) is made only for the low frequency mode. Imposing the constraint that $T \geq \tau^*$ reduces the sample to 6 cross spectra. This limited test upon $(\tau-\tau^*)$ confirms that the previous estimate of $|\underset{\sim}{c}_p| = 21.7$ m/s ($\pm$ 2.9 m/s) is at most 1% different from the spectral estimate, a quite insignificant difference. It should be recognized that this method of comparison implicitly assumes that the wavelength is known a posteriori from the mesoanalyses, but because of the excellent agreement in both mean wave period and phase speed, this assumption is certainly justified.

VI.b. Bandpass Analysis and Estimate of Intrinsic Velocity

Based upon the results of the "preliminary stage" of cross spectral analysis, a bandpass filter is constructed with the aim of achieving unit response at $T = 15$ min, at least a -3 dB response for $10 \leq T \leq 30$ min, and a sharp cutoff for higher frequencies so that the undesirable mode ($T < 10$ min) does not pass through the filter. The bandpass filter is constructed from the very fine low-pass filter of Lanczos (1956), in which the undesirable Gibbs oscillations are strongly damped by the use of σ factors (see Appendix C for details of its construction and testing). The resulting filter response comes very close to meeting the ideal requirements, as seen in Fig. 16.

It would be interesting at this point to test the

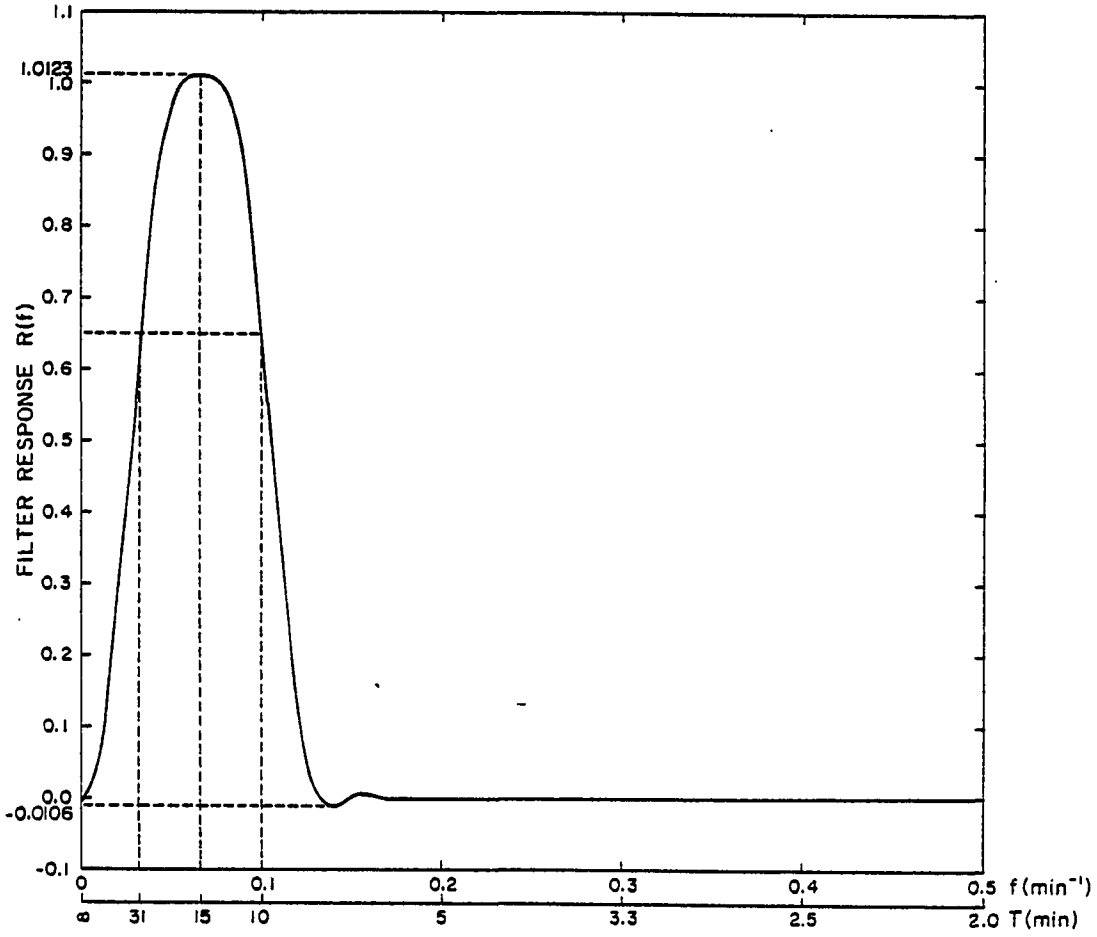

Fig. 16. Bandpass filter selected for use. Notice strongly damped Gibbs oscillations at $f = 0.15$ resulting from σ-smoothing (see Appendix C).

relationship between φ_S calculated from (31) and φ_{BP} calculated from (38). Those stations which contributed to the results of Fig. 15 were subjected to a spectral analysis of their u time series crossed with their v, θ_e, and p time series. The low frequency peaks in these coherence spectra are used as the basis by which the comparison of φ_S to φ_{BP} is made, altogether involving 17 spectra. This comparison is illustrated in Fig. 17, which shows that 88% of the cases lie within the bounds $|\Delta\varphi| < 45^\circ$. Using this criterion, perhaps 2 of the cases would be rejected, and the φ_{BP} values of the other 15 used as best estimates of the phase. These results are very encouraging, because both methods of phase estimation give very similar results. Moreover, there is now an additional basis for conducting a pilot study of the bandpass u^* time series as an aid to determining which portions of the data to subject to the "primary stage" of spectral analysis.

Before this pilot study can be made, an estimate of the intrinsic phase direction θ_ω is needed. It will be shown here that the speed $|\underset{\sim}{C}_\omega|$ is fortunately not required at this point. If θ represents the observed wind direction, $|\underset{\sim}{V}|$ represents the observed wind speed ($\underset{\sim}{V} = \underset{\sim}{i}u + \underset{\sim}{j}v$), and $\theta^*_\omega = 270^\circ - \theta_\omega$, then

$$u^* = |\underset{\sim}{V}| \cos(\theta_\omega - \theta) = u \cos\theta^*_\omega + v \sin\theta^*_\omega \qquad (41)$$

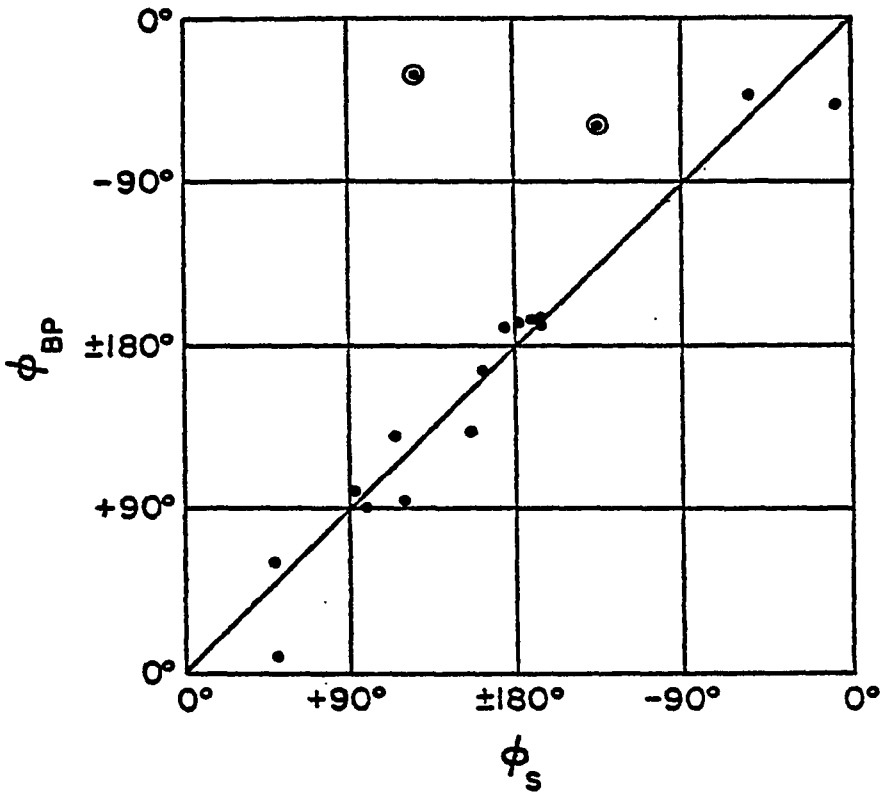

Fig. 17. Relationship of bandpass phase estimate φ_{BP} to spectral phase estimate φ_S for those 17 coherence spectra in which significant low frequency peaks were found. Circled data depict cases that do not meet the $|\Delta\varphi| < 45°$ criterion.

is simply the projection of $\underset{\sim}{V}$ onto $\underset{\sim}{C}_\omega$, and

$$v^* = |\underset{\sim}{V}| \sin(\theta_\omega - \theta) = v \cos \theta^*_\omega - u \sin \theta^*_\omega \qquad (42)$$

is the component normal to u^*. It should be recognized that u^* (the estimate of U defined in (15)) is either in the same or exactly opposite direction as $\underset{\sim}{C}_\omega$, but will not in general have the same magnitude as $\underset{\sim}{C}_\omega$ (see Fig. 12).

The first step in the determination of what records of which stations to study is to find those periods during which noticeable vorticity "wave" activity is present, subject to those meteorological constraints discussed earlier. These periods are listed in the second column of Table 3.

The second step is to plot the one-minute interval, Stephens-filtered wind data during these periods in a conventional Cartesian coordinate system to see whether the wind vector oscillates back and forth in the linear manner shown schematically in idealized form in Fig. 12, and thus allow an estimate of θ_ω to be made. Examples of acceptable and unacceptable station records of equal length appear in Figs. 18 and 19, respectively. The wind vector in the acceptable case oscillates back and forth in a manner which is linear in a statistical sense. In fact, there seem to be two loci of activity as might be expected if the ideal concept in Fig. 12 were actually being realized here (such loci were present in most of these cases). Plots of the oscillating wind vector offer a simple intuitive look at

TABLE 3

DETERMINATION OF RECORD LENGTHS FOR CROSS SPECTRAL STUDY
AND ESTIMATE OF INTRINSIC PHASE DIRECTION

MESONET STATION	TIMES OF PRONOUNCED: VORTICITY 'WAVES'[1]	BANDPASS u^* ACTIVITY[2]	PERIOD FOR COHERENCE ANALYSIS	POSITION RELATIVE TO DRYLINE	θ_ω (DEG)	$2\|u^*\|$ (KNOTS)	SIGNIFICANCE $r_{uv} > 2.60_r$	$r^2_{uv} > 0.25$	F Test
AME	1530-1650	1515-1615	none	Along	---	---			
ASW	1230-1430	1210-1415	1210-1415	Along	308	27	x	x	x
AXS	1510-1730	none	none	East	---	---	x		x
BNG	1300-1350	1300-1350	1245-1425	West	310	20	x	x	x
CGW	1250-1350	none	none	West	---	---			
CLN	1320-1520	1320-1410	none	West	---	---			
CME	1440-1620	1345-1520	1345-1545	Along	299	25	x	x	x
DBS	1540-1720	none	none	East	---	---			
DUT	1330-1600	1505-1600	1440-1630	West	313	19	x	x	x
ESW	1330-1410	none	none	West	---	---		x	
GMS	1230-1430	1330-1410	none	West	---	---			
HNS	1320-1400	none	none	West	---	---			
LNS	1420-1730	1615-1730	none	East	---	---			
MNW	1320-1415	1320-1405	1320-1500	Along	292	22	x	x	x
NNE	1510-1630	none	none	Along	---	---			
CHK	1320-1410	none	none	Along	---	---			
	1520-1630	none	none	West	---	---			
POC	1420-1600	1420-1600	1440-1630	Along	310	37	x	x	x
RKP	1340-1610	1300-1440	1300-1600	Along	312	25	x	x	x
RSE	1510-1730	none	none	East	---	---			
RSN	1440-1610	1450-1610	1440-1620	Along	292	20	x	x	x
RSS	1400-1610	1410-1450	none	East	---	---			
TNE	1520-1640	1530-1640	none	East	---	---			
TUT	1510-1650	1500-1630	1500-1640	Along	302	19	x	x	x
ELR	1340-1420	none	none	Along	---	---			
FTC	1230-1430	1220-1430	1220-1430	West	315	23	x	x	x
VRW	no recorded wind data								

[1] Meteorological constraints imposed (positions of dryline, storms, and weak frontal system are taken into account).

[2] These are periods of quasi-periodic oscillations in u^* of at least moderate amplitude, under same constraints as above, but also using additional constraint imposed by time period during which vorticity 'waves' were present.

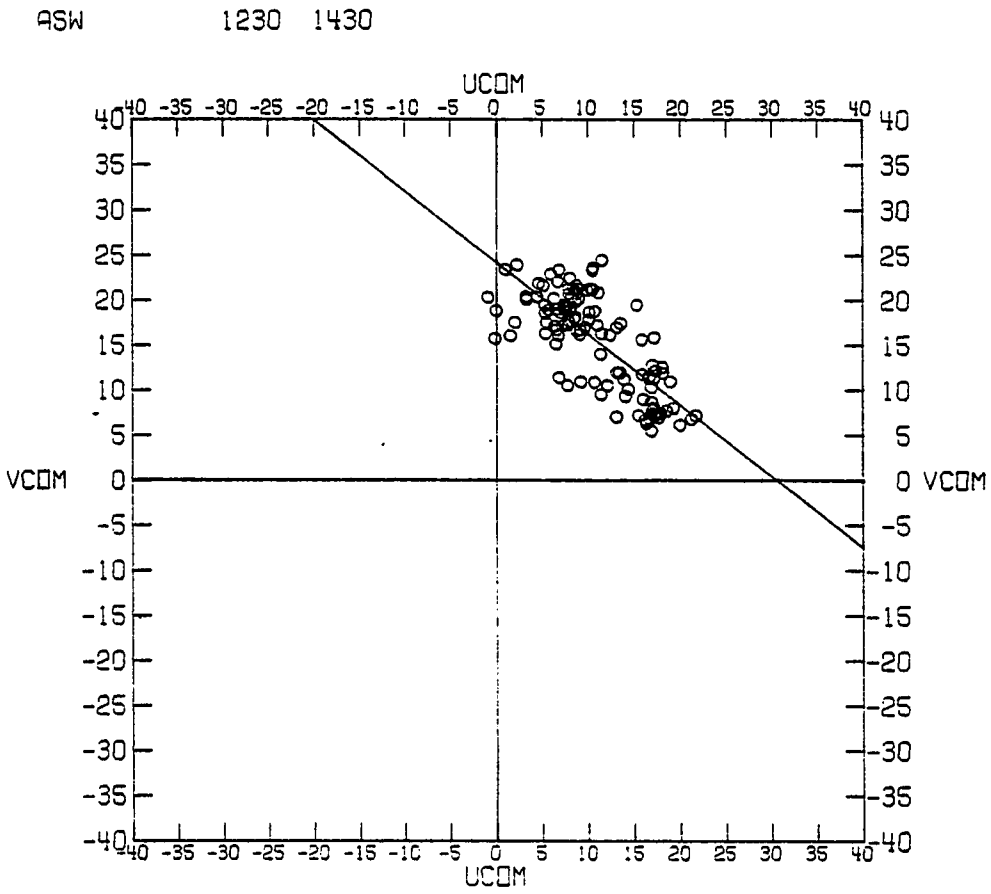

Fig. 18. Example of acceptable station for illustrating linearly oscillating wind vector. UCOM and VCOM are the u and v wind components from station ASW during 1230-1430 period. Statistically significant line of regression determined by least squares method is displayed.

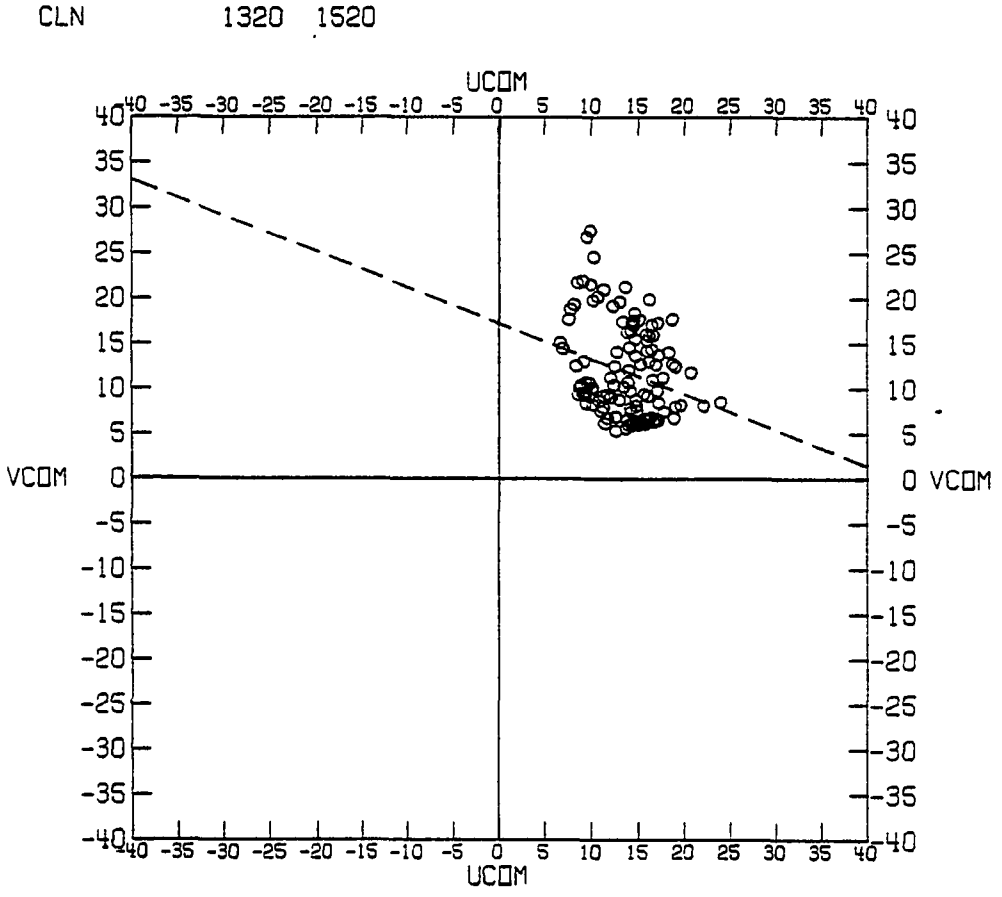

Fig. 19. Example of unacceptable station which did not pass statistical tests of linearity. Computed least squares line is shown. Same format as in Fig. 18.

wavelike motions in the atmosphere, as well as being the basis by which the choice is made of which stations to subject to additional spectral analysis.

Three tests of statistical significance of the linear correlation between the u and v wind components must have been passed for a station record to be chosen for the spectral analysis. In two tests involving the magnitude of the correlation coefficient r_{uv}, the null hypothesis is first made that the correlation between the u and v populations is zero, and then the probability that the observed r_{uv} could be due to accidental sampling fluctuations is determined (Panofsky and Brier, 1968). Thus, the first test to be passed is that

$$r_{uv} > 2.6\ \sigma_r,$$

where

$$\sigma_r = \frac{1}{(N/3-1)^{\frac{1}{2}}}$$

is the standard deviation of a theoretical population with zero correlation between randomly selected pairs of data, and whose distribution is assumed normal; in the formula for σ_r, N is divided by 3 to account for the fact that successive samples of meteorological data are usually so positively correlated that the assumption of statistical independence is violated. Then, if this test is passed, the

probability of these data being random is less than 1%. The second test involving r_{uv} is that

$$r_{uv}^2 > 0.25,$$

which dictates that at least 25% of the total variance is accounted for by the linear correlation. The third requirement is that the scatter of data points about the line of regression not be so large that the F-test described in Panofsky and Brier (1968) is not passed; this last test measures the goodness of fit of the line to the data.

The importance of these tests should not be overlooked, as they determine which station records are to be studied further, and therefore play an important role in the amount of scatter, and consequently, interpretation of the cross spectral results. It is noteworthy that following application of these testing criteria, only ten of the records remain (Table 3), none of which come from stations "east of the dryline". Apparently, the mesoscale disturbance activity, if it is of the nature of gravity waves, does not appear as a strong signal east of the dryline where the low-level static stability is the strongest (see Fig. 3b)! The ten stations for study display very nearly the same θ_ω and $|u^*|$ values, with means of $\theta_\omega = 305^\circ$ ($\pm 8^\circ$) and $|u^*| = 6.1$ m/s ($\pm$ 1.3 m/s).

Upon employing the θ_ω value into (41) and (42), and

subjecting the resulting time series of u^* to the bandpass filter, the final choice of which record lengths to use in the "primary stage" of spectral investigation is made. Notice that the resulting periods in Table 3 are, in most cases, a little longer than those periods of strong signal in the bandpass u^* time series. This extension of the periods is made in order to obtain a sufficient number of data points for spectral analysis. It is significant that whenever tests of linear correlation were passed, strong bandpass signals could always be found. In the gravity wave study conducted by Uccellini (1975), it was assumed that the presence of strong bandpass signals implied wave activity. However, it is evident in Table 3 that such is not always the case.

VI.c. Primary Cross Spectrum Results

For each of the ten candidate stations, a cross spectrum was computed between the u^* and v^*, u^* and p, and u^* and θ_e time series. A histogram plot in Fig. 20 of the significant results from spectra of all the parameters substantiates the double mode of activity previously found in the "preliminary" stage of inquiry. The center of the low frequency mode is again at a 15-16 minute period, and the Δf_o band is also very similar.

The relationships between wave period and phase are shown in Fig. 21 for the significant peaks in the u^* vs v^*

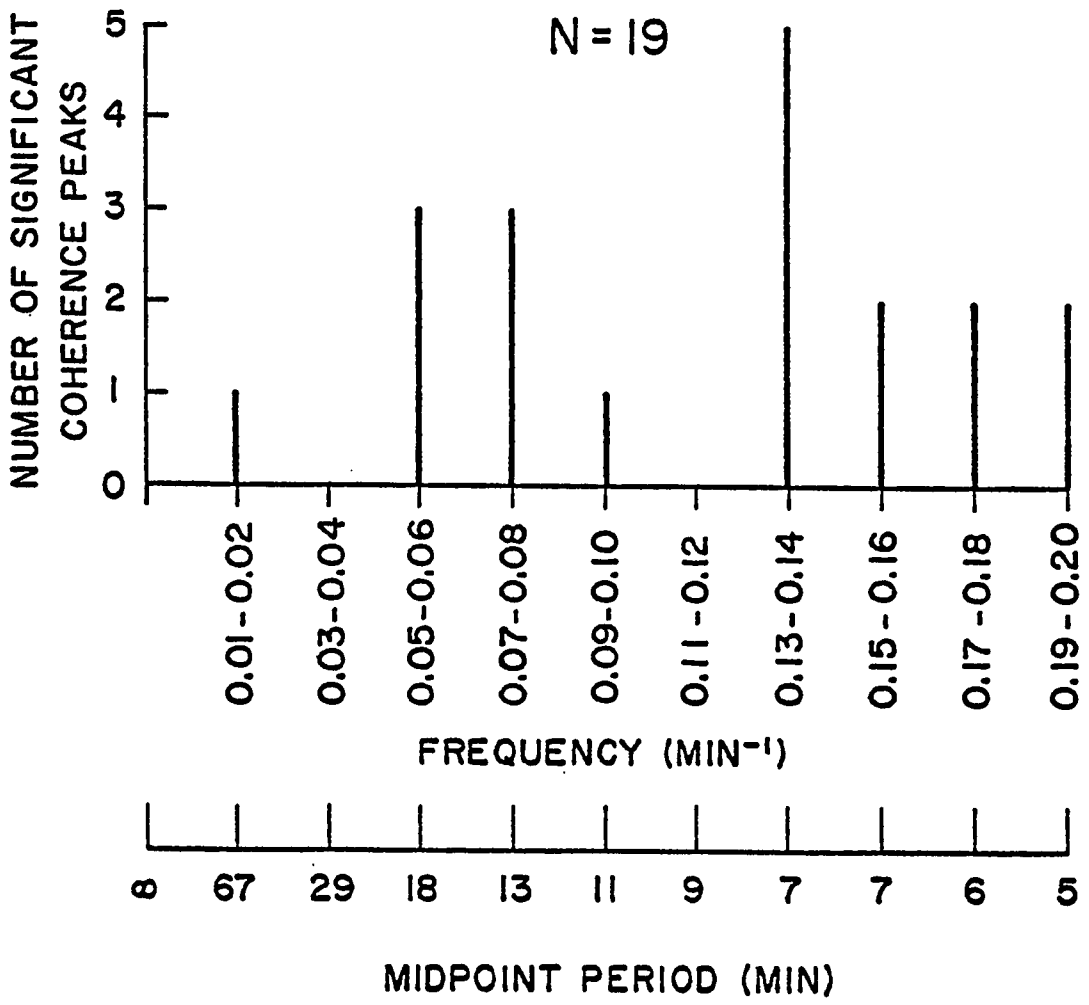

Fig. 20. Histogram plot of 80% statistically significant results from "primary stage" of coherence spectral study involving time series of u^* crossed with v^*, p, and θ_e.

coherence spectra, after ignoring the high frequency mode of activity and applying the constraint $|\Delta\varphi| \leq 60^\circ$. Notice that only five of the ten candidate stations display a significant low frequency peak. These five cases show phases φ_{BP} clustering in the first quadrant with means of $\overline{\varphi}_{BP} = +75^\circ$ ($\pm$ 42°) and $\overline{T} = 16.4$ min ($\pm$ 5.1 min). The mean period agrees within one minute of that obtained from the "preliminary stage" of inquiry, thus confirming the choice of the particular bandpass filter. The mean phase angle differs by only 15° from the 90° predicted from the theory of gravity waves in an environment without vertical wind shear (see (8) and (9)); the addition of shear would alter the u^* vs p phase relationship, but not the u^* vs v^* relationship. Still, the large variability in these results caused by such a small sample does not permit a definitive confirmation of the gaavity wave hypothesis. A closer inspection of the statistical and mesoanalytical data is in order.

The geographical location of the five stations is given in Fig. 22. It is apparent that the wave activity occurred within a distance of at most 20 km from the dryline.

Was the same stochastic physical process being detected by all stations? Although there is some hint of a clustering of those stations that detected coherent wave signals, these cannot reliably be combined into one larger group of stations surrounding the dryline, because there was no record of wind data at VRW, and CHK failed the tests of

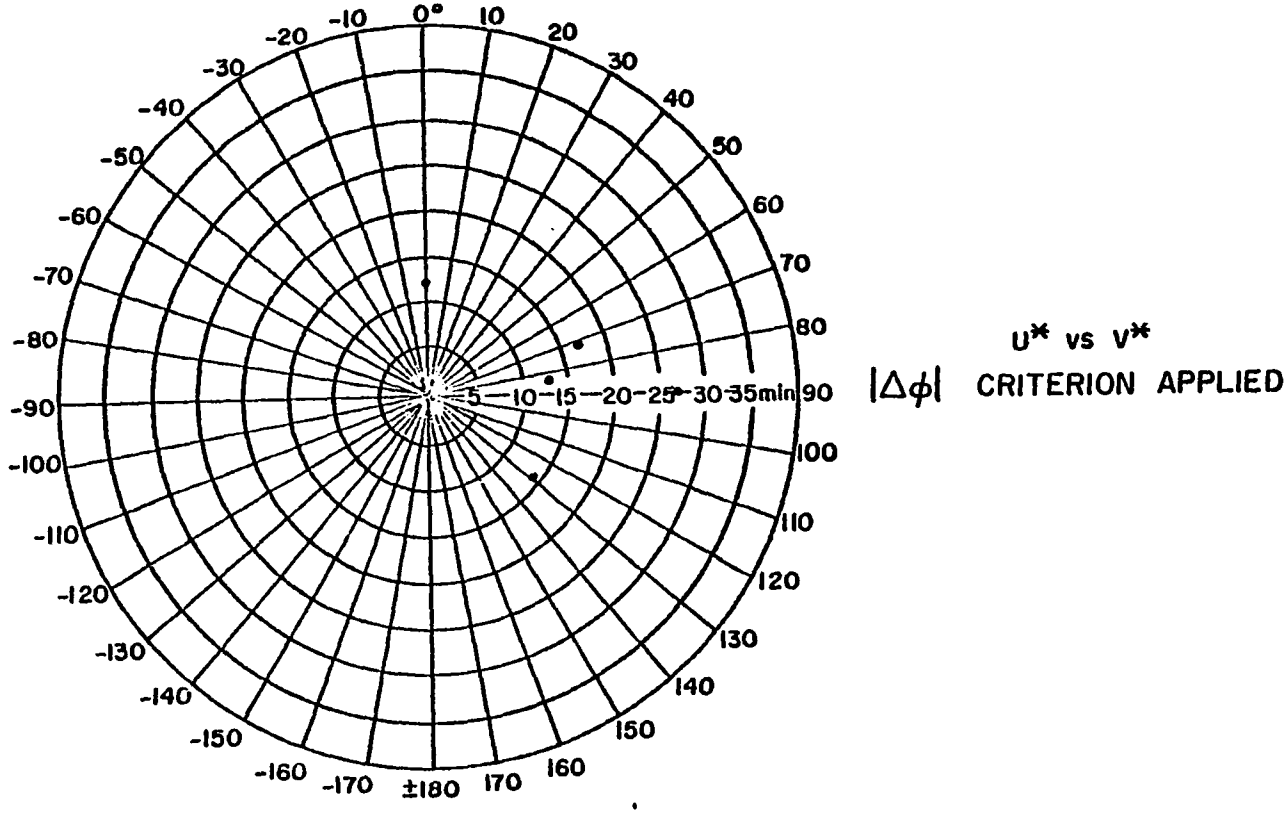

Fig. 21. Relationship between wave period and phase angle for the 80% significant peaks in the u* vs v* coherence spectra. High frequency mode disregarded, and $|\Delta\varphi| \leq 60°$ applied.

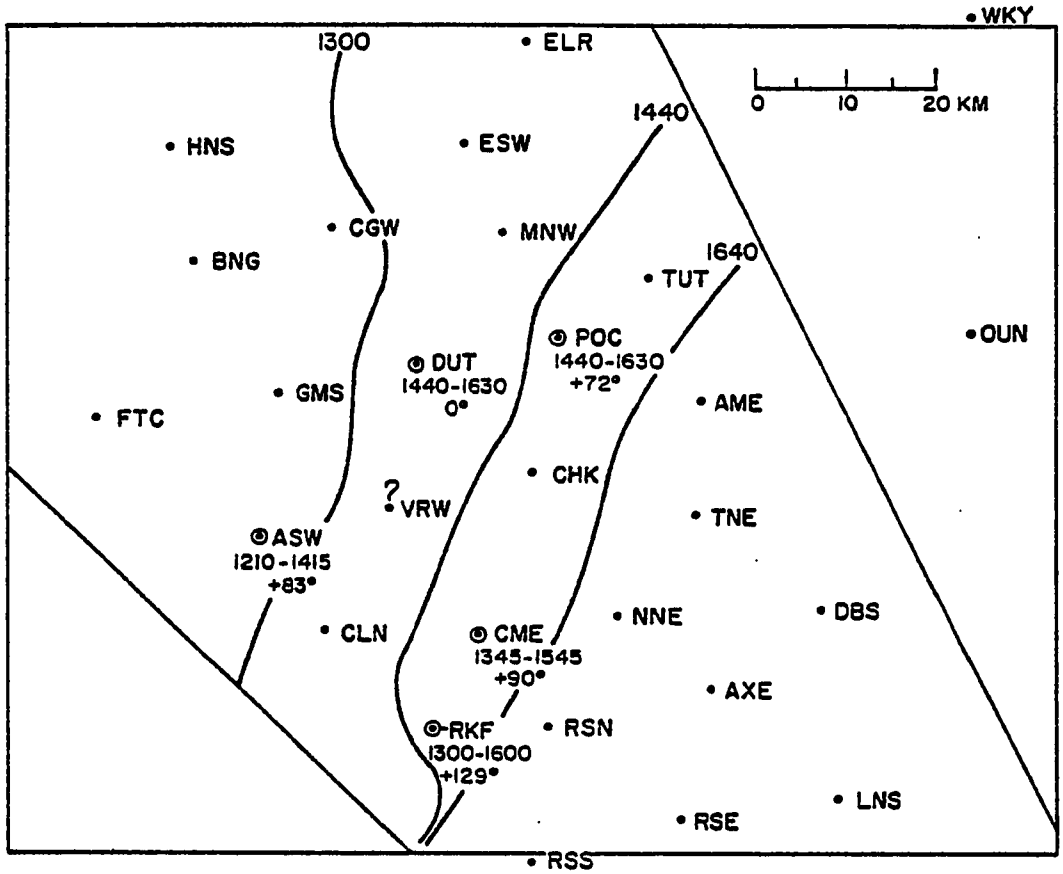

Fig. 22. Display of all mesonet stations that displayed coherent, consistent spectral wind signals. At each of these stations, spectral period of investigation and ϕ_{BP} value are indicated. Also shown are several dryline isochrones and stations WKY, OUN, and FSI discussed later in connection with tower and rawinsonde observations.

linear correlation. However, there is no systematic difference in phase relationship or period between the stations, so there is no reason to think that multiple processes were being sampled.

The geographical display (Fig. 22) suggests that individual waves were spatially incoherent somewhat beyond one horizontal wavelength. To test this idea, cross spectral analyses were performed on the u^* time series between stations DUT, POC, and MNW during interval 1450-1630, and stations RKF, CME, and RSN during interval 1300-1520. Stations MNW and RSN were included because the tests for linear correlation were passed there. The fact that these two stations failed to indicate coherent, consistent signals in the u^* vs v^* cross spectra does not necessarily imply that spatially coherent u^* signals cannot be found since this would be the case if, for instance, the v^* signals were very weak. Unfortunately, no other station geographically close to stations DUT, POC, RKF, and CME also passes the tests of linear correlation. The results of this test confirmed the idea that the waves were incoherent beyond one horizontal wavelength, as only two pairs of the six stations, DUT-MNW and RKF-CME, showed coherent u^* signals.

The limited spatial coherence can be appreciated easily in the bandpass time series of u^* from these stations, as well as the next station downstream of CME, namely NNE (see Fig. 23). It is helpful in the interpretation of this data to re-examine Fig. 9, and label the mesoscale disturbance

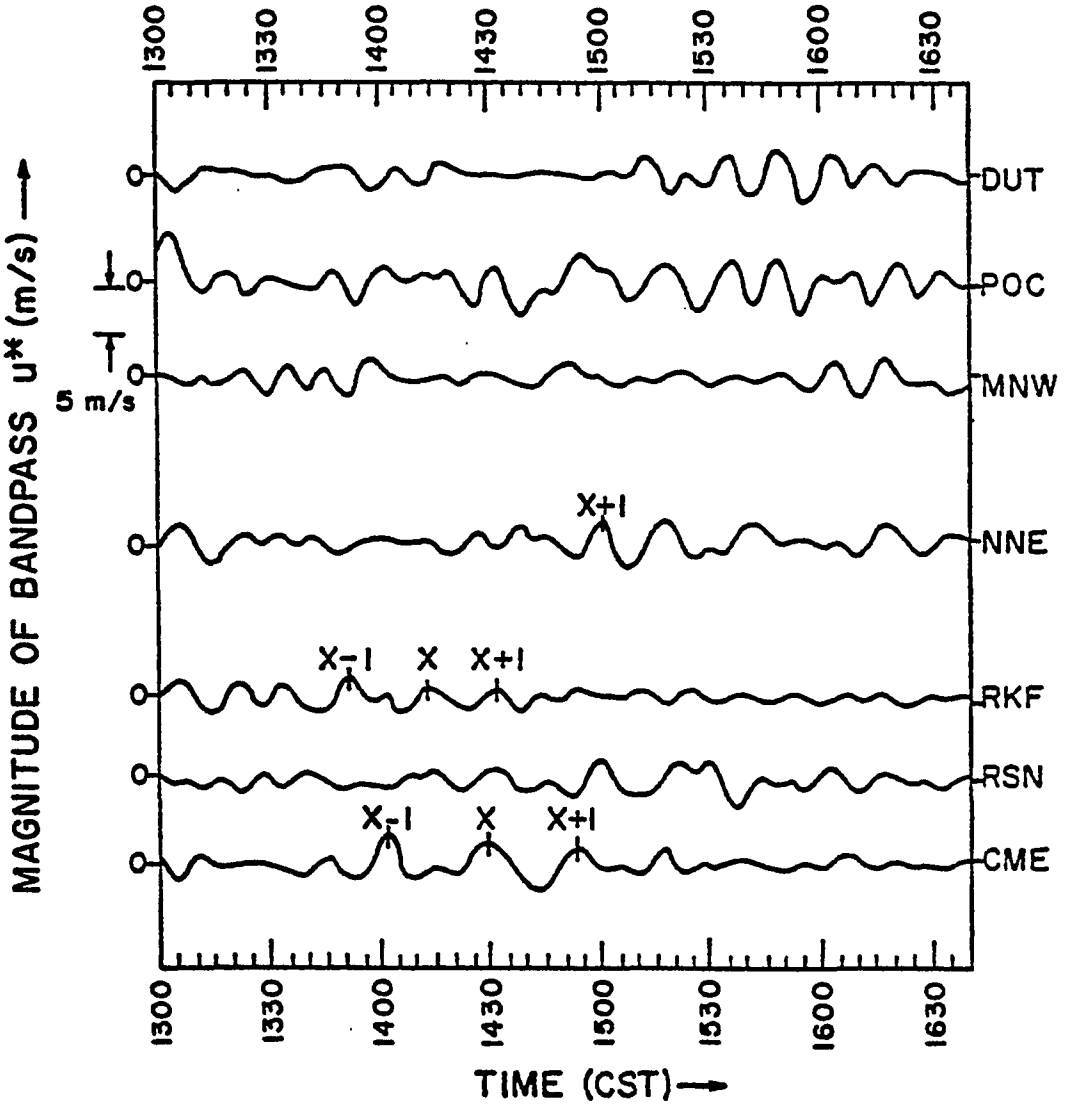

Fig. 23. Bandpass u^* time series of seven stations of interest during periods of wave activity.

depicted there by a very heavy line segment as X, the one preceding it as X-1, and the one following it as X+1. These features are verifiable as positive fluctuations in the bandpass u^* time series at stations RKF and CME, but not at RSN. This observation substantiates the spectral result that the wave signals were confined to a region within 20 km of the dryline.

Only one of the disturbances in Fig. 9 is apparent in the bandpass data taken at NNE, namely X+1 at 1500. Because this station was on the outer fringes of the active wave zone, it only detected some of those disturbances that had by then already triggered deep convection. Not only is such an event not periodic, but such signals are likely contaminated by the convective circulations. Thus it can be understood why the coherence spectra from NNE failed to indicate wave signals, and why the wind data did not pass the tests for linear correlation. It is an important fact that stations RKF and CME are directly upstream of the local area in which each of the first echoes of meso-convective system II appeared (8 km northeast of NNE, as discussed in section III.d.), because this gives credence to the idea that periodic disturbances were responsible for the formation of deep convection downstream.

The geographical intimacy of the other pair of stations that displayed coherent, consistent wave signals (DUT and POC), the spatial coherence of the signals between DUT

and MNW, and the similar u^*-v^* phase relationship, all indicate that the waves in the DUT-POC-MNW cluster are <u>similar in nature</u> to those just discussed. However, it is unlikely that each of the <u>same</u> waves made it that far north, since it is difficult to see these in the bandpass time series, and the vorticity mesoanalyses (Fig. 9) also indicate a weakening or deterioration of waveforms downstream. The strong waves apparent in Fig. 23 during the 1515-1615 interval appear to be confined locally to the northern stations. The problem of determining the spatial coherence of the waves between the two station clusters is compounded by the observation that the CHK wind direction trace showed essentially no variation throughout this period, but instead rather quantum jumps at irregular intervals. Thus, mechanical recording problems is a possibility here.

The lack of strong spatial coherence in the waveform is not inconsistent with the physical structure of the mesoscale dryline environment. Horizontal gravity wave propagation is only possible in a statically stable environment, as can be seen by inserting (20a) into (13), whereupon

$$|c_\omega| = \frac{\omega}{k} = \left(\frac{N^2}{n^2 + k^2}\right)^{\frac{1}{2}} \quad . \tag{43}$$

A gravity wave existing at or west of the dryline would not be expected to propagate horizontally for a very long distance since the stability is so weak there (Fig. 4a). The

vertical propagation of wave energy is examined in the next chapter.

Finally, no estimate of the wave group velocity is possible with this data because the bandpass time series do not show any apparent propagation of a wave packet between stations. Consequently, the dispersive characteristics of the waves, which would be a factor in wave spatial coherence, cannot be determined. No additional examination of $|\underset{\sim}{C}_p|$ seems necessary, because of the success of the "preliminary stage" of analysis with a greater number of stations spaced a greater distance apart.

Only one each of the u^* vs p and u^* vs θ_e coherence spectra displayed a significant peak in the frequency range of interest. The failure of the pressure spectral analyses was anticipated because of instrument limitations. The failure of the θ_e spectral analyses cannot be attributed to instrument limitations, but can be explained in terms of the meteorological conditions present. Remember that horizontal gradients in θ_e outside of the dryline zone are practically non-existent (see Fig. 7). Therefore, the only occasions upon which significant flucuations in θ_e were experienced at a given station when storms were not present were when that station lay within the dryline zone and an MDLW happened to pass by, a circumstance which might have occurred only two or three times. This situation obviously cannot be expected to produce a strong spectral signal, but rather

extreme "red noise" contamination. Remember that this was generally not the case with the velocity fluctuations. This illustrates the general problem of performing a cross spectral analysis of rare event phenomena such as the MDLW.

In summary, the mesoanalytical estimates of wave phase velocity, period, and thus wavelength are verified by the cross spectral analyses. An intrinsic propagation direction of $\theta_w = 305^\circ$ (or 125°) and associated magnitude of $u^* = 6.1$ m/s has been found in five station records that passed severe tests of linear correlation significance needed to justify the use of the impedance concept. None of these stations exist east of the dryline, thus there is indication that the source for gravity waves could not have been within the very low-level inversion present there. The phase relationships between u^* and v^* cluster in the first quadrant with a mean of $\varphi_{BP} = +75^\circ$ ($\pm$ 42°), a value which differs by 15° from the predictions of gravity wave theory. The high amount of variability in the phase estimates can be attributed to the small $V/U \approx v^*/u^*$ ratio (see (14)) and to the limited size of the sample. However, the variability is too great to conclusively confirm the theoretical phase prediction.

Observation that the wave activity was present only within $\pm$ 20 km of the dryline suggests that a careful search for wave critical levels include consideration of the dynamic stability present within the instrumental tower layer,

and that the possibility of wave ducting be studied as well. These considerations may prove helpful in furthering understanding of why the wave signals lacked strong spatial coherence and were confined to such a limited area.

CHAPTER VII

TESTS OF THE GRAVITY WAVE HYPOTHESIS

VII.a. Prediction of Wave Phase Velocity and Use in Reconstruction of Boundary Layer Wind Field

The verification of the mesoanalytical estimates of phase velocity, period, and wavelength by the cross spectral analyses, and the small difference between observed and predicted U-V phase relationships, provides a firm ground for continued investigation of the gravity wave hypothesis as an explanation for the mesoscale disturbance. Evaluation of the other test implications in Chapter V is necessary to assess the ability of the mesoscale dryline environment to produce gravity waves. Although excellent agreement has been found between estimates of phase velocity calculated from the mesonetwork and cross spectral analyses, there is a need to compare these observations with theoretical predictions. No attempt will be made here to perform a complete dynamical stability analysis of the mesoscale environment surrounding the dryline. Such a task will not be performed analytically because no function can easily fit the observed profiles of wind and temperature; rather, a complete numerical

analysis would perhaps need to be performed using a continuous profile model such as that of Mastrantonio, et al. (1976).

The approach here will be to make quasi-theoretical predictions of $\underset{\sim}{C}_p$. Earlier it was shown how both the impedance relation (15) and the Wegener hypothesis (17,18) could independently predict theoretical values for $\underset{\sim}{C}_p$. Unfortunately, the discussion on microbarograph limitations and the result that the u^* vs p spectral analyses failed to find consistent phase relationships raise serious questions about the sole use of the impedance relation for the present purpose. Thus, the comparison of theory to observations will rely upon (1) a comparison of observed $\underset{\sim}{C}_p$ to the Wegener hypothesis prediction, and (2) a comparison of observed $\underset{\sim}{C}_p$ to a composite prediction involving the sum of $\underset{\sim}{\overline{U}}_1$ (the mean wind in the lowest layer of an assumed two-layer model atmosphere) and $\underset{\sim}{C}_\omega$ (the "observed" intrinsic phase velocity found jointly from the impedance relation and Wegener hypothesis prediction).

Both of the methods for predicting $\underset{\sim}{C}_p$ assume a two-layer model atmosphere. How well the real atmosphere can be modelled as such can be seen by examining the subsynoptic rawinsonde data. Since the results of the linear wind correlation study show that no linearly oscillating wind vector can be found east of the dryline, it seems reasonable to consider the wind and temperature profiles from the 1640 Ft. Sill sounding (Fig. 4a), representative of conditions west

of the dryline. The deep adiabatic layer extending to 4.1 km AGL (577 mb), characterized by nearly uniform wind direction, is taken to be the first layer; the 577-543 mb inversion layer is taken to be second layer. The mass-weighted value of $\bar{U}_1$ is calculated to be 219°, 17.9 m/s, and in the upper layer $\bar{U}_2$ is found to be 227°, 34.6 m/s. Thus, with the mesoanalytical observation that $\beta = 219°$, the Wegener hypothesis prediction utilizing (17) and (18) is $|\underset{\sim}{C}_p| = 26.1$ m/s, $\theta_p = 235°$.

The prediction of $\underset{\sim}{C}_p$ from the second method requires an a posteriori estimate of both the direction and magnitude of $\underset{\sim}{C}_w$. Its magnitude is undoubtedly subject to considerable uncertainty because of the poor pressure data for the impedance relation (15). Its direction is also somewhat uncertain, since the linear correlation estimate of $\theta_w = 305°$ differs substantially from that obtainable from the Wegener hypothesis prediction of $\underset{\sim}{C}_p$, namely $\underset{\sim}{C}_w = \underset{\sim}{C}_p - \bar{U}_1 = 264°$, 9.8 m/s. If an average of these two θ_w values (284°) is used in conjunction with the Wegener hypothesis prediction of $|C_w| = 9.8$ m/s, then a predicted value of $\underset{\sim}{C}_p = 241°$, 23.8 m/s is obtained.[4]

The two quasi-theoretical predictions of $\underset{\sim}{C}_p$ differ by 16°, 4.4 m/s and 22°, 2.1 m/s from the mesoanalytical

[4] A third estimate of $\underset{\sim}{C}_w$ can be calculated directly from the impedance relation using pressure data from the instrumented tower, subject to certain energy flux constraints as explained later. However, this estimate (322°, 11.7 m/sec) does not lead to a better comparison with the observed value of $\underset{\sim}{C}_p$.

estimate (219°, 21.7 m/s). The uncertainty in that estimate was 8°, 2.9 m/sec. The most reliable estimate of intrinsic velocity would be the direction obtained from the linear correlation study combined with the magnitude predicted from the Wegener hypothesis (305°, 9.8 m/s).

It will now be shown that it is possible to reconstruct the essence of the observed mesoscale wind field by combining calculations of gravity wave wind components U, $V \approx u^*$, v^*, phase velocities $\underset{\sim}{C}_w$, $\underset{\sim}{C}_p$, and the ambient flow velocity vector $\underset{\sim}{\bar{U}}$. The purpose of this exercise is to justify the prior usage of the surface relative vorticity field to define the wave axes, in light of the fact that gravity waves are essentially irrotational phenomena. Although the energy convergence field along the dryline was also disturbed by the passage of the waves, the vorticity/streamline fields better indicated the waves' presence, because an ambient energy convergence region existing, on the average, at the dryline tended to mask the waves' presence. Of course, at the time when the mesoanalyses were studied in seeking the presence of systematic storm-triggering disturbances, no attempt was made to adapt the method of study so as to "prove" any preconceived hypothesis. Indeed, had mesoscale gravity waves been the subject of biased interest, then surely the convergence field would have been used to define the wave axes. This exercise will demonstrate that the observed propagation characteristics of mesoscale disturbances

detectable as anomalies in the vorticity field can be produced by a peculiar set of circumstances, namely gravity waves whose intrinsic direction of propagation is nearly at right angles to the ambient wind, and whose wind perturbations behave according to (8), (9), and (14).

The Wegener hypothesis prediction of $\underset{\sim}{C}_p = 235°$, 26.1 m/s is used in conjunction with the estimate of $\underset{\sim}{C}_\omega = 305°$, 9.8 m/s to calculate the ambient flow velocity vector $\underset{\sim}{\overline{U}} = \underset{\sim}{C}_p - \underset{\sim}{C}_\omega = 213°$, 24.6 m/s. Use of the observed value of $\underset{\sim}{C}_p = 219°$, 21.7 m/s would give a more southerly direction to $\underset{\sim}{\overline{U}}$ of approximately the same magnitude; however, this minor change has no impact on the final conclusions. Remember that the estimates of $\underset{\sim}{C}_p$ and $\underset{\sim}{C}_\omega$ result from inserting actual observations (from mesonet analysis, rawinsonde analysis, and the linear correlation study of mesonetwork winds) into the gravity wave equations (15), (16), (17), and (18). The three wind vectors are displayed on the left side of Fig. 24.

The direction of $\underset{\sim}{C}_\omega$ determines the direction of gravity wave propagation relative to the ambient wind field, and so the wave-induced wind perturbations U, V are considered within this framework. The cross spectral analyses indicate that the phase relationship between the observed components u^* and v^* does not differ by more than 15° from the theoretical prediction of the U-V phase relationship. Consequently, it is assumed that (8) and (9) provide the actual phase relationship $\varphi = +90°$. The relative magnitudes of

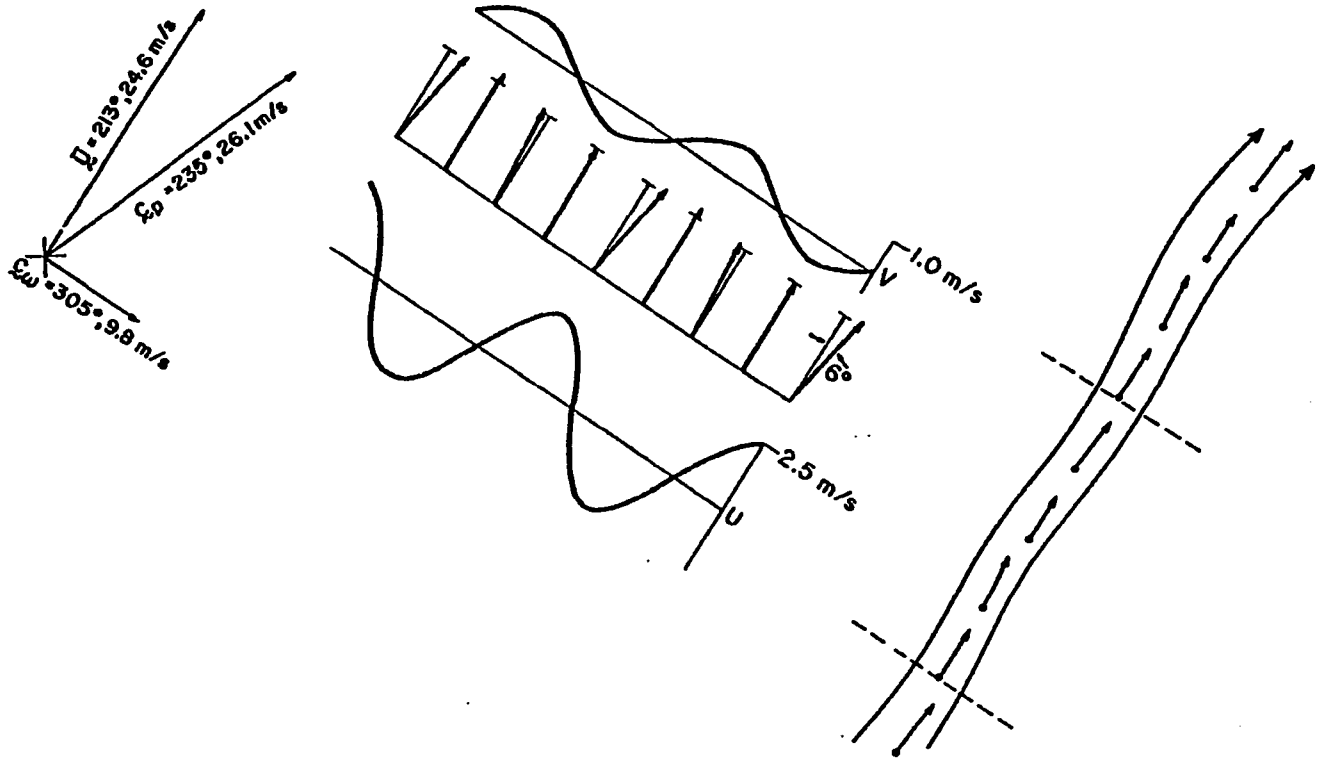

Fig. 24. Reconstruction of mesoscale wind field from observed characteristics of apparent gravity waves and calculated ambient flow velocity vector $\bar{U}$. Left figure shows $\bar{U}$ and gravity wave vectors. Center figure shows wave-induced wind perturbations U, V as estimated from cross spectral and bandpass analyses superposed onto $\bar{U}$ (tic marks depict extent of $\bar{U}$ vector). Right figure shows reconstruction of surface streamlines from center figure, and wave axes (dashed).

$|U|/|V|$ as estimated from the bandpass time series of $|u^*|/|v^*|$ (see Fig. 23) is $\sim$ (2.5 m/s)/(1.0 m/s)=2.5; this observation confirms the theoretical expectation (14) that $|U| > |V|$. The estimated value of $\underset{\sim}{\overline{U}}$ is combined with these results for the magnitude and phasing of U,V in the middle section of Fig. 24 to produce a wind vector that oscillates back and forth with the passage of gravity waves. Notice that this behaviour is consistent both with the observations from those ten mesonet stations that passed tests of linear correlation (Fig. 18 and Table 3), and with the theoretical test implication derived from the impedance relation (Fig. 12).

How well does this reconstructed wind field compare with the observed surface wind field in Fig. 9? The reconstruction method employed here utilizes the ambient wind velocity vector $\underset{\sim}{\overline{U}}$ representative of an entire (boundary) layer. However, the vector is still quite relevant to surface observations because (a) predicted and (surface) observed values of $\underset{\sim}{C}_p$ differ by an amount just in excess of the error bounds on the observed value, and (b) the direction of $\underset{\sim}{\overline{U}}$ does not change significantly throughout the boundary layer west of the dryline. The right side of Fig. 24 displays the reconstructed wind field assuming steady-state conditions and neglecting these minor differences. The similarities are striking:

(1) the directional deviation of the reconstructed wind vector by the waves amounts to 12°, whereas

the mesoanalyses reveal a 10°-30° deviation;

(2) the reconstructed streamlines display a backing-veering-backing behaviour, just as seen in Fig. 9; and

(3) the wave axes clearly are characterized by enhanced cyclonic streamline curvature, with only minor speed variations, which would naturally contribute to wavelike perturbations in the relative vorticity field.

Thus this experiment clearly demonstrates that mesoscale gravity waves whose characteristics are calculated from the actual observations can explain the general nature of the observed surface wind field, and also justifies the use of vorticity anomalies to define the wave axes.

VII.b. Critical Levels

Earlier it was shown that the only plausible source for gravity waves that could be rigorously examined with the available data is dynamic instability. In this section, the two necessary conditions for dynamic instability ($Ri<0.25$ at some critical level) are to be sought for at some altitude in the dryline environment.

The evaluation of $Ri(z)$ is not an easy matter, for its value is extremely sensitive to rather minor fluctuations in the background profiles of wind and potential temperature $\overline{\theta}$, particularly in the case of a deep, nearly

isentropic layer ($\partial\overline{\theta}/\partial z = 0$), such as that existing on the 1640 FSI sounding. Stability theory assumes that (a) the two necessary conditions are evaluated precisely at the time and place of wave occurrence, but that (b) the sounding does not sample any of the waves explicitly, so that the profiles are actually characteristic of the background medium.

These highly idealized conditions are probably never realized in any gravity wave study, however in this study extreme care is taken in the analysis of the sounding data to approach these conditions as closely as possible. The NSSL rawinsondes typically relay information to the ground station at increments of about 50-150 m in height. At each of the data levels, $\overline{\theta}$ and $\overline{U}_c$ are computed, where $\overline{U}_c$ is the ambient wind in the direction of wave propagation (219°),

$$\overline{U}_c = |\underset{\sim}{V}| \cos(\beta-\theta).$$

These data are then interpolated at equal increments in height of 50 m by the method of natural cubic splines (Reinsch, 1967); this method maintains piecewise continuous third derivatives while preserving the exact values at the original data levels. Next, a simple three-point smoother (weights of ¼, ½, ¼) is applied to the interpolated data. Finally, an additional smoothing operation involving an arithmetic average of adjacent sets of five data points is performed, keeping only every fifth point for the actual Ri(z) calculation (hence, a vertical resolution of 250 m results).

The vertical profiles of $\overline{\theta}$ (z) and $\overline{U}_c$(z) prior to the arithmetic smoothing operation for both the 1640 FSI (Ft. Sill) and 1710 OUN (Norman) soundings are displayed in Fig. 25, along with the Ri(z) profiles following arithmetic smoothing. Clearly, this method greatly reduces the number and magnitude of small superadiabatic layers. However, OUN data in the deep layer $2.0 \leq z \leq 2.9$ km MSL is disregarded because of the radiational effects of clouds upon the $\overline{\theta}$ profile (see Fig. 4b). This particular Norman sounding was chosen despite this unfortunate contamination problem because of its intimate spatial and temporal proximity to the dryline and mesoscale waves (see Fig. 22).

From the Ri(z) profile at FSI, we find the two conditions necessary for dynamic instability at a single critical level ($\overline{U}_c = |\underset{\sim}{c}_p|$), namely $z_c = 3.3$ km MSL. Although six critical levels can be found on the OUN profile, only one of these ($z_c = 3.6$ km) occurs in a layer wherein Ri(z) is a rather continuous function. In this layer from $z = 3.50$ km to $z = 3.75$ km, Ri drops from 0.88 to 0.18. By interpolation, Ri = 0.5 at $z_c = 3.6$ km, however this value is sufficiently close to 0.25 considering the degree of variability of Ri with height. Therefore, necessary but insufficient conditions for dynamic instability are met on both sides of the dryline at approximately the same altitude (3.3-3.6 km MSL). Notice that this level exists just beneath the strong inversion found on both soundings.

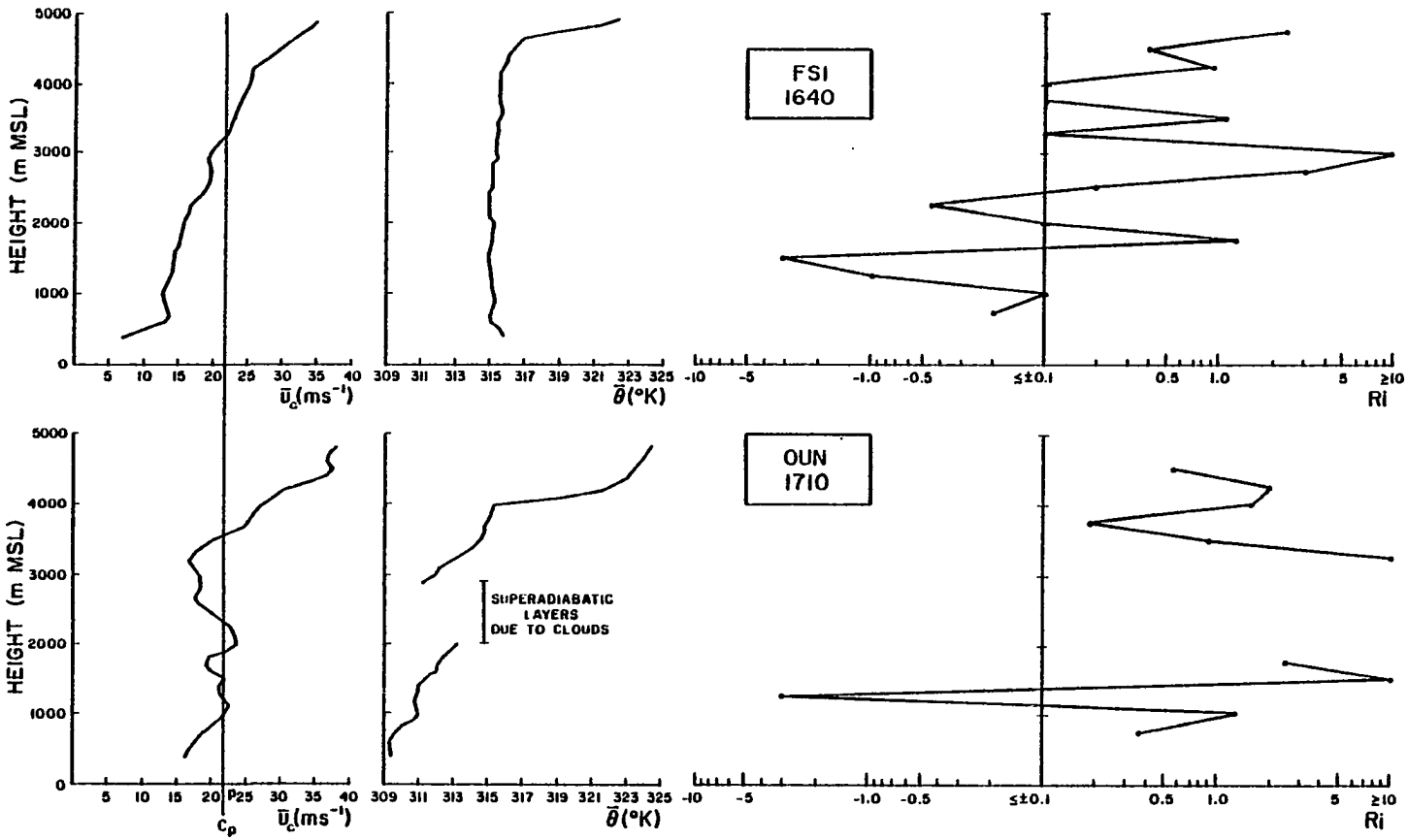

Fig. 25. Vertical profiles of potential temperature ($\bar{\theta}$), wind speed in the plane of wave propagation ($\bar{U}_C$) and Richardson number (Ri). Curves are obtained by spline fitting and smoothing of rawinsonde data from 1640 FSI and 1710 OUN soundings.

VII.c. Waves Detected by Instrumented Tower

The instrumentation on the 444 m high WKY-TV tower and the time-height display were described in Appendix B and Chapter V. A portion of this display appears in Fig. 26 during the interval in which two well-defined mesoscale waves, as well as the dryline, were detected. During this interval, the dryline is, by extrapolation from the mesonetwork, just about at the tower. The closest storms are about 20 km due east of the tower, but are not believed to have any direct influence on this data, since the mesoscale disturbances at the dryline in Fig. 9 do not seem to undergo discernible behavioural changes once storms do develop.

The gradual elimination of a very low-level inversion is evident. The inversion is essentially gone by 1744 when the stability decreases to a value of $\partial\theta/\partial z = 0.5^{\circ}C/450m$. This is only 6 minutes after passage of the dryline[5], as evidenced by the sudden wind veering, decrease of vertical wind shear, and strong updrafts.

The origin of this inversion is in the evaporative cooling that apparently occurred in downdraft air from storm H earlier about 1520. Weak values of incident solar radiation caused by continued cloud cover helped to maintain the strength of this inversion until 1618-1634, during which

[5] Extrapolation of the weak frontal system to WKY would indicate that the system had become coincident with the dryline by this time; in fact, the statically neutral layer seen after 1744 is characteristic of the post-dryline atmosphere.

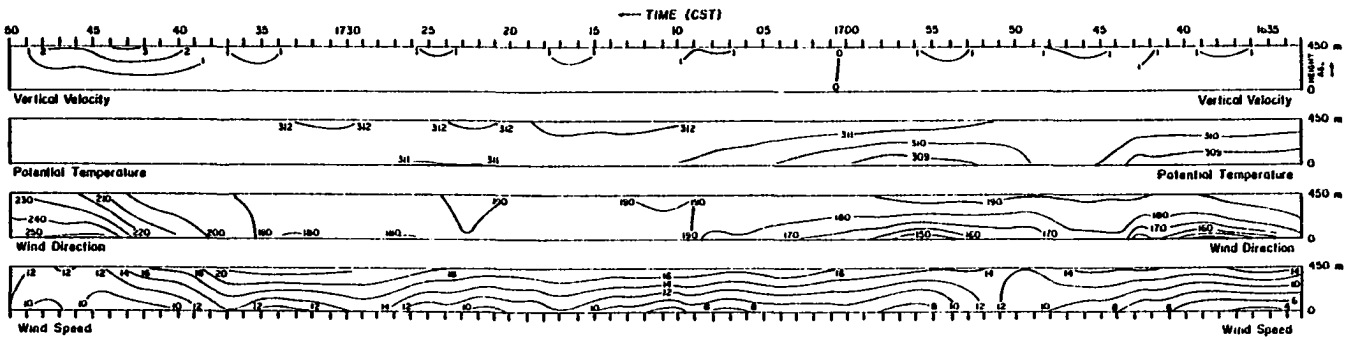

Fig. 26. Time-height display of interpolated and smoothed WKY-TV tower data depicting mesoscale waves. Horizontal and vertical wind speeds are in m s^{-1}, wind direction in deg, and potential temperature in K units.

time a tripling of the radiation values, an increase in the z_1 temperature of 4°C, and a decrease in the static stability to 33% of its previous value, all occurred.

Breaks in the inversion, such as that during 1643-1650, resulted primarily from advection in the lower levels, since neither significant subsidence nor increased incident radiation occurred. It seems as though the dryline was in the immediate vicinity of WKY during the entire interval displayed, and that the periodic advection of warmer air over the station may be interpreted as the passage of several of the MDLW (this does not necessarily contradict an earlier observation made that MDLW activity disappeared over the mesonet after 1600).

Clearly, there is a strong relationship between changes in the fields of static stability and wind velocity. Calculated Ri decreases to values below 0.25 throughout most of the tower layer during those intervals when the static stability is strongest, because at those times both the directional veering and the speed shear are strongest. It is not clear whether increasing static stability permits stronger vertical wind shear, or whether backing of the winds acts to advect in more stable air, however the two fields are definitely interrelated.

The two periods of wind backing in this display are interpreted as evidence for mesoscale waves in the streamline/vorticity fields, which are in turn associated with

the MDLW. This observation provides important evidence for the real existence of these features independent of either the mesonetwork or radar observations.

If the same waves were being detected by both the mesonetwork and tower, then an extrapolation of individual waves from the edge of the network to the tower using the observed propagation velocity of each wave should be capable of predicting when the wave events would occur at the tower. Since the mesoscale axes of enhanced positive vorticity (the waves) were always associated with enhanced cyclonic curvature in the streamlines, then the phenomena to be searched for in the z_1 level tower data are the strongest wind veerings. Altogether seven such waves were extrapolated to the tower, with the results that three of them were not verified because there was either a break in the data or existing storms made interpretation impossible, two others were verified to within four minutes of the expected time of arrival (these are shown in Fig. 26), and the other two failed verification for no obvious reason. The latter two waves were anticipated at the tower at 1714 and 1719, times during which the static stability was very low. Hence, it might be thought that at least some degree of stability was a necessary condition for the occurrence of periodic fluctuations in the velocity field. This idea is in direct contradiction with the cross spectral result that at least one of the mesonet stations (DUT in Fig. 22) detected the waves west of the

dryline where presumably the static stability is neutral. To assist in resolving this paradox, a determination of both the ducting properties of this inversion and the energy/momentum flux profiles is needed.

VII.d. On the Likelihood of Wave Ducting

A preliminary question that needs to be addressed is whether a significant wave amplitude could be expected at the ground if the wave energy propagates downward from the critical level through the adiabatic layer west of the dryline. If a large fraction of the amplitude at the source level is computed to reach ground level, then the paradoxical cross spectral result should be given more weight.

In performing this calculation, it must be shown that the waves are evanescent, which occurs when $N/\omega < 1$. Given the values of $\lambda_x = 22$ km (Table 2) and $|\underset{\sim}{C}_\omega| = 9.8$ m/s (Wegener hypothesis prediction), ω is computed from (13) to be $\omega = 2.80 \times 10^{-3} s^{-1}$. From the $\overline{\theta}$ profile computed from the FSI 1640 data, we see in Fig. 25 that $N \doteq 0$ throughout the entire layer below $z_c = 3.3$ km MSL = 2.9 km AGL, thus the waves west of the dryline must be evanescent.

Despite the fact that wave amplitude is thus expected to decrease exponentially away from the critical level, the "hydrodynamic filtering" property of the atmosphere should allow a significant wave amplitude at the ground because the ratio $\lambda_x/H = 22$ km/2.9 km = 7.6 is so large. Although

the predicted surface pressure perturbation of an evanescent gravity wave can be calculated from (23), we have no knowledge of ζ_H and only a rough estimate of $|\underset{\sim}{C}_\omega|$. Gossard and Hooke (1975) show that for either a two-layer discontinuous density model or a three-layer continuous density profile model (both shearless), the maximum pressure perturbation occurs at the wave source height (P_H). Thus the wave amplitude at the ground (P_o) can be computed as a fraction of P_H using (23) as

$$\frac{P_o}{P_H} = \frac{\rho_s |\underset{\sim}{C}_\omega|^2 \zeta_H \gamma_1 H/[H \sinh(\gamma_1 H)]}{\rho_s |\underset{\sim}{C}_\omega|^2 \zeta_H \gamma_1 H/[H \tanh(\gamma_1 H)]} = \operatorname{sech}(\gamma_1 H), \tag{44}$$

where $\gamma_1 H = 2\pi H/\lambda_x$, from which we obtain $P_o/P_H = 0.73$. Thus a very significant fraction of the wave amplitude can be expected at the ground west of the dryline, which confirms the cross spectral implication that strong low-level static stability is not a necessary condition for ground detection of the waves.

It is now of interest to examine the ducting properties of the low-level inversion seen in the tower data. The argument for strong static stability being a necessary condition for mesoscale wave occurrence is seemingly given additional support by the observation that the vertical extent of the wind direction fluctuations seems to be limited by the height of this stable layer (Fig. 26). This suggests that a duct may exist whose height (h) is smaller than that

of the top of the tower.

This idea is tested by examining the four necessary conditions for ducting listed in Chapter IV. Although this hypothetical duct layer is statically stable, Ri is typically super-critical (Ri < 0.25) throughout much of the layer; thus, the first two conditions of Lindzen and Tung (1976) are met. Disregarding the superadiabatic cloud layer in Fig. 4b, the lapse rate of the atmosphere above the tower is conditionally unstable, and since the conditions for dynamic instability are met, the third criterion of finding a good upper reflective layer is also realized. It is with the last criterion ($h > \lambda_z/4$) that problems exist. Using (24) to compute λ_z, and given that the Väisälä-Brunt frequency in the duct layer averaged during the two wave episodes of 1633-1642 and 1652-1703 is

$$N = \left[\frac{(9.8 \text{ m s}^{-2})}{(310\text{K})} \, (5.8 \text{ K/Km}) \right]^{\frac{1}{2}} = 1.36 \times 10^{-2} \text{s}^{-1},$$

we obtain $\lambda_z/4 = 1133$ m, which is higher than both the tower and the apparent height h.

The inversion cannot act as a duct because it is too shallow. This fact becomes apparent if a comparison is made of the profiles of potential temperature obtained at approximately the same time from the tower and the nearby Norman rawinsonde release (Fig. 27). Notice that $\overline{\theta}$ increases linearly with height at the tower even if the linear interpolation assumption is not imposed. The $\overline{\theta}$ profile at Norman

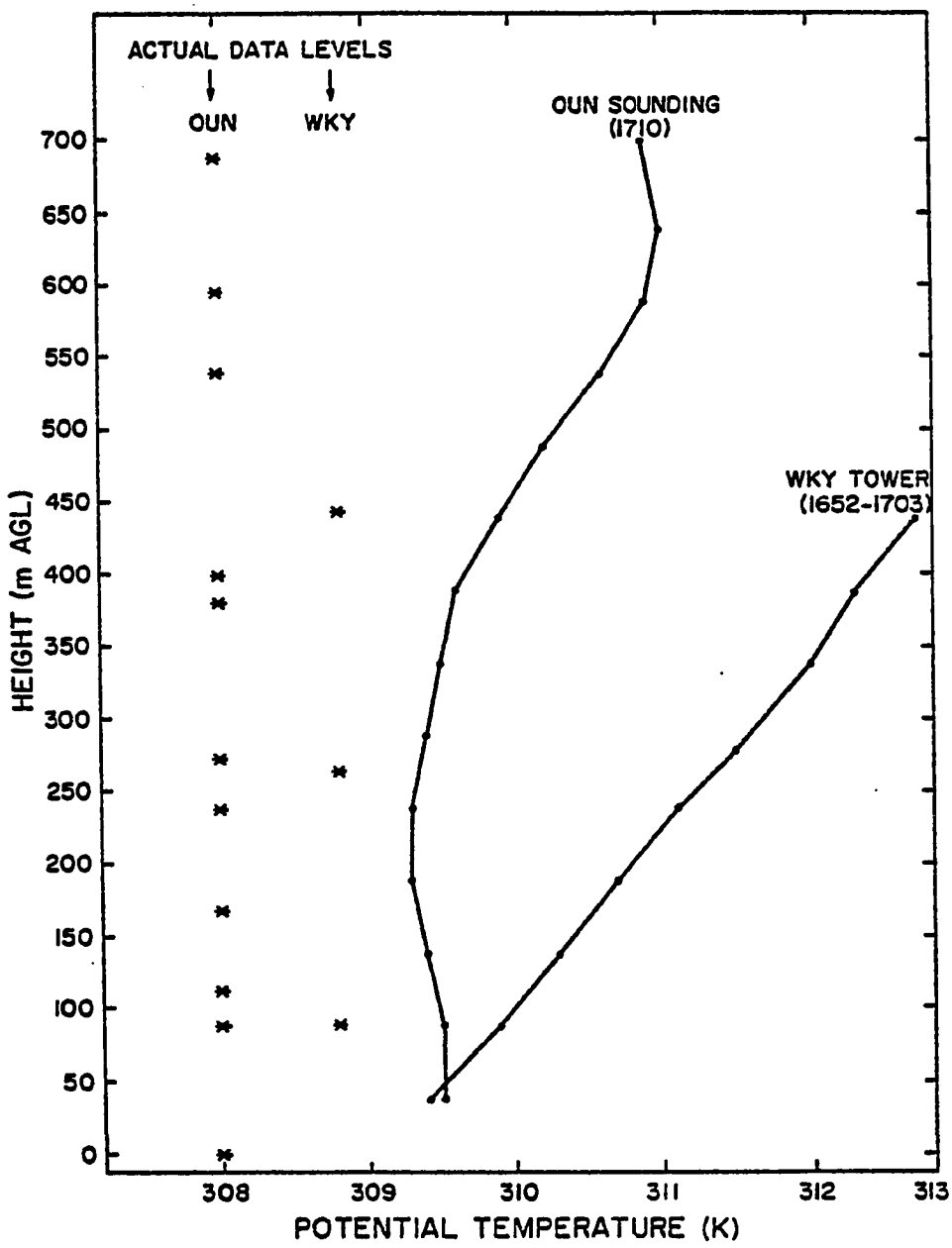

Fig. 27. Comparison of $\overline{\theta}$ profiles calculated from sounding and tower data during intervals shown.

indicates that an inversion exists at 638 m AGL (below $\lambda_z/4$), imbedded within a much deeper atmosphere characterized by somewhat lower static stability (Fig. 25). Because the two values of $\overline{\theta}$ at the ground are in exact agreement, and the strong static stability exists for some unknown distance beyond the top of the tower, the insufficiently deep inversion at Norman is assumed to exist above the tower at approximately the same level (this cannot actually be verified because no soundings were released at WKY). Hence, the low-level inversion cannot act as a duct, and the impression that the wind direction fluctuations are limited vertically to a height h is inconsistent with the physics.

Because the shortest wavemodes are attenuated most easily and the predicted surface wave amplitude is so large without the presence of a duct, there really does not seem to be any need for a duct in any case (bear in mind that the computation of $\lambda_z/4$ is very sensitive to the value of $|\underset{\sim}{C}_g|$ used). The point needs to be emphasized that the fluctuations seen in the tower data are undoubtedly the same waves detected over the mesonetwork. Their source cannot be within the tower layer since $|\underset{\sim}{U}_c| < |\underset{\sim}{C}_p|$ everywhere, but more likely at $z_c = 2.9\text{-}3.2$ km AGL determined from the rawinsonde analysis. The paradox is most easily resolved if static stability is not required as a <u>necessary condition</u> for wave occurrence, but rather if stability is understood to be merely a <u>manifestation</u> of such waves just east of the dryline.

Henceforth, the failure to verify those two waves expected during periods of neutral stability can be thought of as just a coincidence, since those waves were weakening rapidly over the mesonetwork and could have perhaps dissipated before reaching the tower.

It is conceivable that the role played by the low-level inversion may in fact have been a destructive one. Notice that the inversion height h (638 m AGL) is about half of that required for a good duct $\lambda_z/4$ (1133 m AGL). Thus, instead of a constructive interference pattern between the source and reflected waves, a destructive one may have been created. This idea may help to explain why coherent, consistent signals could not be detected by the cross spectrum analyses beyond 20 km east of the dryline. Of course, this remains within the realm of speculation.

VII.e. Wave Energy and Momentum Flux Calculations

Quantitative estimates of energy and momentum flux resulting from shear instability have rarely appeared in the literature, because they require in-situ data obtained by aircraft, free balloon, or tower (Gossard and Hooke, 1975). An example of one such calculation and its implications for finding the level of wave generation from tower data can be found in Merrill (1977). In this thesis, the basic Merrill methodology is used, although occasional gaps in the data do not permit use of such a sophisticated bandpass filter that requires long continuous data records. Instead, the Shuman

filter (section V.a.) is applied to smooth the data, after which the mean fields, calculated over the period 1633-1703 encompassing two wavelengths, are subtracted from the low-pass data to obtain the estimated "wave fluctuations". Examination of the resulting data shows that the remaining fluctuations are indeed mainly in the desired 10-30 minute range.

It has been shown by Elliott (1972) that undesirable dynamic pressure contributions to the measured pressure under conditions of neutral stability are usually 0.001-0.002 times the value of the measured pressure for wind speeds of 5-10 m/s. Because this problem is very significant when determining pressure perturbations of perhaps a few tenths of a millibar magnitude due to gravity waves, all measured pressure data were corrected for this effect by subtracting out the term

$$P_{dyn} = \rho_o(z) |\underset{\sim}{V}|^2/2,$$

which had typical values of 0.5-1.5 mb.

All computations were performed in the plane of intrinsic wave propagation using an iterative technique. Specifically, an initial guess of $\theta_\omega = 305^\circ$ was used at all three levels, the impedance relation (15) was then employed to obtain $|\underset{\sim}{C}_\omega|$, and estimates of momentum and energy flux were made using (25), (28), and (29). The resulting vertical variation of $|\underset{\sim}{C}_\omega|$ was then examined for reasonable continuity; also, the difference between the two energy flux estimates was examined, and if either the continuity or flux difference

was unacceptable, the program was iterated with a new guess for θ_ω until reasonable values were obtained at each level.

The "wave fluctuation" data were inspected prior to the actual flux computations to insure that a high degree of P-U correlation existed at all three instrumented levels. This check was performed to give credence to the idea of performing flux computations on data assumed to be representative of gravity wave activity. During the 1633-1703 interval, P and U fluctuations were in-phase 78% of the time at the z_1 level, 61% of the time at the z_2 level, and 99% of the time at the z_3 level.

The results of these calculations are summarized in Table 4. The value of $|\underset{\sim}{C}_\omega|$ at level z_2 still seems questionable, and in fact both estimates of energy flux there were extremely sensitive to very modest changes in θ_ω. Undoubtedly this failure is due to the fact that no real pressure data was collected at this level and that the linear interpolation estimate of the pressure made in order to utilize (28) and (29) was a poor one. In fact, the degree of P-U correlation was lowest at that level. Therefore, it is virtually impossible to obtain reasonable profiles of energy flux with this data set, and the search for the source of the waves must rely totally upon the momentum flux profile. Nevertheless, it is somewhat comforting to find that at each level the sign of the momentum and energy fluxes are the same, just as is required when everywhere $|\underset{\sim}{C}_p| > |\underset{\sim}{U}_c|$.

The profile of wave momentum flux indicates divergence at or near $z_2 = 266$ m. This general profile is very insensitive to the actual value of θ_ω used because this parameter only affects the magnitude of U in a very weak manner. However, the value of momentum flux at z_3 is somewhat questionable, because (a) three fluctuations in W were evident while only two existed in U, and (b) as seen from (26), flux divergence at a critical level where $Ri < 0.25$

Table 4. Wave Momentum and Energy Flux Calculations

Level	θ_ω (deg)	$\lvert \underset{\sim}{C}_\omega \rvert$ (m s^{-1})	$F_M(25)$ (dyne cm^{-2})	$F_E(28)$	$F_E(29)$ (erg $cm^{-2}s^{-1}$)
z_1	322	11.7	-0.42	-578	-489
z_2	304	4.4	-0.85	-223	-371
z_3	360	15.3	+1.42	+2080	+2170

implies a source level for wave generation, yet there is no critical level in this data. For these two reasons, the flux estimate at z_3 is disregarded, in which case the most negative value of the flux exists at or above z_2. This is interpreted as a downward flux of U-momentum from above z_2, given that $C_\omega > 0$. The greatest value of $F_M = -0.85$ dyne cm^{-2} is a rather small flux, but similar to the -1.5 dyne cm^{-2} reported by Merrill (1977) for an event with a critical level at 130 m AGL. These results are not in contradiction

with the observation that a critical level exists much higher, but do not support the contention that the low-level inversion could have acted either as the wave source or a duct (in which case zero momentum flux is anticipated). Therefore, the earlier observation of the critical level in the 2.9-3.2 km layer is accepted as the most likely source level for gravity waves. All of these results are synthesized and evaluated in the forthcoming chapter.

VII.f. Aspect Ratio

Another crucial test suggested earlier to determine the relative acceptability of the thermal plume vs. the gravity wave hypotheses is the degree of hydrostaticity of the mesoscale disturbance as parameterized by its calculated aspect ratio A. Two calculations of A can be made, the first from gravity wave theory using (20a), which gives

$$A = \frac{\lambda_x}{\lambda_x} = \frac{n}{k} = \left[\left(\frac{N}{\omega}\right)^2 - 1\right]^{\frac{1}{2}}$$

$$= \left[\left(\frac{1.36 \times 10^{-2}\ s^{-1}}{2.80 \times 10^{-3}\ s^{-1}}\right)^2 - 1\right]^{\frac{1}{2}} = 5,$$

thus implying an essentially hydrostatic phenomenon, if the disturbance is actually a gravity wave. The second calculation is made independently of any gravity wave considerations, and involves the slope of the line connecting the maxima in U at each of the three tower levels during the

periods 1638-1643 and 1651-1659. Since the disturbances appear first at the uppermost levels,

$$A = \frac{\Delta x}{\Delta z} = |\underset{\sim}{c}_p| \frac{\Delta t}{\Delta z} = (21.7 \text{ m s}^{-1}) \ (1.099 \text{ s m}^{-1}) = 24.$$

Despite the large difference between the two estimates, the conclusion is still that the phenomenon is basically hydrostatic in nature.

CHAPTER VIII

ABILITY OF MESOSCALE GRAVITY WAVES TO INITIATE DEEP CONVECTION

VIII.a. Observation Synthesis and Theory Evaluation

Considerations from classical hydrodynamic stability theory outlined only two general hypotheses that are both testable and relevant to the mesoscale distrubance phenomenon-the theory of thermal plumes, and the theory of gravity waves. The vortex stretching hypothesis, although intractable and questionably relevant, yet is still plausible, and seems to have some merit in the fact that coherent, consistent spectral signals were found only within $\pm$ 20 km of the dryline zone, which also served as a local extremum in the relative vorticity field. Unfortunately, this hypothesis cannot be thoroughly tested until the theory is in a more advanced state. The remaining hypotheses can now be evaluated as explanations for the occurrence of the mesoscale disturbances and associated dryline waves. Computations from the mesoanalyses and cross spectral analyses, and comparison of other observations with the test implications from gravity wave theory, are synthesized in performing this

evaluation.

The thermal plume concept is now seen to be implausible for several reasons:

(1) Mesoanalyses of relative vorticity and energy convergence indicate the existence of the storm-causing mesoscale disturbance in some instances at least 50 minutes (average of 35 minutes) prior to first echo appearance. This period of time exceeds a realistic prediction of the time it should take a rapidly growing cumulus cloud to not only produce radar-detectable hydrometeors, but also significantly influence the surface fields. Surface detection of plume-associated perturbations should be possible only when the plume circulations are sufficiently intense, or deep. Thus, the thermal plume concept cannot explain such an early appearance of the surface perturbations.

(2) The mesoscale disturbances are apparently wavelike, displaying unequal wavenumbers along and normal to its direction of propagation. Often two separate areas of ambient convergence would be

simultaneously enhanced by the passage of a mesoscale disturbance propagating transverse to the mean wind direction. There is no reason to suspect that a line of plumes would be oriented as such, since theoretical models (Asai, 1970) predict a preferred longitudinal mode under the given atmospheric conditions. The wavelike nature of the disturbance is clearly evident on the space-time cross section in Fig. 11.

(3) Despite the result that the cross spectral analyses indicate coherent, consistent wave signals west of the dryline where $Ri < 0$, the disturbances in Fig. 11 propagate across the dryline and as far as 20 km east of the dryline without a noticeable change in trace speed. Tower observations of strong fluctuations in the low-level static stability just to the east of the dryline indicate the passage of several of these disturbances. The degree of stability prior to each event is so strong that it would be very difficult for any thermal plume to exist unless

air were mechanically forced upwards; of course, a gravity wave could conceivably be such a mechanism.

(4) The disturbances are essentially hydrostatic phenomena characterized by an aspect ratio at least five times as large as that typical for a thermal plume.

One of the most crucial tests of the two hypotheses, the P vs. U phase relationship, could not be performed because of microbarograph limitations. Despite this problem, upon considering all of the results just discussed, there is little doubt that the thermal plume hypothesis is not an acceptable one. Perhaps the best reason for disregarding the thermal plume mechanism is the much stronger evidence that exists in support of the gravity wave mechanism:

(1) The wind vectors at ten of the mesonet stations oscillate back and forth in a statistically linear fashion, just as predicated by the impedance relation shown schematically in Fig. 12. Half of these stations display coherent, consistent peaks in the u^* vs v^* coherence spectra. None of these stations exists east of the dryline.

(2) Those five mesonet stations which pass

the $|\Delta\varphi|$ phase difference criterion display an average u^* vs v^* phase angle of $+75^\circ$, as compared to the $+90^\circ$ predicted from the theory of gravity waves in a shearless environment.

(3) Estimates of horizontal phase speeds calculated from the mesoanalyses, the space-time cross section, and the cross spectral phase angles agree within 2% of one another. The difference between the mesoanalytical estimate of $\underset{\sim}{C}_p$ (219°, 21.7 m/s) and the two predictions of $\underset{\sim}{C}_p$ from gravity wave theory lies just outside the uncertainty in the mesoanalytical value (8°, 2.9 m/s). The mean period of coherent, consistent spectral signals in the u^* vs v^* time series (15-16 minutes) compares quite favorably with the mean period of mesoscale disturbances (17 minutes). Therefore, the wave characteristics of the mesoscale disturbance are successfully analyzed in terms of gravity wave parameters $u^*, v^* \approx U, V$.

(4) By combining the calculated gravity wave phase velocities $\underset{\sim}{C}_w$ and $\underset{\sim}{C}_p$ with

the $|\Delta\varphi|$ phase difference criterion display an average u^* vs v^* phase angle of $+75^\circ$, as compared to the $+90^\circ$ predicted from the theory of gravity waves in a shearless environment.

(3) Estimates of horizontal phase speeds calculated from the mesoanalyses, the space-time cross section, and the cross spectral phase angles agree within 2% of one another. The difference between the mesoanalytical estimate of $\underset{\sim}{C}_p$ (219°, 21.7 m/s) and the two predictions of $\underset{\sim}{C}_p$ from gravity wave theory lies just outside the uncertainty in the mesoanalytical value (8°, 2.9 m/s). The mean period of coherent, consistent spectral signals in the u^* vs v^* time series (15-16 minutes) compares quite favorably with the mean period of mesoscale disturbances (17 minutes). Therefore, the wave characteristics of the mesoscale disturbance are successfully analyzed in terms of gravity wave parameters $u^*, v^* \approx U, V$.

(4) By combining the calculated gravity wave phase velocities $\underset{\sim}{C}_w$ and $\underset{\sim}{C}_p$ with

the phase relationship between, and magnitude of, the wave wind components u^*, v^*, the essence of the observed mesoscale wind field can be reconstructed. This exercise not only justifies use of the surface relative vorticity field to define the gravity wave axes, but it demonstrates that gravity waves whose characteristics are calculated from observations can explain the general nature of the observed wind field.

(5) Because the (observed) wavelength-to-(predicted) source height ratio is so large, gravity wave theory predicts that 73% of the maximum wave amplitude aloft could be expected to reach ground level west of the dryline. Thus, ducting is not a necessary condition for a significant wave amplitude to exist at ground level. The fact that both the space-time cross section and the linear correlation-cross spectrum analyses show periodic signals west of the dryline is consequently in accordance with predictions from evanescent gravity wave theory.

(6) Examination of the necessary ducting conditions of Lindzen and Tung (1976) indicates that not only is the low-level inversion to the east of the dryline too shallow to act as a good duct, but that its presence may have acted to cause destructive wave interference. Such an hypothesis can explain the observed lack of wave activity beyond 20 km east of the dryline.

(7) Cross spectrum and bandpass analysis indicates a lack of spatial coherence in the waveforms beyond one or two horizontal wavelengths. The observed deterioration of the vorticity disturbance identity downstream (Fig. 9) is supported by these analyses. Moreover, the physical structure of the mesoscale environment at and west of the dryline theoretically could not be expected to allow significant horizontal propagation of gravity waves.

(8) The only relevant and testable source for gravity waves, namely dynamic instability, apparently exists on both sides of the dryline at approximately

the same altitude (2.9-3.2 km AGL), since the two necessary conditions for dynamic instability are found there. The wave momentum flux profile determined from the tower data also implies that a wave source is somewhere above the low-level inversion.

In conclusion, the gravity wave mechanism seemingly offers the best explanation for the occurrence of the wave-like mesoscale disturbances since the test implications of the theory best fit the available, relevant empirical findings. Perhaps the most crucial question to be answered now is: Can the ability of the evanescent gravity waves to initiate severe convection be demonstrated quantitatively?

VIII.b. The Destabilizing Effects of the Gravity Waves

There is a straightforward procedure to study the ability of the evanescent gravity waves to initiate deep convection. The first step in the procedure is to obtain the vertical profile of parcel displacement $\eta(z)$. This profile will not be determined by any specific analytical or numerical model, and thus is not constructed under any simplifying assumptions other than that the gravity wave is evanescent, not ducted, and is not affected by the presence of any critical level (see below). A representative sounding of the mesoscale dryline environment must be created

before application of this $\eta(z)$ profile. Finally, the layer lifting method (employed by Uccellini (1975)) is used to study the destabilizing effect of the waves during passage of the wave crests over the dryline, given the vertical displacement profile $\eta(z)$, and thus to determine their ability to initiate deep convection.

The maximum parcel displacement ζ_H must be calculated before constructing the vertical profile of $\eta(z)$. Although (23) implies that a scaling factor involving P_o is needed, substitution of the impedance relation (15) for P_o results in

$$\zeta_H = \frac{U}{|\underset{\sim}{c}_\omega|} \frac{\sinh \gamma_1 H}{\gamma_1} , \tag{45}$$

for which $U = 6.1$ m/s, $|\underset{\sim}{c}_\omega| = 9.8$ m/s, and $\gamma_1 H = 2\pi H/\lambda_x$, or thus $\zeta_H = 2.1$ km. This value for ζ_H is about 2.5 times larger than one calculated by Uccellini (1975) with the aid of a simple linearized two-layer model. However, our ζ_H is only a factor of 1.2 times that reported by Reed and Hardy (1972) for a case similar to ours involving gravity waves whose wavelengths were 15 km and probable source region at 10 km AGL.

Before continuing with the procedure, a few comments should be made on the possible sources of error contributing to the relatively large estimate of ζ_H. The most obvious problem concerns the guess made earlier on $|\underset{\sim}{c}_\omega|$, which

ultimately is related to the microbarograph limitations. Another problem is the inherent assumption in (23) that no critical levels exist, whereas in reality one is found in the deep adiabatic layer occupied by the gravity wave. Gossard and Hooke (1975) show that

$$W(z) \sim (z-z_c)^{\frac{1}{2}}$$

and

$$U(z) \sim (z-z_c)^{-\frac{1}{2}}$$

near the critical level. Thus, vertical motion approaches zero at an infinitesimal distance away from the critical point; however, it is also evident that $U \to \infty$ there, so that Kelvin-Helmholtz instability should develop as the consequence of this wave-induced shear to reduce the unstable velocity shear. This nonlinear problem has been treated numerically by Tanaka (1975), who finds that gravity wave energy is redistributed and dissipated by the induced Reynolds stress. Eventually the wavelength would be so small that atmospheric viscosity and thermal conductivity effects would dissipate the wave energy at molecular levels, thus preventing $U \to \infty$. Although the exact effect of the critical level in the $W(z)$, hence the $\eta(z)$, profile is very complex, it must be recognized that it is a potential problem. Quantitative estimates of the errors related to either the microbarograph limitations or the critical level assumption cannot be made,

unfortunately.

The vertical profile of $\eta(z)$ is determined by applying the estimate of ζ_H to (22), and then adopting the inverse of the transformation (6) to $\zeta(z)$. The profiles of $\rho_o(z)$, $\zeta(z)$, and $\eta(z)$ are calculated at 250 m increments (Table 5).

Table 5. Calculated Profile of Wave Vertical Displacement (H = 2.9 km, ζ_H = 2.1 km)

z(km)	0.00	0.25	0.50	0.75	1.00	1.25	1.50	1.75	2.00	2.25	2.50	2.75
ζ(km)	0.00	0.16	0.32	0.48	0.64	0.81	0.99	1.16	1.35	1.55	1.75	1.97
ρ_o(kg m^{-3})	1.08	1.05	1.03	1.01	0.99	0.97	0.95	0.93	0.91	0.89	0.87	0.85
η(km)	0.00	0.16	0.33	0.50	0.67	0.86	1.06	1.25	1.47	1.71	1.95	2.22

The profile of wave displacements is to be applied to the representative dryline sounding shown in Fig. 28. This model is created by taking an average of the potential temperature and mixing ratio values at each level of the 1640 FSI and 1710 OUN soundings. The method removes all superadiabatic layers and produces a double inversion at 600 mb and 550 mb. The resulting surface potential temperature value of 311.5 K agrees exactly with those values found in the surface mesoanalyses along and just to the east of the dryline (Fig. 8). However, the observed mixing ratio of 17-19 g kg^{-1} is underestimated by about 4 g kg^{-1}.

Upon application of the layer lifting method to the sounding, a two-fold destabilizing effect of the gravity

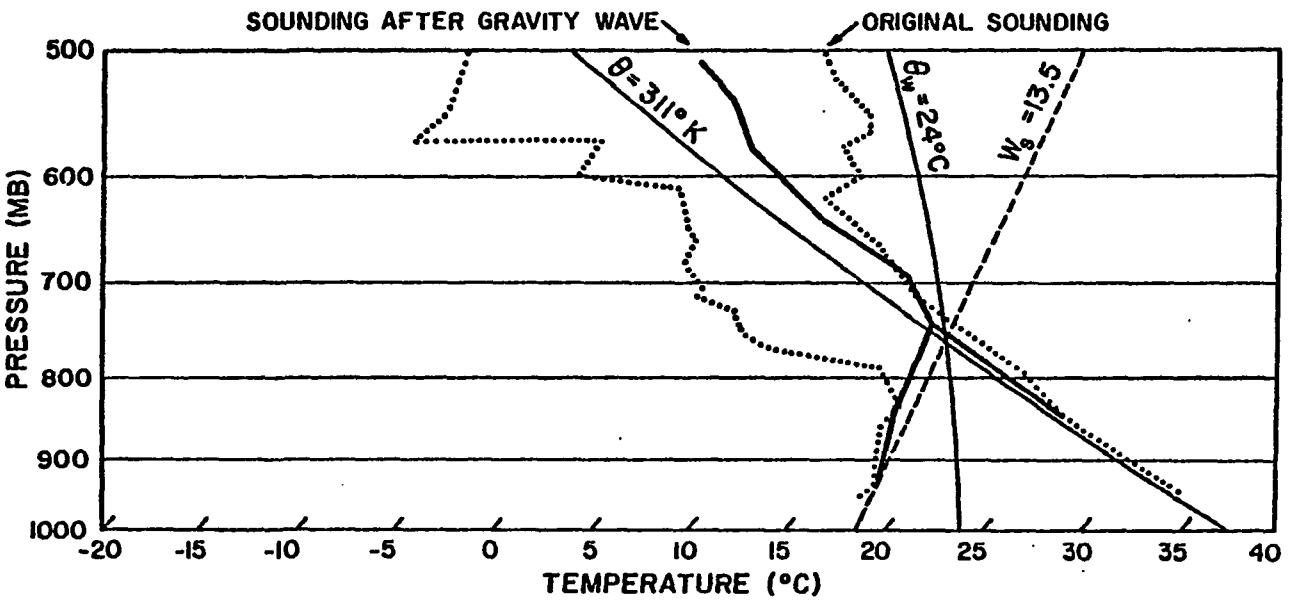

Fig. 28. Representative dryline sounding prior to and during passage of gravity wave crest. Dotted lines depict temperature and dewpoint temperature profiles prior to wave, heavy dark lines depict the same during wave passage.

waves is seen. The original model sounding was both conditionally and potentially unstable, yet this instability could not be realized both because of the weak stable layer just below the LCL at 740 mb and the double inversions aloft that might have suppressed any convection mechanically forced to the LCL. Assuming an average mixing ratio of 13.5 g kg^{-1} (slight allowance has been made for the model underestimate), this potential instability can now be realized during the passage of a gravity wave crest, i.e. following one complete cycle of upward parcel displacement. The first effect of wave passage is the destruction of the strong inversions and the increase in the area of positive buoyancy in the 840-720 mb layer. Parcels may now gain kinetic energy from their environment in their totally unimpeded, accelerated rise from the surface layer.

The second effect is the creation of a deep saturated layer above the 740 mb level, which is nearly coincident with the level of free convection. Thus, deep convection may be expected to develop explosively along the $\theta_w = 24^\circ C$ pseudoadiabatic from cloud bases at the 750 mb LFC. Notice that, although the calculated vertical displacements are undoubtedly too large, the sounding prior to the gravity wave occurrence does not require very much layer lifting to realize the vast reservoir of potential instability present. Since even a reduction in ζ_H by half would allow this instability to be realized, this experiment indicates that these gravity waves

are quite sufficient to initiate deep convection along the dryline.

CHAPTER IX

CONCLUSIONS

In this thesis, an intensive study has been made of a mesoscale "trigger mechanism" responsible for initiating severe convection cells in a major tornado outbreak case involving an Oklahoma dryline (8 June 1974). The mechanism has been isolated as wavelike disturbances, related to the evolving background medium, and shown to be capable of initiating the convection. An important link between the subsynoptic and mesoscale in this case was also revealed, namely that the subsynoptic moisture convergence region along the dryline was maintained by the repeated succession of convergence anomalies associated with the mesoscale wavelike disturbances.

Objective analysis of surface mesonetwork data detected the disturbances as periodic fluctuations in the energy convergence field located generally along the dryline. The propagating waves were also apparent as positive enhancements in the relative vorticity field, and occasionally as disturbances in the moist static energy field that defined the dryline's location. The waves propagated in the direction of

the mean winds in the deep adiabatic layer west of the dryline, with a horizontal phase speed of 22 m/s, a median wavelength of 22 km, and a mean periodicity of 17 min. A cross spectral analysis of the mesonetwork data verified these estimates to within 8%.

A review of classical hydrodynamic instability theory suggested that only two general hypotheses were both testable and relevant to the mesoanalytical findings-the theory of thermal plumes, and the theory of gravity waves. A third concept involving the vertical stretching of vortex tubes along the dryline seemed plausible, but was unfortunately untestable with available data and also questionably relevant to the mesoscale. The wavelike nature of each disturbance, its existence long before the subsequent appearance of the radar echo, its appearance during periods of strong low-level static stability just east of the dryline, and its large aspect ratio, are observations that are in disagreement with the test implications from thermal plume theory. Therefore, this hypothesis was considered an untenable one.

It was found that gravity wave theory could explain the nature of the mesoscale disturbance better than the other hypotheses considered, for the following nine reasons:

(1) Winds at 10 of the 26 mesonet stations oscillated back and forth in a statistically linear manner characteristic of gravity waves (Gossard and Munk, 1954).

(2) Half of these ten stations displayed significant peaks in the coherence spectra involving the time series of the wind components along (U) and normal to (V) the calculated direction of intrinsic gravity wave motion.

(3) All of the five peaks passed strict consistency tests for phase angle, and the mean phase of $+75^{\circ}$ compared quite well with the $+90^{\circ}$ predicted from the theory of evanescent gravity waves.

(4) The difference between the observed and predicted wave phase velocities only slightly exceeded the observational error.

(5) The general nature of the observed mesoscale surface wind field could be reconstructed by combining calculated gravity wave phase velocities with the characteristics of the U,V wind perturbations; moreover, the use of the relative vorticity field in wave detection was thereby justified.

(6) Observations of the waves at ground level was given theoretical support because of the calculation that 73% of

the maximum wave amplitude at the height of wave generation could be expected to reach ground level; this was possible because of the large wavelength-to-source height ratio, despite the evanescent nature of the assumed gravity wave.

(7) The lack of a detectable wave signal beyond 20 km east of the dryline could be explained in terms of gravity wave concepts by considering the ducting properties of a low-level inversion present there.

(8) Sounding data indicated that the two necessary conditions for dynamic instability (Miles, 1961) were present on both sides of the dryline in the 2.9-3.2 km AGL layer. Thus, there was a tenable source mechanism present for gravity wave development, although several other mechanisms could not be ruled out. Observations of wave behaviour and calculated momentum flux also supported the contention of an elevated wave source.

(9) A quantitative analysis of the impact of these evanescent gravity waves upon a

composite sounding representative of the mesoscale dryline environment did indeed show that the wave amplitude in the lower troposphere was sufficient to destabilize the sounding to the point where surface-based parcels could reach their level of free convection without obstruction, and thence deep convection would develop in an explosive manner following the passage of a wave.

This study conclusively demonstrates the capability of a mesoscale gravity wave as a "trigger mechanism" to periodically force the development of one tornadic storm after another. A quantitative comparison of the mesoscale observations with theory has thus attempted to increase our understanding of which processes might trigger the formation of individual severe storms along this, and perhaps similarly acting, drylines. Additional studies must be conducted to ascertain the generality of these conclusions to other drylines, and the peculiarity of the circumstances which permitted the explosive release of potential energy here. It is of fundamental importance that gravity waves apparently triggered the tornadic storms, rather than having merely modulated the intensity of storms generated by other means.

The present study suffers from several drawbacks that

could be remedied in the future with a well-coordinated observational program. The most serious problems result from the lack of reliable, informative microbarograph data, namely (a) a direct computation of intrinsic phase speed with the impedance relation could not be made; (b) because of this, errors were introduced into the estimation of the wave displacement profile needed to determine the ability of the assumed gravity wave to initiate convection; (c) the wind-pressure correlation analysis, critically important in evaluating the relative merits of the thermal plume and gravity wave hypotheses, could not be conducted; and (d) a reliable wave energy flux profile could not be calculated.

If the estimate of intrinsic phase speed $|\underset{\sim}{C}_\omega|$ is substituted directly into the surface pressure perturbation P_o formula (23), and it is assumed that the maximum wave-induced parcel displacement $\zeta_H = 2.1$ km is accurate, then $P_o = 0.67$ mb results. This magnitude exceeds the read-off error in the NSSL microbarograph data, yet pressure wave signals could not be detected. Undoubtedly, the estimates of both $|\underset{\sim}{C}_\omega|$ and P_o are too large, since ζ_H (and so the gravity wave vertical velocities) are probably too large by at least a factor of two. Moreover, the physical structure of the environment at and west of the dryline can only support gravity waves with very small $|\underset{\sim}{C}_\omega|$, a fact which is consistent with the observation of poor spatial coherence in the waveforms (see (43)). Despite these problems, a corresponding reduction in the value

of ζ_H will not change the final conclusion that the evanescent gravity wave has the ability to initiate deep convection.

Another drawback concerns the lack of rawinsonde data of sufficient spatial/temporal resolution to define the mesoscale variability of the atmospheric vertical structure near the dryline. This data problem prohibited an assessment of the precise roles played by dynamic instability and geostrophic imbalance in the generation of gravity waves, and the low-level inversion in ducting the waves. In summary, gravity waves could not be proven to be the responsible "trigger mechanism" because of these problems. Indeed, other untestable hypotheses like the vortex tube stretching mechanism of Barcilon and Drazin (1972) seem plausible. More complex theories concerning mixed modes of activity (e.g. Gossard and Moninger, 1975) were not considered because of the degree of success of the simpler gravity wave hypothesis in explaining the observations.

The remedies for these problems are three-fold. Firstly, a sensitive microbarograph system with a resolution and reporting increment of 0.1 mb, preferably with filtering devices, is needed to detect atmospheric gravity waves of the type apparently found in this case study. The PAM (Portable Automated Mesonet) pressure sensors employed in the SESAME '79 experiment do meet these specifications, however the SAM digital system used by NSSL in that experiment fail to do so. In the latter case, priority was given to reporting

dynamic range rather than reporting increment (accuracy). Next, at least three, and preferably five, instrumented levels are needed on meteorological towers to permit wave energy flux calculations. Thirdly, higher resolution rawinsonde (or satellite-derived profile) data are needed to determine the atmospheric structure in the mesoscale environment in which gravity waves may occur. Although there is small hope to ever be able to detect the waves themselves, it is essential that the ambient conditions be known, which is possible with a 50 km/60 min resolution, but not with the 120 km/90 min resolution available on 8 June 1974.

The results of this research have shed some light on one type of mesoscale mechanism that can trigger the development of severe storms along drylines. By focusing down from the subsynoptic to the mesoscale, the nature of the subsynoptic moisture convergence region could be understood more clearly. Future studies should also examine the dynamical coupling between these scales and determine if and why mesoscale gravity waves are actually the response to an instability created on the larger scale. The role of downward momentum transport in sustaining low-level convergence (McGinley, 1973) should be investigated using such a multiple-scale approach. Also, more complex mechanisms (e.g. mixed wave modes) should be examined for relevance. These efforts should provide additional insights into the scale interactive processes that initiate and maintain severe

convective storms, and establish the degree of generality of the conclusions from this thesis.

REFERENCES

Anthony, R. W., 1978: Dust storm-severe storm characteristics of 10 March 1977. Mon. Wea. Rev., 106, 1219-1223.

Asai, T., 1970: Three-dimensional features of thermal convection in a plane Coutte flow. J. Meteor. Soc. Japan, 48, 18-29.

Barcilon, A., and P. G. Drazin, 1972: Dust devil formation. Geophys. Fl. Dyn., 4, 147-158.

Barnes, S. L., 1973: Mesoscale objective analysis using weighted time-series observations. NOAA Tech. Memo. ERL NSSL-62, National Severe Storms Laboratory, Norman, Oklahoma, 60 pp.

_____, 1978: Oklahoma thunderstorms on 29-30 April 1970: Part I: Morphology of a tornadic storm. Mon. Wea Rev., 106, 673-684.

Blumen, W., 1972: Geostrophic adjustment. Rev. Geophys. and Space Physics, 10, 485-528.

Bonner, W. D., 1966: Case study of thunderstorm activity in relation to the low-level jet. Mon. Wea. Rev., 94, 167-178.

Carter, J. K., 1970: The meteorologically instrumented WKY-TV tower facility. NOAA Tech. Memo. ERLTM-NSSL-50. National Severe Storms Laboratory, Norman, Oklahoma, 18 pp.

Danielsen, E., 1974: The relationship between severe weather, major dust storms and rapid large-scale cyclogenesis, I and II. Subsynoptic Extratropical Weather Systems Colloquium Notes, Vol. II, National Center for Atmospheric Research, Boulder, Col., 215-241.

Doswell, C. A., 1977: Obtaining meteorologically significant surface divergence fields through the filtering property of objective analysis. Mon. Wea. Rev., 105, 885-892.

Duchon, C. E., and J. S. Goerss, 1977: Errors in computing coherence spectra. Proceedings, Fifth Conf. on Probability and Statistics in Atmospheric Sciences, Las Vegas, Amer. Meteor. Soc., 291-296.

Elliott, J. A., 1972: Microscale pressure fluctuations measured within the lower atmospheric boundary layer. J. Fluid Mech., 53, 351-383.

Fawbush, E. J., R. C. Miller, and L. G. Starret, 1951: An empirical method of forecasting tornado development. Bull. Am. Meteor. Soc., 32, 1-9.

Fujita, T., 1963: Analytical mesometeorology: a review, in Meteor. Monographs, 5, No. 27, 77-125.

Gill, G. C., and P. L. Hexter, 1972: Some instrumentation definitions for use by meteorologists and engineers. Bull. Am. Meteor. Soc., 53, 846-851.

Goff, R. C., 1975: Thunderstorm-outflow kinematics and dynamics. NOAA Tech. Memo. ERL NSSL-75, National Severe Storms Laboratory, Norman, Oklahoma, 63 pp.

_____, and W. D. Zittel, 1974: The NSSL/WKY-TV tower data collection program: April-July 1972. NOAA Tech. Memo. ERL NSSL-68, National Severe Storms Laboratory, Norman, Oklahoma, 45 pp.

Gossard, E. E., 1960: Spectra of atmospheric scalars. J. Geophys. Res., 65, 3339-3351.

_____, and W. H. Hooke, 1975: Waves in the Atmosphere. Developments in Atmospheric Science, II, Elsevier Scientific Publishing Co., Amsterdam, 456 pp.

_____, and W. R. Moninger, 1975: The influence of a capping inversion on the dynamic and convective instability of a boundary layer model with shear. J. Atmos. Sci., 32, 2111-2124.

_____, and W. B. Sweezy, 1974: Dispersion and spectra of gravity waves in the atmosphere. J. Atmos. Sci., 31, 1540-1548.

_____, and W. Munk, 1954: On gravity waves in the atmosphere. J. of Meteor., 11, 259-269.

Haltiner, G. J., 1971: Numerical Weather Prediction. John Wiley and Sons, Inc., New York, 317 pp.

Hempel, C. G., 1966: Philosophy of Natural Science. Prentice-Hall, Inc., Englewood Cliffs, N. J., 116 pp.

Herron, T. J., and I. Tolstoy, 1969: Tracking jet stream winds from ground level pressure signals. J. Atmos. Sci., 26, 266-269.

Hooke, W. H., and K. R. Hardy, 1975: Further study of the atmospheric gravity waves over the eastern seaboard on 18 March 1969. J. Appl. Meteor., 14, 31-38.

Hudson, H. R., 1971: On the relationship between horizontal moisture convergence and convective cloud formation. J. Appl. Meteor., 10, 755-762.

Jenkins, G. M., and D. G. Watts, 1968: Spectral Analysis and its Applications. Holden-Day, Inc., San Francisco, 525 pp.

Jones, W. L., 1972: Ducting of internal gravity waves on a stable layer with shear. J. Geophys. Res., 77, 3879-3885.

Koch, S. E., 1975: Observations of mesoscale factors influencing the intensity of new cell developments in convective storm situations. Report 75-1, Grant No. GI-31278X, Dept. of Meteorology, Univ. of Wisconsin, Madison, Wisconsin, 87 pp.

_____, and J. McCarthy, 1977: On the formation of tornadic storm systems in a dryline environment. Preprints, 10th Conf. on Severe Local Storms, Omaha, Nebraska, Am. Meteor. Soc., 479-486.

Kunkel, K. E., E. W. Eloranta, and S. T. Shipley, 1977: Lidar observations of the convective boundary layer. J. Appl. Meteor., 16, 1306-1311.

Kuo, H-L, 1949: Dynamic instability of two-dimensional nondivergent flow in a barotropic atmosphere. J. Meteor., 6, 105-122.

Lamb, H., 1932: Hydrodynamics. Cambridge University Press, (6th ed.), 738 pp.

Lanczos, D., 1956: Applied Analysis. Prentice-Hall, Inc., Englewood Cliffs, N.J., 539 pp.

Lilly, D. K., 1975: Severe storms and storm systems: Scientific background, methods, and critical questions: Cloud Dynamics (ed. H.R. Pruppacher), in Pageoph, 113, Birkhäuser Verlag, Basel, 713-734.

Lin, C. C., 1955: The Theory of Hydrodynamic Stability, Cambridge Univ. Press.

Lindzen, R. S., and K. K. Tung, 1976: Banded convective activity and ducted gravity waves. Mon. Wea. Rev., 104, 1602-1617.

Mastrantonio, G., F. Einaudi, and D. Fua, 1976: Generation of gravity waves by jet streams in the atmosphere. J. Atmos. Sci., 33, 1730-1738.

Matsumoto, S., and T. Akiyama, 1970: Mesoscale disturbances and related rainfall cells embedded in the "Baiu Front", with a proposal on the role of convective momentum transfer. J. Meteor. Soc. Japan, 48, 91-102.

Mazzarella, D. A., 1972: An inventory of specifications for wind measuring instruments. Bull. Am. Meteor. Soc., 53, 860-871.

McGinley, J., 1973: Environmental energy fields associated with severe storms. M.S. Thesis, University of Oklahoma, Norman, Oklahoma, 130 pp.

McGuire, E. L., 1962: The vertical structure of three drylines as revealed by aircraft traverses. National Severe Storms Project Report No. 7, National Severe Storms Laboratory, Norman, Oklahoma, 10 pp.

Merrill, J. T., 1977: Observational and theoretical study of shear instability in the airflow near the ground. J. Atmos. Sci., 34, 911-921.

Miles, J. W., 1961: On the stability of heterogeneous shear flows. J. Fluid Mech., 10, 496-508.

Miller, R. C., 1972: Notes on analysis and severe storm forecasting procedures of the Air Force Global Weather Central. Tech. Rep. 200, Air Weather Service, 190 pp. [AD-744 042]

NSSL (National Severe Storms Laboratory) Staff, 1971: The NSSL surface network and observations of hazardous wind gusts. NOAA Tech. Memo. No. ERL NSSL-55, National Severe Storms Laboratory, Norman, Oklahoma, 19 pp.

NSSP (National Severe Storms Project) Staff Members, 1963: Environmental and thunderstorm structures as shown by National Severe Storms Project observations in Spring 1960 and 1961. Mon. Wea. Rev., 91, 271-292.

Ogura, Y., and Y-L Chen, 1977: A life history of an intense mesoscale convective storm in Oklahoma. J. Atmos. Sci., 34, 1458-1476.

Orlanski, I., 1968: Instability of frontal waves. J. Atmos. Sci., 25, 178-200.

Panofsky, H. A., and G. W. Brier, 1968: Some Applications of Statistics to Meteorology. Pennsylvania State University Press, University Park, Pa., 224 pp.

Petersen, D. P., and D. Middleton, 1963: On representative observations. Tellus, 15, 387-405.

Pitchford, K. L., and J. London, 1962: The low-level jet as related to nocturnal thunderstorms over midwest United States. J. Appl. Meteor., 1, 43-47.

Purdom, J. F. W., 1976: Some uses of high resolution GOES imagery in the mesoscale forecasting of convection and its behavior. Mon. Wea. Rev., 104, 1474-1483.

Raymond, D. J., 1975: A model for predicting the movement of continuously propagating convective storms. J. Atmos. Sci., 32, 1308-1317.

Reed, R. J., and K. R. Hardy, 1972: A case study of persistent, intense, clear air turbulence in an upper level frontal zone. J. Appl. Meteor., 11, 541-549.

Reinsch, C. H., 1967: Smoothing by spline functions. Numerische Mathematik, 10 (3), 177-183.

Rhea, J. O., 1966: A study of thunderstorm formation along drylines. J. Appl. Meteor., 5, 58-63.

Sasaki, Y., 1973: Mechanism of squall-line formation as suggested from variational analysis of hourly surface observations. Preprints, 8th Conf. on Severe Local Storms, Denver, Colorado, Am. Meteor. Soc., 300-307.

Schaefer, J. T., 1973: The motion and morphology of the dryline. NOAA Tech. Memo ERL NSSL-66, National Severe Storms Laboratory, Norman, Oklahoma, 81 pp.

_____, 1975: Nonlinear biconstituent diffusion: A possible trigger of convection. J. Atmos Sci., 32, 2278-2284.

Stephens, J. J., 1966: Low-pass filters for a sequence of equally-spaced data. Atmospheric Science Group, University of Texas (unpublished manuscript), 20 pp.

Tanaka, H., 1975: Quasi-linear and nonlinear interactions of finite amplitude perturbations in a stably stratified fluid. J. Meteor. Soc. Japan, 53, 1-32.

Tegtmeier, S. A., 1974: The role of the surface, subsynoptic, low pressure system in severe weather forecasting. M.S. Thesis, University of Oklahoma, Norman, Oklahoma, 66 pp.

Tennekes, H., and J. L. Lumley, 1972: A First Course in Turbulence. MIT Press, Cambridge, Massachusetts, 300 pp.

Tidwell, L. G., 1975: A synoptic and subsynoptic study of the June 8, 1974 severe thunderstorm and tornado outbreak in Oklahoma. M.S. Thesis, University of Oklahoma, Norman, Okla., 65 pp.

Uccellini, L.W., 1975: A case study of apparent gravity wave initiation of severe convective storms. Mon. Wea. Rev., 103, 497-513.

Ulanski, S. L., and M. Garstang, 1978: The role of surface divergence and vorticity in the life cycle of convective rainfall. Part I: Observations and analysis. J. Atmos. Sci., 35, 1047-1062.

Wallace, J. M., 1971: Spectral studies of tropospheric wave disturbances in the tropical Western Pacific. Rev. Geophys. and Space Physics, 9, 557-612.

Wilk, K. E., and R. A. Brown, 1975: Applications of conventional and Doppler radar measurements in severe storm research. Preprints Third Symposium on Meteorological Observations and Instrumentation, Washington, Amer. Meteor. Soc., 165-174.

Zawadzki, I. I., 1973: Measurement and application of rainfall autocorrelation functions. Report MW-76, McGill University, 33 pp.

APPENDIX A

TIME-SPACE CONVERSION TECHNIQUE APPLIED TO MESOSCALE OBJECTIVE ANALYSIS

The methods by which the weight parameters κ^* and ν^* in (1) were chosen, and the sensitivity of the analyses to temporal and spatial variation of the advection vector $\underset{\sim}{C}$, is discussed in this appendix.

a. Empirical Tests on Analytical Data

By what criterion can a value for κ^* be chosen? It was mentioned in section II that the chosen value of κ^* (81 km^2) resulted in a theoretical response of 0.76 for $\lambda=2\Delta n$ wavelengths and a response of 0.04 for $\lambda=2\Delta x$ wavelengths. The response function shown in Fig. 2 was calculated for a steady-state translating wave of wavelength λ and amplitude A of the form

$$f(x,t') = A \sin\left[\frac{2\pi}{\lambda}\ (x' - ct')\right], \qquad \text{(A1)}$$

where x' is the distance in the direction of wave travel $\underset{\sim}{C}$, and t' is the time difference from the reference time. It can be shown (Barnes, 1973) that the theoretical response of the time-to-space conversion (TSC) technique to

this function involves only the space weighting parameter and the numerical convergence parameter γ (=0.4), namely

$$R(\lambda) = R_o(\lambda)[1 + (R_o(\lambda))^{\gamma-1} - (R_o(\lambda))^{\gamma}], \qquad (A2)$$

where

$$R_o(\lambda) = \exp\left[-\left(\frac{\pi}{\lambda}\right)^2 \kappa^*\right]. \qquad (A3)$$

These equations were employed in the construction of the response curve shown in Fig. 2.

Barnes performed empirical tests on this function specified for a different data array and set of κ^*, ν^*, $\underset{\sim}{C}$ parameters than the ones used in the present case study. The results of those tests showed that significantly more detail can be obtained using the TSC technique than relying upon "synoptic" (on-time) observations alone. Because each reporting station generates a series of observations strung out along $\underset{\sim}{C}$, the TSC technique has the ability to resolve a $2\Delta n$ wave, whereas a synoptic analysis will produce extremely noisy and incoherent fields. Sampling theory (Petersen and Middleton, 1963) specifies that 5 data points (not 3 as for a $2\Delta n$ wave) are necessary to resolve a disturbance and its derivatives. Thus it is the objective of the present tests on the analytical function (A1) to prove that the TSC technique can indeed resolve a $2\Delta n$ wave, and hence to show its superiority over a synoptic analysis.

In these tests, the analytical function (A1) determines both the "observed" data and the test values at grid points. The observation values are calculated for a 26 x 7 array (26 stations and 7 time series values) using values of $t' = n\Delta t$ ($n = -3, -2, \ldots, +3$), and a sampling interval of $\Delta t = 5$ min. An advection vector of $\underset{\sim}{C} = 218^\circ$, 66.6 km/hr was employed (see part c below), thus resulting in off-time displacement increments of $ct' = 5.55$ km, or roughly $0.8\ \Delta r$ (Δr = grid diagonal). The values at the observation points are then computed directly from (A1) after making a transformation of coordinates from the east-west Cartesian grid to the rotated grid in the direction $\underset{\sim}{C}$ via

$$x' = x \cos \theta^* + y \sin \theta^*, \qquad \text{(A4)}$$

where $\theta^* = 270^\circ - \theta = 218^\circ$. Wave amplitude A is set equal to 100 arbitrary units.

The results of the experiments for the test function (verification) field, the TSC-derived field, and the synoptic field are shown in Figs. A1, A2, and A3, respectively. The appearance of the TSC field is remarkably superior to that of the synoptic field, in terms of amplitude response, wave phase, and spatial coherence. Other indicators of the superiority of the TSC technique are a reduction in the total field RMS error from 86 to 77 and a 24% reduction in the error of the field mean value.

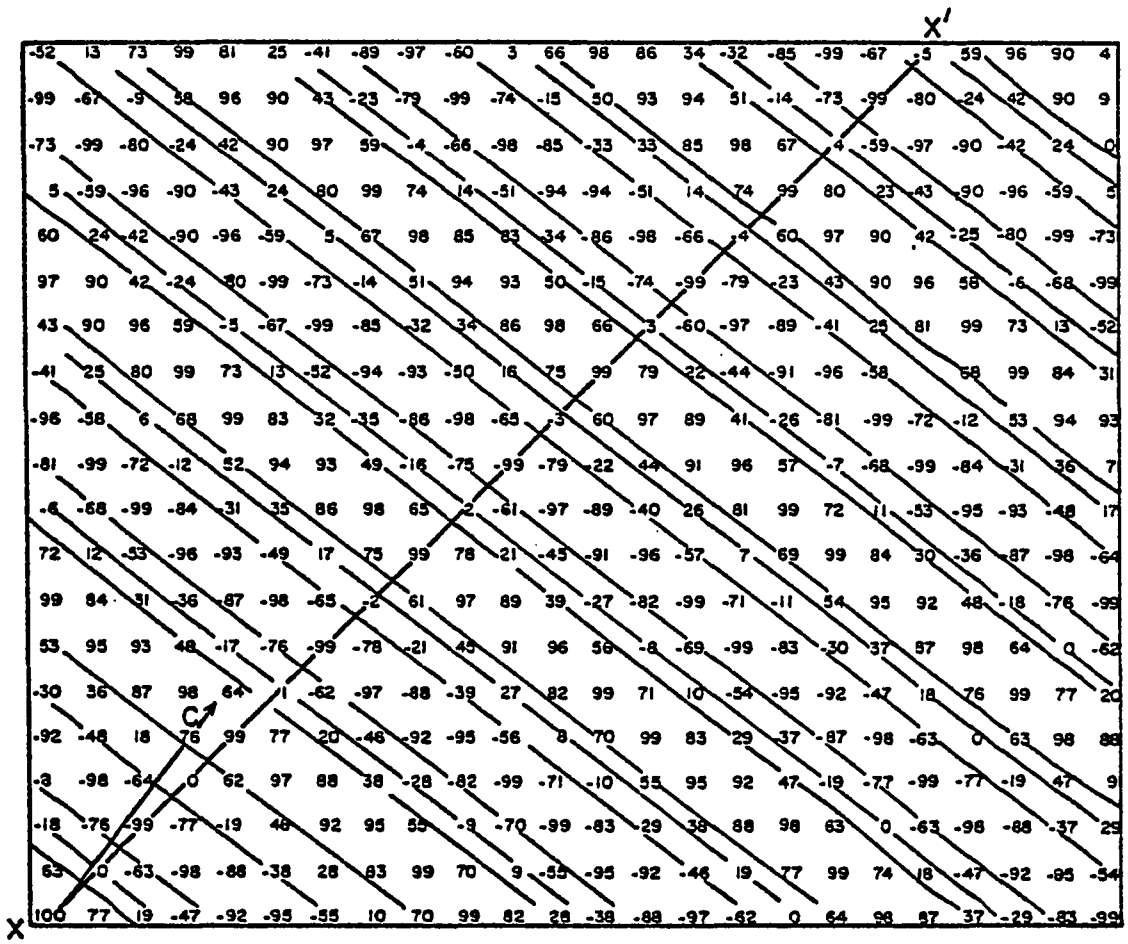

Fig. A1. Test function (verification) field for empirical study of time-to-space conversion technique. Note the direction of advection vector $\underset{\sim}{C}$.

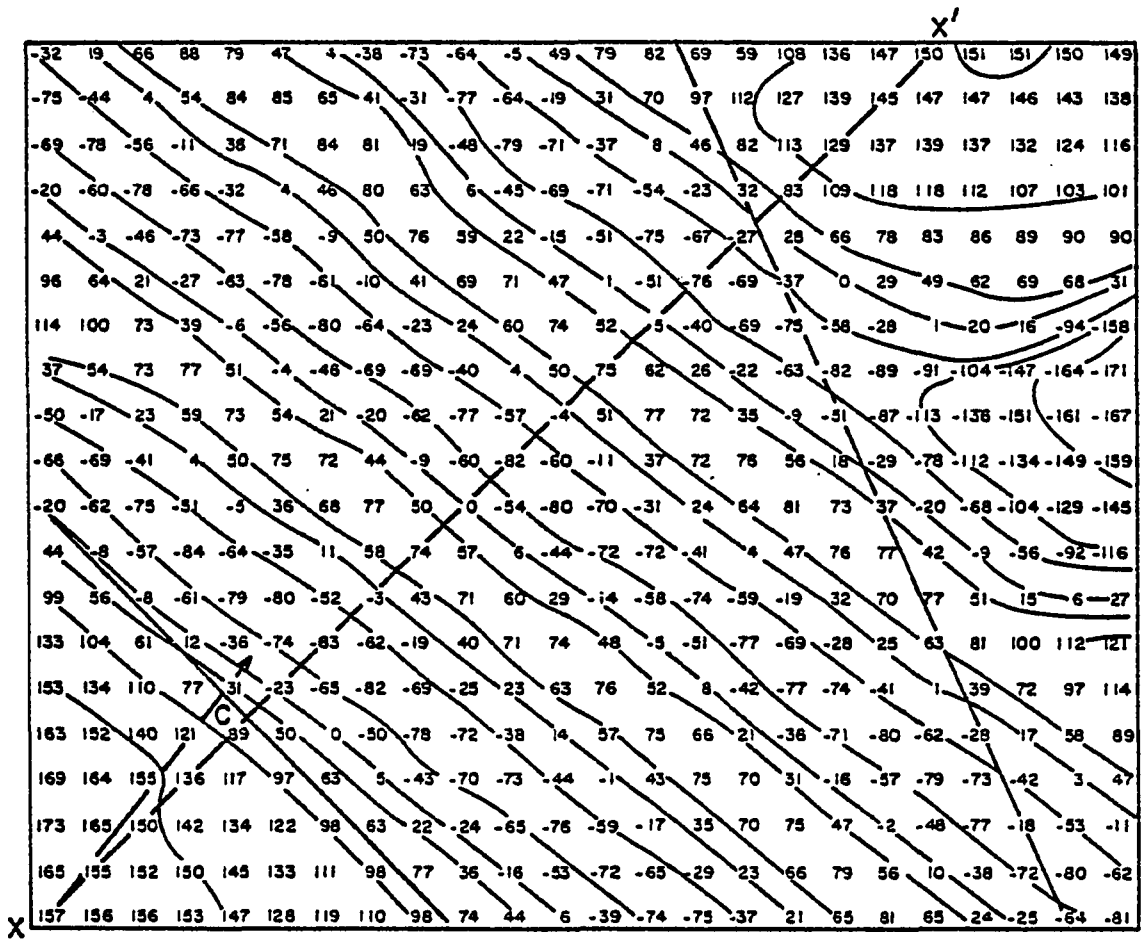

Fig. A2. Interpolated field resulting from time-to-space conversion.

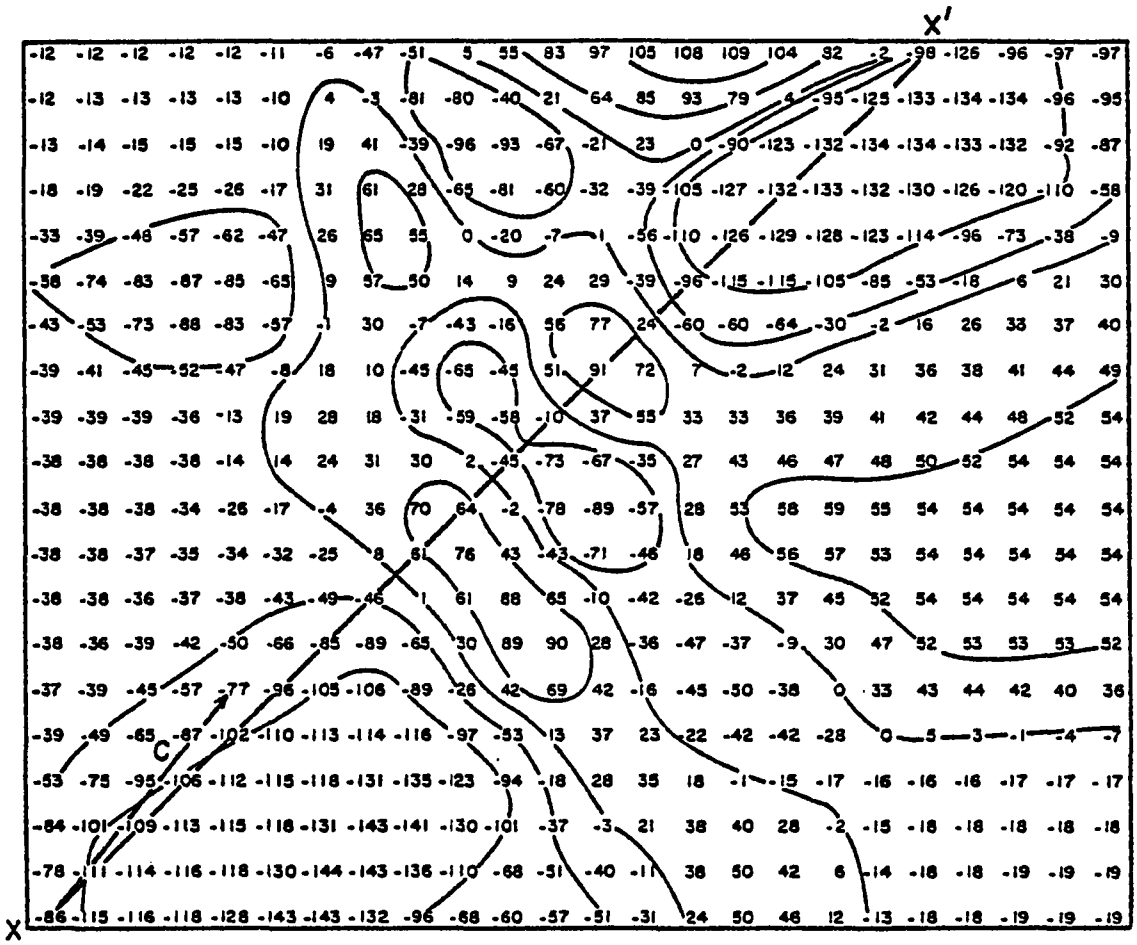

Fig. A3. Interpolated field resulting from synoptic (on-time) analysis.

A cross section was made along the line x-x' nearly normal to the wave fronts to emphasize the superior results obtained using this technique (see Fig. A4). The TSC field rapidly deteriorates outside of the solid diagonal borders, so no analyzed fields were examined in the main body of this paper outside of this "reliable domain". These borders were drawn at $2\Delta r$ distance from the nearest station, a conservative estimate of reliability considering that $3 \times 0.8\Delta r = 2.4\Delta r$ was theoretically accurate. Even inside the "reliable domain", amplitude responses and phases are improved. Notice that the experimental responses of this technique agree closely with the theoretical response (0.76) calculated from (A2) and (A3). These general results are in agreement with those of Barnes.

b. Determination of ν^*

Both the tests above and the other map analyses employed a value of $\nu^* = 225$ min^2. The proper choice of ν^* is based upon the data spacing, the value of Δt, and the degree to which the system of interest (e.g., a thunderstorm) may be assumed to be in steady state. As $\nu^* \to \infty$, all the time-series data apply with nearly equal weight regardless of when observed (see (1)), thus large ν^* is properly assigned for quasi-steady state systems.

Although the properties of the system are assumed to be advected horizontally with the translational velocity $\underline{C}$ of the system (which is allowed to vary spatially/

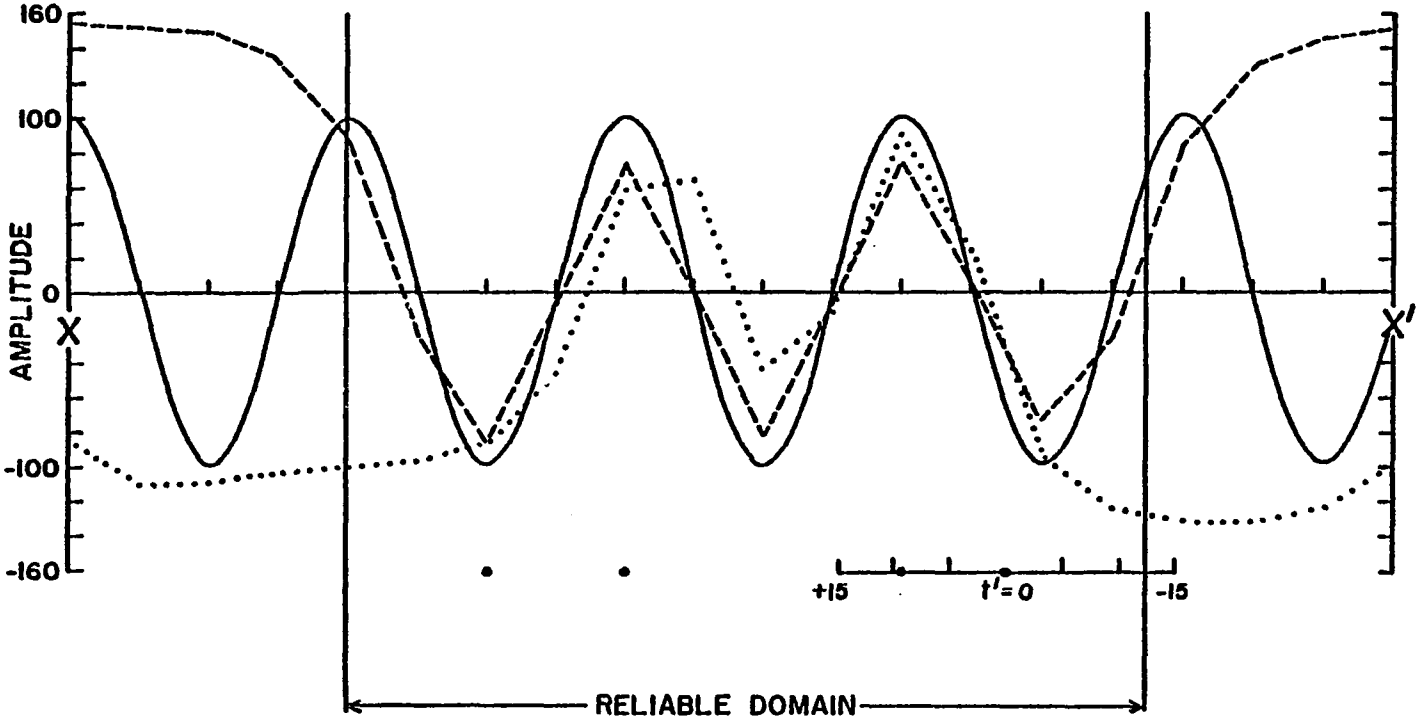

Fig. A4. Cross section along line x-x' of fields in three previous figures. Test function, time-to-space conversion, and synoptic results are depicted by solid, dashed, and dotted lines, respectively. Solid circles beneath denote station locations within one grid distance from line x-x'. Tic marks spaced equidistantly from rightmost station show spatial positions of all 7 off-time observations at that station for 5-minute interval data. Reliable domain corresponds to area inside the diagonal borders of Fig. A2.

temporally), for this strictly to be the case the system cannot undergo substantial change, but must be in steady state over the conversion period τ. However, the Barnes technique uniquely assumes a decrease of system conservation with time difference from the reference time. For this reason an autocorrelation study should be useful for objectively determining $\nu^* = \tau^2$, where τ is now viewed as a "decorrelation lag time", at the point where the autocorrelation function first drops below a value of e^{-1}. Although this strictly requires a matching of time-averaged Lagrangian and station Eulerian autocorrelation functions (Zawadzki, 1973), a calculation of only the latter for selected stations gave a value of $\tau = \pm$ 15 min, $\nu^* = 225$ min^2, resulting in 7 time-series observations being used for each analysis.

To confirm this result (that the systems in this case study could be assumed quasi-steady state over the conversion period τ), objective analyses were run for various values of τ. Those with $\tau < 15$ min displayed less coherence and more noise, a result which is due to the data spacing and Δt value. On the other hand, use of a larger τ could not be justified from the autocorrelation study, since the chosen τ value would be an uppermost limit to the Zawadzki, (op. cit.) one. Thus, in practice one can choose a value of ν^* partly on empirical grounds, but guided by objective autocorrelation analysis.

c. Determination of $\underset{\sim}{C}$

The choice of either one or multiple values for the translation vector $\underset{\sim}{C}$ rests solely on empirical grounds. As Fujita (1963) showed, system areal fluctuations may be accommodated by specification of a spatially varying translation vector. Although this complication is suggested for such events as thunderstorm downdrafts, all the storms in this case study were still in the development stage while over the mesonetwork and did not display strongly divergent fields typical of mature downdrafts.

As with other studies (Fujita, 1963; Barnes, 1978) the first guess made for $\underset{\sim}{C}$ was observed storm motion - here the average translation vector of 16 storm cells over the mesonetwork. Using this vector instead of the individual cell vectors results in an off-time displacement difference of no more than one grid distance for all but one of the cells. Comparison of positions of prominent features appearing in those analyses resulting from the use of this one vector with the station time series showed that the first guess was 18% too high. Hence a better estimate of the appropriate vector value is $\underset{\sim}{C} = 218°$, 66.6 km/hr for all analyses in the 1100-1730 CST period ($C = 225°$, 65.0 km/hr at later times).

The fact that the final choice of $\underset{\sim}{C}$ was quite close to the average storm motion is not fortuitous. Even though vertical advection of air aloft to the ground was apparently

minimal, prominent features obviously related to individual storm cells after first echo appearance still seemed to translate at roughly the same velocity prior to first echo. Such related features as the energy convergence and mesolow centers could be tracked back in time for at least 30 min prior to first echo, in both the mesoanalysis and the time series. It was actually quite fortunate that the storms did not fully mature until they were edging the network, and that the same system velocity was quite valid for all meteorological parameters, at least over the conversion period τ. In general, the analyst must evaluate each case separately to determine what conditions are relevant in the choice of $\underset{\sim}{C}$.

APPENDIX B

PERFORMANCE CHARACTERISTICS OF MESONETWORK AND WKY-TV TOWER INSTRUMENTS

Table B1 lists the various components of the data acquisition systems and their performance characteristics as described by Carter (1970), NSSL (1971), and Mazzarella (1972).

It is assumed that the wind speed, temperature, relative humidity, and pressure sensors act approximately as first-order systems that behave mathematically as

$$\tau \frac{dX_0}{dt} + X_0 = X_i \ , \tag{B1}$$

where X_i is the input value and X_0 the output from the sensor. For this system, the amplitude reduction ratio is

$$\frac{A_0}{A_i} = \frac{1}{\sqrt{1 + (\tau\omega)^2}} \tag{B2}$$

and the phase error produced is

$$\varphi = \tan^{-1} (\tau\omega), \tag{B3}$$

where ω $(= 2\pi/T)$ is the circular frequency of an assumed

Table B1. SENSOR PERFORMANCE CHARACTERISTICS

Measured Variable	Sensor Type	Sensor Constants[1]	Threshold Values	Resolution	Absolute Accuracy
Mesonetwork Wind Speed	F420C cup anemometer	d = 7.96 m	1.03 m sec^{-1}	0.77 m sec^{-1}	---
Wind Direction	F005 wind-vane	ζ = 0.14 λ_n = 17.53 m	1.03 m sec^{-1}	22.5°	---
Temperature	Friez Model 594 Hygro-thermograph (Bourdon Tube Type)	τ < 100 sec^{2}	---	1.1°C	---
Relative Humidity	Friez Model 594 Hygro-thermograph (Human Hair Type)	τ < 30 sec^{2} (for temp. > 20°C)	---	5%	---
Pressure	Belfort Model 5-800 Microbaro-graph	τ < 60 sec^{2}	---	0.68 mb	---
WKY-TV Tower Horizontal Wind	Bendix Model 120 Aerovane	d = 4.67 m ζ = 0.28 λ_n = 14.63 m	0.87 m sec^{-1}	---	0.26 m sec^{-1} 3°
Temperature[3]	Yellow Springs Instr. Co. Thermistor	τ < 25 sec	---	---	0.2°C
Relative Humidity	PCRC-11 Hot Wire	τ < 30 sec (avg. τ = 5 sec)	---	---	3%
Pressure	Belfort Model 6068 Micro-barograph	---	0.2 mb	---	0.5 mb
Vertical Wind	Gill Model 27100 Anemometer	d = 0.95 m	0.25 m sec^{-1}	---	0.11 m sec^{-1}

[1]The symbols used here are the following: distance constant (d), damping ratio (ζ), undamped natural wavelength (λ_n), and time constant (τ). See Gill and Hexter (1972) for definitions.

[2]Estimates by Prof. Fred Brock, Adjunct Professor in Department of Meteorology, University of Oklahoma. Exact values are not readily obtainable.

[3]Two independent electrical systems are used on the tower to provide redundancy for quality control.

sinusoidal input wave of period T.

It is also assumed that the wind vanes act approximately as second-order systems that behave according to

$$\frac{d^2x_0}{dt^2} + 2\zeta\omega_n \frac{dx_0}{dt} + \omega_n{}^2 x_0 = \omega_n{}^2 x_i, \tag{B4}$$

where ω_n $(= U\frac{2\pi}{\lambda_n})$ is the "natural frequency" as a function of incident wind speed U. For this system, the amplitude reduction ratio is

$$\frac{A_0}{A_i} = \frac{1}{\left[1 - \left(\frac{\omega}{\omega_n}\right)^2 + \left(2\zeta\frac{\omega}{\omega_n}\right)^2\right]^{\frac{1}{2}}} \tag{B5}$$

and the phase error is

$$\varphi = \tan^{-1}\left[\frac{-2\zeta\ \omega/\omega_n}{1 - \left(\omega/\omega_n\right)^2}\right]. \tag{B6}$$

Using the sensor performance characteristics in Table B1 and assuming U = 5 m sec^{-1}, we can calculate A_0/A_i and φ for all systems using (B2), (B3), (B5), and (B6). For this value of U, $\tau = 1.59$ and 0.93 sec, respectively, for the F420C and Bendix 120 wind speed sensors, and $\omega_n = 1.792$ sec^{-1}. A larger value of U will improve the response characteristics, so the calculations presented in Table B2 represent the "worst possible conditions" expected. The response of the tower sensors is in every case better than those shown here, so no calculations were made.

Table B2. Calculated Response of Mesometeorological Sensors to Atmospheric Waves of Various Periods. Response of Tower Sensors in Every Case Exceeds These Values. Phase Lags ϕ Given in Degrees and Parenthetically in Time (Minutes).

	S E N S O R									
	Wind Speed (τ = 1.59 sec)		Wind Direction ω_n = 1.792 sec^{-1} ζ = 0.14		Temperature (τ = 100 sec)		Relative Humidity (τ = 30 sec)		Pressure (τ = 60 sec)	
T (min)	A_0/A_i	ϕ	A_0/A_i	ϕ	A_0/A_i	ϕ	A_0/A_i	ϕ	A_0/A_i	ϕ
5	1.00	2(1)	1.00	0(0)	0.43	65(1)	0.85	32(0)	0.62	52(1)
10	1.00	1(0)	1.00	0(0)	0.69	46(1)	0.95	17(1)	0.85	32(1)
15	1.00	1(0)	1.00	0(0)	0.82	35(1)	0.98	12(1)	0.92	23(1)
20	1.00	0(0)	1.00	0(0)	0.89	28(2)	0.99	9(1)	0.95	17(1)

APPENDIX C

CONSTRUCTION OF A BANDPASS FILTER

In the construction of any filter a trade-off must be made between the steepness of the slope of the filter and the amplitude of the "Gibbs oscillations" beyond the cutoff frequencies. Generally speaking, the greater the number of weights employed, the greater the damping of the Gibbs oscillations. The low-pass filter of Lanczos (1956) uses sigma factors to perform this damping. The kth weight is determined by

$$w_k = \frac{\sin(2\pi f_c k)}{\pi k} \left[\frac{\sin(\pi k/n)}{\pi k/n} \right]^m , \qquad (C1)$$

where n is half the number of total weights minus one, f_c is the cutoff frequency at which the filter response is 0.5, and m gives the number of applications of the σ factor, found inside the exponent.

A bandpass filter can be constructed from the subtraction of two low-pass filters, or the addition of a low-pass and high-pass filter. The weights are then determined by

$$w_k = \frac{\sin(2\pi f_{c2} k) - \sin(2\pi f_{c1} k)}{\pi k} \left[\frac{\sin(\pi k/n)}{\pi k/n} \right]^m , \qquad (C2)$$

whose response is given by

$$R(f) = w_o + 2 \sum_{k=-n}^{n} w_k \cos (2\pi f k). \qquad (C3)$$

The filter response shown in Fig. 16 results from taking $n = 25$, $\sigma = 1$, $f_{c2} = 0.105$, and $f_{c1} = 0.027$.

A test of the filter was made upon a synthetic time series generated by superpositioning white noise, a discrete first-order autoregressive process, and a pure tone signal whose frequency matches that of the maximum filter response. The filter effectiveness was determined by passing the synthetic data, a rough simulation of atmospheric data, through the filter and examining changes in both the time series and the computed autocorrelation function. The results of this test confirm that autocorrelation peaks more than double in amplitude (see Fig. C1) and become quite periodic following the bandpass filtering. The appearance of the filtered time series was also quite reasonable and satisfactory. Notice that the phase of the harmonic signal is unaltered by the filtering process.

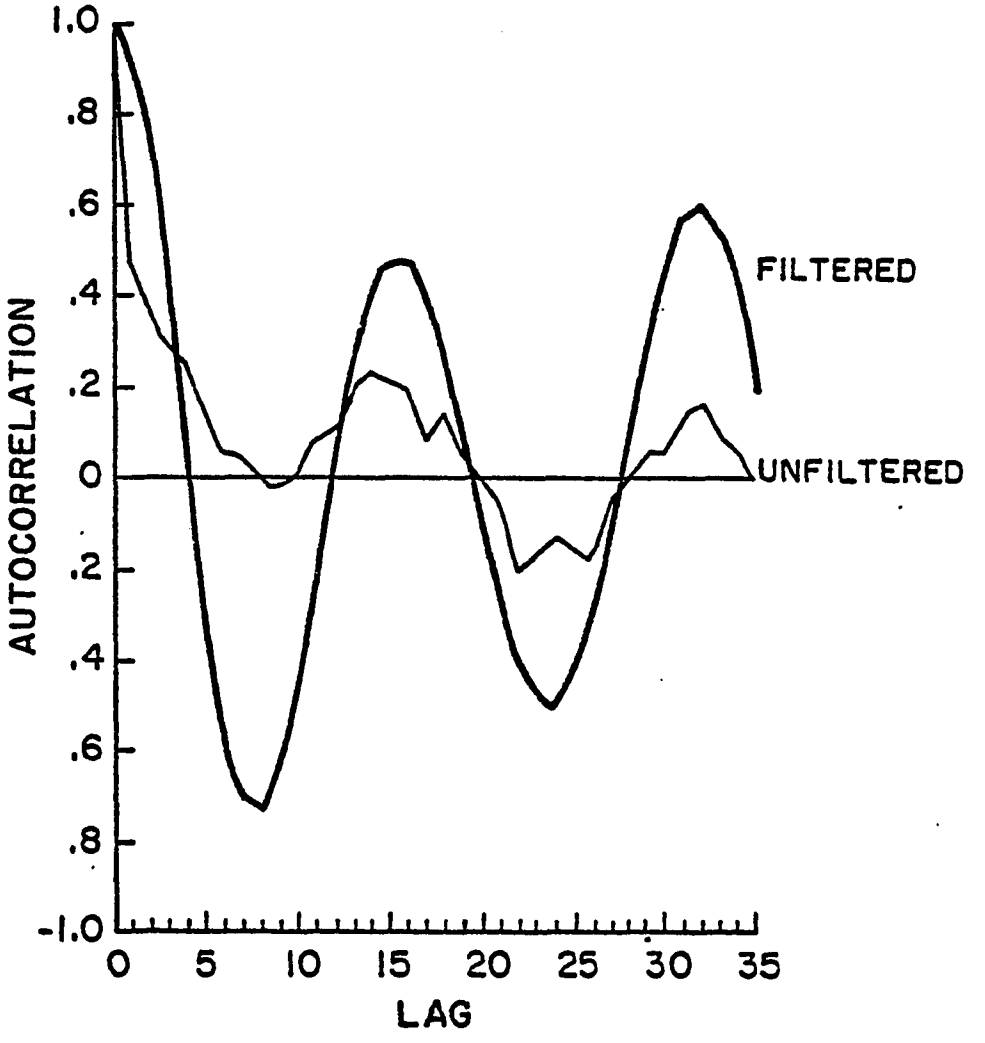

Fig. C1. Autocorrelograms computed from unfiltered and band-pass filtered synthetic time series.